Radiation Dose to the Lens of the Eye from Computed Tomography Scans of the Head

by

Natalie Ann Januzis

Graduate Program of Medical Physics
Duke University

Date:_____

Approved:

_____
Terry Yoshizumi, Supervisor

_____
Martin Tornai, Chair

_____
James Colsher

_____
Donald Frush

_____
Rathnayaka Gunasingha

_____
Neil Petry

Dissertation submitted in partial fulfillment of
the requirements for the degree of Doctor of Philosophy in the Graduate Program of
Medical Physics in the Graduate School
of Duke University

2016

ABSTRACT

Radiation Dose to the Lens of the Eye from Computed Tomography Scans of the Head

by

Natalie Ann Januzis

Graduate Program of Medical Physics
Duke University

Date:_____
Approved:

_____
Terry Yoshizumi, Supervisor

_____
Martin Tornai, Chair

_____
James Colsher

_____
Donald Frush

_____
Rathnayaka Gunasingha

_____
Neil Petry

An abstract of a dissertation submitted in partial
fulfillment of the requirements for the degree
of Doctor of Philosophy in the Graduate Program of
Medical Physics in the Graduate School of
Duke University

2016

Abstract

While it is well known that exposure to radiation can result in cataract formation, questions still remain about the presence of a dose threshold in radiation cataractogenesis. Since the exposure history from diagnostic CT exams is well documented in a patient's medical record, the population of patients chronically exposed to radiation from head CT exams may be an interesting area to explore for further research in this area. However, there are some challenges in estimating lens dose from head CT exams. An accurate lens dosimetry model would have to account for differences in imaging protocols, differences in head size, and the use of any dose reduction methods.

The overall objective of this dissertation was to develop a comprehensive method to estimate radiation dose to the lens of the eye for patients receiving CT scans of the head. This research is comprised of a physics component, in which a lens dosimetry model was derived for head CT, and a clinical component, which involved the application of that dosimetry model to patient data.

The physics component includes experiments related to the physical measurement of the radiation dose to the lens by various types of dosimeters placed within anthropomorphic phantoms. These dosimeters include high-sensitivity

MOSFETs, TLDs, and radiochromic film. The six anthropomorphic phantoms used in these experiments range in age from newborn to adult.

First, the lens dose from five clinically relevant head CT protocols was measured in the anthropomorphic phantoms with MOSFET dosimeters on two state-of-the-art CT scanners. The volume CT dose index ($CTDI_{vol}$), which is a standard CT output index, was compared to the measured lens doses. Phantom age-specific $CTDI_{vol}$-to-lens dose conversion factors were derived using linear regression analysis. Since head size can vary among individuals of the same age, a method was derived to estimate the $CTDI_{vol}$-to-lens dose conversion factor using the effective head diameter. These conversion factors were derived for each scanner individually, but also were derived with the combined data from the two scanners as a means to investigate the feasibility of a scanner-independent method. Using the scanner-independent method to derive the $CTDI_{vol}$-to-lens dose conversion factor from the effective head diameter, most of the fitted lens dose values fell within 10-15% of the measured values from the phantom study, suggesting that this is a fairly accurate method of estimating lens dose from the $CTDI_{vol}$ with knowledge of the patient's head size.

Second, the dose reduction potential of organ-based tube current modulation (OB-TCM) and its effect on the $CTDI_{vol}$-to-lens dose estimation method was investigated. The lens dose was measured with MOSFET dosimeters placed within the same six anthropomorphic phantoms. The phantoms were scanned with the five clinical head CT

protocols with OB-TCM enabled on the one scanner model at our institution equipped with this software. The average decrease in lens dose with OB-TCM ranged from 13.5 to 26.0%. Using the size-specific method to derive the $CTDI_{vol}$-to-lens dose conversion factor from the effective head diameter for protocols with OB-TCM, the majority of the fitted lens dose values fell within 15-18% of the measured values from the phantom study.

Third, the effect of gantry angulation on lens dose was investigated by measuring the lens dose with TLDs placed within the six anthropomorphic phantoms. The 2-dimensional spatial distribution of dose within the areas of the phantoms containing the orbit was measured with radiochromic film. A method was derived to determine the $CTDI_{vol}$-to-lens dose conversion factor based upon distance from the primary beam scan range to the lens. The average dose to the lens region decreased substantially for almost all the phantoms (ranging from 67 to 92%) when the orbit was exposed to scattered radiation compared to the primary beam. The effectiveness of this method to reduce lens dose is highly dependent upon the shape and size of the head, which influences whether or not the angled scan range coverage can include the entire brain volume and still avoid the orbit.

The clinical component of this dissertation involved performing retrospective patient studies in the pediatric and adult populations, and reconstructing the lens doses from head CT examinations with the methods derived in the physics component. The

cumulative lens doses in the patients selected for the retrospective study ranged from 40 to 1020 mGy in the pediatric group, and 53 to 2900 mGy in the adult group.

This dissertation represents a comprehensive approach to lens of the eye dosimetry in CT imaging of the head. The collected data and derived formulas can be used in future studies on radiation-induced cataracts from repeated CT imaging of the head. Additionally, it can be used in the areas of personalized patient dose management, and protocol optimization and clinician training.

Dedication

This work is dedicated to all of the people who have positively influenced me along my journey. First and foremost, this is dedicated to my parents, Nadine and Joseph Januzis, whose endless encouragement, patience, and love has helped to shape me into the person I am today. Secondly, this is dedicated to my fiancé, Adam Beckmann, whose constant love and support has provided me with the motivation to pursue this degree. Lastly, this is dedicated to Colleen Allen and our dog, Duke, who have inspired me to always work hard and who have made this journey truly incredible.

Contents

List of Tables

List of Figures

List of Abbreviations

AAPM	American Association of Physicists in Medicine
ADCL	Accredited Dosimetry Calibration Laboratory
AP	Anterioposterior
CF	Conversion Factor
CI	Confidence Interval
CTA	Computed Tomography Angiography
CTDI	Computed Tomography Dose Index
$CTDI_{100}$	CTDI measured along a 100-mm ion chamber
$CTDI_{vol}$	Volume Computed Tomography Dose Index
d_{eff}	Effective Diameter
DICOM	Digital Imaging and Communications in Medicine
DLP	Dose Length Product; product of $CTDI_{vol}$ and scan length (mGy-cm)
EMR	Electronic Medical Record
EPRI	Electric Power Research Institute
FOV	Reconstructed Field of View
Gy	Gray; a unit of radiation dose (1 Joule/kilogram)
HVL	Half Value Layer
ICRP	International Commission on Radiological Protection

IRB	Institutional Review Board
LAT	Lateral
LET	Linear Energy Transfer
MC	Monte Carlo
MOSFET	Metal Oxide Semiconductor Field Effect Transistor
MRN	Medical Record Number
NCRP	National Council on Radiation Protection and Measurements
netOD	Net Optical Density
OB-TCM	Organ-based Tube Current Modulation
Pitch	Table travel per tube rotation divided by beam collimation (mm/mm)
PMMA	Polymethyl methacrylate
PSC	Posterior Subcapsular
RBE	Relative Biological Effectiveness
SI	Scanner-independent
Sv	Sievert; unit of equivalent radiation dose
TBI	Total Body Irradiation
TF	Total Filtration
TLD	Thermoluminescent Dosimeter

Acknowledgements

I would like to acknowledge, first and foremost, my advisor, Dr. Terry Yoshizumi, who has provided me with a wealth of knowledge and experience in the medical health physics field. I am truly grateful for his guidance throughout my master's and PhD degrees. Next, I would like to acknowledge my committee members, Dr. Donald Frush, Dr. Martin Tornai, Dr. James Colsher, Dr. Rathnayaka Gunasingha, and Neil Petry, for their time and many contributions that have shaped this research project into what it is today. I would also like to thank the lab manager of the Duke Radiation Dosimetry Laboratory (DRDL), Giao Nguyen, who has provided me with much assistance in data collection and analysis. There have been many students in the DRDL who have contributed in some way to this work, and for that I am grateful as well. Finally, I would like to acknowledge Carolyn Lowry, a CT technologist at Duke University Medical Center. She spent many nights scanning phantoms with me, and her contribution is truly invaluable.

1. Introduction

1.1 Anatomy of the eye

The eye is a sphere-like structure, which is comprised of different components that aid in the sense of vision (Figure 1.1). The outermost layer of the eye, called the sclera, contains the cornea, which is transparent and located just anterior to the iris (the colored part of the eye). The vascular layer of the eye is the next layer moving inwards and consists of the choroid, ciliary body, and iris. Located just inside the sclera, the choroid is highly pigmented with melanin and contains many blood vessels. The ciliary body, which is comprised of the ciliary muscle and the ciliary processes, aids in suspending the lens in place via the suspensory ligament. The iris, which consists of smooth muscle fibers, attaches to the ciliary body and controls the amount of light that enters the eye by changing the size of the pupil. The retina is the innermost layer of the eye; it contains photoreceptor cells and the cells that pass nerve impulses along to the optic nerve (which emerges from the optic disk). The interior space of the eye is separated into the anterior and posterior cavities. The anterior cavity lies in front of the lens and is filled with the aqueous humor (a clear and watery substance). The posterior cavity, which consists of the entire space posterior to the lens, contains a semisolid material called the vitreous humor (1).

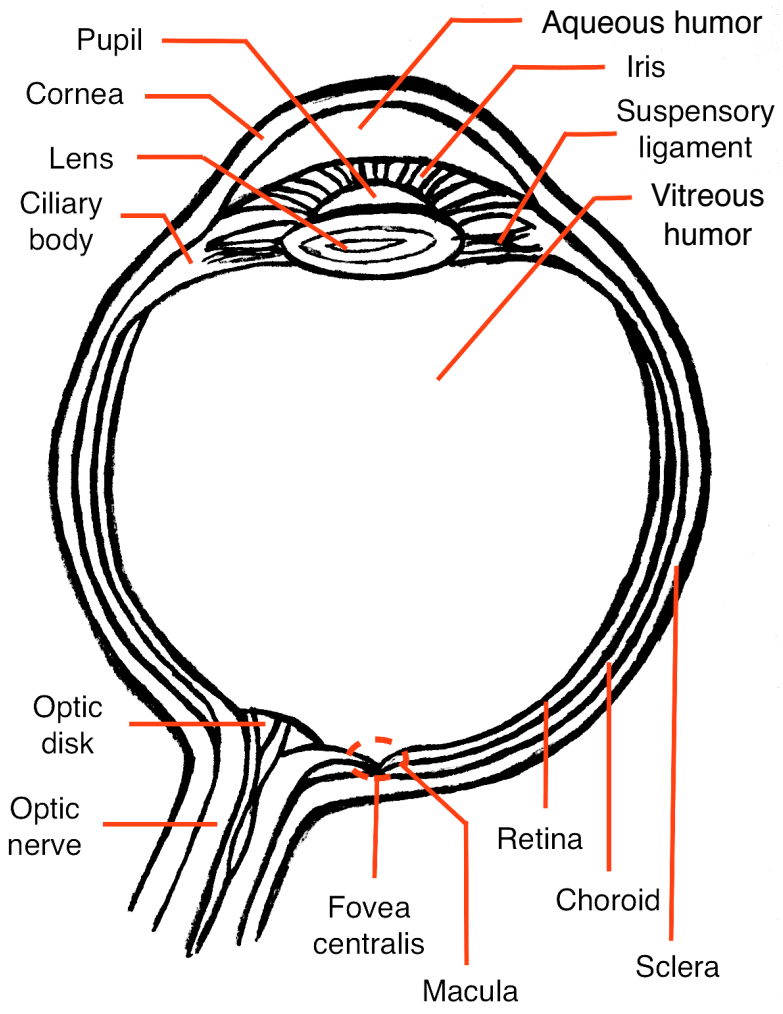

Figure 1.1: Anatomy of the eye

1.2 Anatomy of the Lens of the Eye

The lens of the eye, which is a transparent, biconvex structure, has the primary function of focusing incoming light on the retina to produce a sharp image. In order to focus on objects at different distances from the eye, the lens changes shape through contraction and relaxation of the ciliary muscles (1). The lens is comprised of three

components including the capsule, the epithelium, and the lens fibres. The lens capsule is a membrane that completely encloses the lens and protects it from viruses and bacteria (2-4). Since the lens is avascular, the capsule allows for passive exchange of nutrients into the lens and waste out of the lens (5).

A single layer of nucleated cuboid epithelial cells is present just inside the anterior capsule (Figure 1.2). Proliferation of these epithelial cells occurs in the germinative zone (located bilaterally just north of the lens equator); the new cells move along the capsule to the transitional zone where they differentiate and elongate into secondary fibre cells (6). As more are produced, the older secondary fibre cells are shifted towards the center of the lens where they wrap around the nucleus; differentiation of the secondary fibre cells results in loss of organelles and synthesis of certain crystallin proteins (7).

The nucleus is comprised of primary fibre cells, which originate from ectodermal cells located in the posterior area of the lens vesicle during gestation. Unlike the secondary fibre cells, which wrap around the nucleus, primary fibre cells are oriented in the antero-posterior direction (6). The human lens continues to gradually increase in size after birth with an observed linear growth mode continuing throughout life (8). Damage to lens proteins also accumulates throughout life because there is little protein turnover (9). While the lens is protected from light damage by antioxidants and antioxidant enzymes, there is a decrease in production of these defense systems by middle age (9).

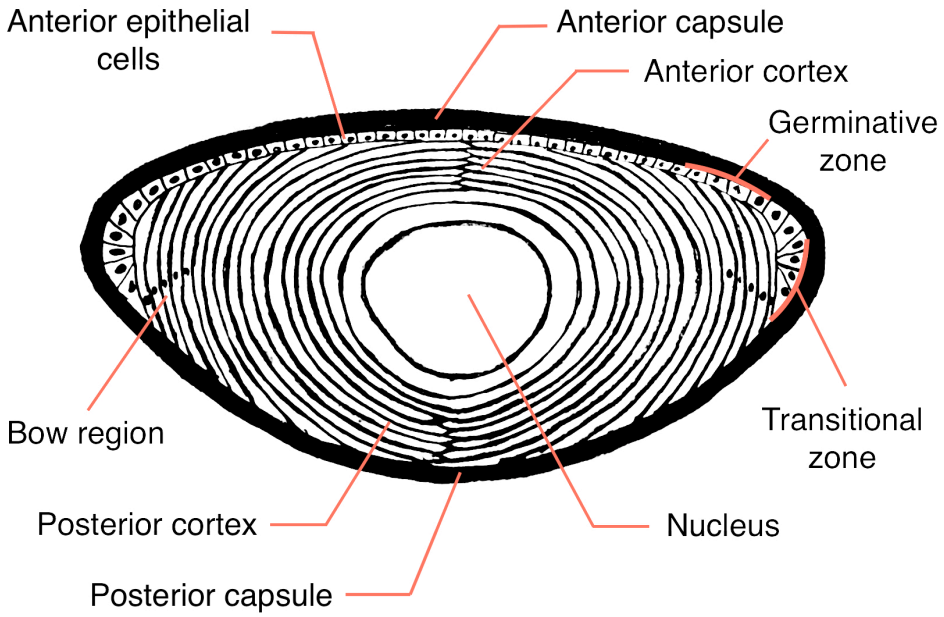

Figure 1.2: Anatomy of the human lens

1.3 Cataracts

Cataracts are one of the leading causes of visual impairment worldwide (10) and are defined as areas of opacities in the lens of the eye (1). Cataracts are typically associated with aging, but other risk factors include diabetes, corticosteroid use, exposure to sunlight, radiation exposure, and trauma (11).

Currently, the only method of treatment is surgical removal of the lens, and costs related to cataracts account for 40% of overall US ocular disease expenditures (12). There are certain risks associated with this treatment, including but not limited to posterior capsular opacification (otherwise known as secondary cataract), and retinal detachment

both of which have a higher occurrence in young patients undergoing cataract surgery (13).

1.3.1 Types and Risk Factors

Cataracts are classified by the location in the lens in which they are present. Types of cataracts include nuclear, cortical, posterior subcapsular (PSC), supranuclear, and mixed. Nuclear cataracts, which appear in the central portion of the lens, are the most common type of age-related cataract (14) and are associated with cigarette smoking (15). Cortical cataracts are the second most common age-related opacification (14). They appear in the cortex of the lens, and have been associated with diabetes (16), ultraviolet radiation (17), and ionizing radiation (18). PSC cataracts appear in the area adjacent to the posterior capsule and are associated with corticosteroid use (19), diabetes (20), and ionizing radiation (21, 22). Supranuclear cataracts appear in the region of the lens just above the nucleus and are associated with Alzheimer's disease and Down Syndrome (23, 24). Mixed cataracts refer to the presence of opacifications in more than one part of the lens. Cataracts can also be described by the degree of opacity present in the lens, whether they are stationary or progressive, and by the color of the opacification.

1.3.2 Detection and Quantification of Lens Opacities

Detection and documentation of cataracts in the lens is performed either by subjective methods using a slit lamp microscope or by objective methods using Scheimpflug photography of the anterior eye (25). The Scheimpflug slit images are

particularly advantageous for epidemiological studies because they provide measurements of light scatter in the lens, which allows for identification of early changes (25).

Standardized cataract grading systems have been developed for clinical use; these systems compare a patient's cataract to standard photographs to determine the severity. The numerous grading systems include the LOCS (Lens Opacities Classification Systems) (26-28), the Wilmer Clinical and Photographic Grading System (29), the Wisconsin Clinical and Photographic Grading System (30), the Oxford Clinical Cataract Grading System (31), the NEI Clinical Cataract Grading System (32), the AREDS (Age-Related Eye Disease Study) (33), the Japanese CCRG Cataract Grading System (34), the WHO (World Health Organization) Cataract Grading System (35), and systems quantifying posterior capsule opacification (36, 37). While all these systems grade cataracts differently, a recent study produced an algorithm to convert between cataract grading systems, and applied this method to two common systems (LOCS III and the Wisconsin Clinical and Photographic Grading System) (38).

1.4 Radiation Effects on the Eye

The structures of the eye vary in sensitivity to radiation, with the lens of the eye being one of the most radiosensitive structures and the optic nerve being one of the most radioresistant (39). With the exception of the lens, ophthalmic complications from exposure to ionizing radiation occur after receiving doses in the tens of Gray to the iris

(40, 41), sclera (41), lacrimal gland (39, 40, 42), conjunctiva (43), retina (42, 44, 45), and the optic nerve (42, 46, 47).

1.4.1 Radiation-Induced Cataractogenesis

While the exact mechanism of cataract formation from exposure to radiation is not entirely known, the initiating event is thought to occur in the epithelial cell layer (48). Radiation exposure to the germinative zone in the lens epithelium is assumed to cause damage to the genome (49, 50). It is then postulated that this genomic damage results in changes to cell division and/or lens fibre cell differentiation which ultimately expresses as cataract (49, 51).

1.5 Factors Affecting Radiation-induced Cataractogenesis

While exposure to ionizing radiation has been associated with the development of cataracts (52), there are a number of factors that influence the severity and progression of the opacities. These factors include but are not limited to the dose, fractionation, and age at exposure.

1.5.1 Dose

Radiation-induced cataracts were originally considered a tissue reaction (or deterministic effect). Tissue reactions have a threshold dose, below which the effect does not occur. The radiation dose required to produce lens opacities was thought to be 0.5-2 Gy for acute exposures (53). However, recent studies (21, 22) have shown conflicting

results concerning threshold dose estimates; this has called into question whether radiation-induced cataracts are tissue reactions or stochastic effects.

Without considering the presence of a threshold dose or lack thereof, the effect of radiation dose on severity of cataracts has been previously studied in mice exposed to 250 kVp x-rays (54). This study demonstrated that there was an increased number of lens opacities with increased dose, and these opacities progressed linearly with increasing time after irradiation (54).

1.5.2 Fractionation

Fractionation, which is a technique used to reduce normal tissue effects in radiation therapy, can have a modifying effect in radiation-induced cataractogenesis. In the animal eye, fractionated exposure to low-LET radiation (gamma- and x-rays) has been shown to affect the length of the latent period and the progression of the induced lens opacities (54-58). Additionally, studies on humans undergoing total body irradiation (TBI) have shown that fractionated TBI reduces the risk of cataract compared to single dose exposures (59-61).

1.5.3 Age

The age at exposure is also considered to be an influencing factor on radiation-induced cataractogenesis (58, 62). Studies on individuals who were exposed as children, including those receiving treatment for skin hemangiomas (63, 64) and those residing around the Chernobyl nuclear reactor (65), have shown that the young lens may be more

radiosensitive. Hall *et al.* reported that lens opacities were found in 37% of individuals exposed in infancy, compared to only 20% in the non-exposed group of the same age range (64). The effect of age on radiation cataractogensis has been supported by animal studies (66, 67), which have shown that dose and age can affect the latency and progression of radiation-induced cataracts in rats.

1.5.4 Type of Radiation

Another factor that can influence radiation-induced cataractogenesis is the type of the radiation that the lens is exposed to. While most human studies have investigated radiation-induced cataracts from exposure to low-LET (gamma- and x-ray) radiation, there have been publications on the presence and severity of cataracts in cyclotron workers exposed to neutrons (68). Animal studies have been used to study the effect of different types of radiation on cataract formation (54). Di Paola *et al.* determined that a dose of 0.17 Gy from 14-MeV neutrons produced the same number of lens opacities in mice as a 16 Gy dose from 250-kVp x-rays (54). This suggests that both the dose and type of radiation have an influence on the formation of radiation-induced cataracts.

1.6 Epidemiological Studies

There have been several epidemiological studies on cataract formation in select populations exposed to radiation. These populations include the atomic bomb survivors, Chernobyl clean-up workers and people living in the vicinity of the reactor,

radiotherapy patients, medical workers, and patients exposed to radiation from diagnostic CT.

1.6.1 Atomic Bomb Survivors

One of the most widely studied populations exposed to radiation are the survivors of the atomic bombs in Japan. There have been two recent studies on incidence of cataract in the atomic bomb survivors (21, 69). Minamoto *et al.* performed eye examinations on the atomic bomb survivors 55 years post-exposure. This study included individuals who were 13 years old or younger at the time of the bombings, and also those who had been examined in a previous study between the years of 1978 and 1980. The results of this study demonstrated that cortical and PSC cataracts in the atomic bomb survivors were significantly correlated with radiation dose (69).

Performed by Nakashima *et al.*, the second study was a reanalysis of previous data on cataract in atomic bomb survivors by using a different dosimetry system and a single ophthalmologist for re-diagnosis. Specifically, this study evaluated the presence of a threshold dose value for radiation cataractogenesis. This study estimated a dose threshold value of 0.6 and 0.7 Sv for cortical and PSC cataracts, respectively. However, the confidence intervals of their threshold dose estimates suggest that there may in fact be no threshold dose (21).

1.6.2 Chernobyl

One study investigated the presence of cataracts in the Chernobyl clean-up workers. Worgul *et al.* examined over 8600 workers 12 and 14 years post-exposure, and found that 25% of the subjects presented with PSC or cortical cataracts. This study estimated the lens doses in the workers to range from 0 to more than 1000 mGy. A dose threshold analysis was performed on the data, with the results suggesting that the dose threshold for radiation cataractogenesis is less than 1 Gy (22).

1.6.3 Individuals Exposed as Children

The studies on individuals who were exposed as children involve those residing around the Chernobyl nuclear reactor (65) and those receiving treatment for skin hemangiomas (64). Day *et al.* studied the incidence of cataracts in a pediatric population that were living in the permanent control zone around the Chernobyl nuclear reactor compared to an unexposed control population. The results of this study showed that there was a small, statistically significant excess of subclinical PSC opacities in the exposed group compared to the control (65).

Hall *et al.* investigated the lens opacities in individuals exposed to ionizing radiation in childhood. The exposed population was comprised of individuals who had received radiotherapy for skin hemangiomas when they were less than 18 months old. This study reported that lens opacities were found in 37% of individuals exposed in infancy, compared to only 20% in the non-exposed group of the same age range (64).

1.6.4 Medical Workers

There have been numerous studies on cataract incidence in medical workers, including radiologic technologists (70), interventional cardiology personnel (71, 72), and physicians exposed to ionizing radiation (73). Chodick *at al.* performed a prospective cohort study of over 35,000 radiologic technologists in the United States. At the start of the study, these subjects were aged 22 to 44 years old, and they were followed for 20 years. The findings of this study suggest that increased exposure to radiation increases the possibility of cataract formation. Additionally, they noted that their findings suggest there may be no apparent threshold for radiation cataractogenesis (70).

Two studies investigated the incidence of cataracts among interventional cardiology personnel (71, 72). Vano *et al.* performed eye examinations on interventional cardiologists, associated workers in the department, and an unexposed control group. They determined that PSC cataracts were present in 32% of the interventional cardiologists and 21% of the nurses and technicians compared to 12% in the control group (71). Jacob *et al.* studied the incidence of cataracts in interventional cardiologists at different medical centers in France compared to an unexposed, non-medical worker control group. Similar to Vano *et al.* (71), they found that PSC were present in 17% of the interventional cardiologists compared to 5% in the control group (72).

Lastly, Mrena *et al.* conducted a study that investigated the incidence of cataracts in physicians exposed to ionizing radiation. The physicians ranged in age from 45 to 70

years and included 29 radiologists, 11 interventional radiologists, 16 cardiologists, and 1 surgeon. This study found that 42% of the physicians had lens opacities, and the most prevalent opacity was nuclear (14% of subjects), followed by cortical (7%) and finally PSC (5%) (73). While nuclear cataracts are not typically associated with exposure to ionizing radiation, they are associated with age. Since the age of the physicians ranged from 45 to 70, this may be an explanation for the high percentage of nuclear cataracts observed in this study.

The main limitation of all of these studies is that they relied on questionnaires to gather information on medical history and work practices. This type of data is purely anecdotal and can often be unreliable. Additionally, lens doses were either estimated from occupational radiation badge readings and anecdotal information on work practices from the questionnaires (70, 71, 73), or they were not estimated at all (72).

1.6.5 Patients Exposed to Radiation from Diagnostic CT

One of the first studies on exposure to diagnostic x-rays and cataracts was a population-based study in the town of Beaver Dam, Wisconsin (74). This study, along with a 5-year follow up study of the participants (75), found a significant relationship between history of x-ray exposures and PSC cataract. However, the limitations of the study were that the radiology history of each subject was self-reported and only a sample of the subjects had their medical records reviewed by the senior investigator for accuracy.

A few years later, the Blue Mountains Eye Study investigated the presence of cataracts and the history of head CT scans in an urban Australian population (76). Unlike the Beaver Dam Eye Study, the results of this study suggested there was no significant association between cataracts and head CT exposures. However, once again, this study only polled the participants on their exposure history and did not validate the self-reports of head CT scans.

More recently, the risk of cataract associated with repeated head/neck CT scans was investigated in a nationwide population-based study in Taiwan (77). The participants in this study were enrolled in the Taiwan National Health Insurance Research Database, which allowed for direct access to their complete exposure histories. The findings of this study suggested that cataract incidence increases gradually with increasing frequency of CT examinations.

1.6.6 Cataract Threshold Dose Evaluation

There have only been a handful of epidemiological studies to estimate an actual dose threshold. These include the reanalysis of the atomic bomb data by Nakashima *et al.* (21) and the study on the Chernobyl clean-up workers by Worgul *et al.* (22). In the atomic bomb survivor study, the results show that the dose threshold was 0.6 and 0.7 Sv for cortical and PSC cataracts, respectively. However, the 90% confidence intervals are quite large, ranging from <0 to 1.2 Sv for cortical cataracts and <0 to 2.8 Sv for PSC cataracts (21).

The study on the Chernobyl clean-up workers estimated that the cataract dose threshold is less than 1 Gy, with their data pointing to an upper limit dose threshold of 0.7 Gy (22). However, like the study on the atomic bomb survivors, there is likely to be considerable uncertainty in the dose estimates, which results in a great deal of uncertainty in dose threshold estimates. While it may appear from these two studies that the dose threshold is lower than 1 Gy, further investigation into this area is warranted before any specific conclusions are made about a dose threshold.

1.7 Viewpoints on Radiation-induced Cataractogenesis

1.7.1 International Commission on Radiological Protection

The International Commission on Radiological Protection (ICRP) is an organization that provides recommendations on different aspects of radiation protection. They have published numerous reports on threshold values for radiation-induced cataractogenesis (53, 56, 78-80). In light of the recent studies suggesting cataracts may form at doses lower than previously expected, the most recent of these recommendations in ICRP Publication 118 states that the threshold dose for radiation-induced cataract after acute or protracted exposures is now assumed to be 0.5 Gy (56, 81). Prior to this, doses of 0.5-2 Gy and 5 Gy were thought to have caused detectable opacities in the lens from acute and protracted exposures, respectively (53). Additionally, in Publication 118, the ICRP recommended that the equivalent lens dose limit to occupationally exposed persons be reduced to 20 mSv/year averaged over 5

years, with no single year exceeding 50 mSv; the dose limit for members of the public remained the same (15 mSv/year) (56). The previous lens dose limit to occupational workers was 150 mSv/year (53, 79). Reducing the lens dose limit by a factor of 7.5 would have clear regulatory implications, requiring more accurate methods of monitoring lens doses and better protective measures.

1.7.2 National Council on Radiation Protection and Measurements

The National Council on Radiation Protection and Measurements (NCRP), which is an organization that provides guidance radiation protection issues, has also released several reports regarding the effects of radiation on the lens of the eye (82-88). Early on, these reports identified radiation-induced cataractogenesis as a deterministic effect (82). Exposure limits to the lens of the eye for both occupationally exposed persons and members of the public were based on the prevention of the deterministic effects (84, 85). More recently, the NCRP reported that radiation-induced cataracts may in fact be a stochastic effect, with no dose threshold (87). The NCRP noted in their latest report that the current occupational dose limits (150 mGy/year) should be reassessed (88) and they are expected to publish an updated commentary sometime in 2016 on these issues as well as addressing the conclusions about threshold doses and lens dose limits noted in ICRP Publication 118.

1.8 Gaps in Knowledge

Questions still remain about the presence of a dose threshold in radiation cataractogenesis. Since a limited number of studies have estimated dose thresholds and the results of these studies have high uncertainties, more accurate dosimetry models and continued follow-up on populations already studied may provide more information regarding this topic. Additionally, new studies on populations exposed to protracted doses may be very useful in this area as well.

The Electric Power Research Institute (EPRI) recently published a meta-analysis on all epidemiological studies related to radiation cataractogenesis. In this, they suggested criteria for improvement in the methodologies of future studies on cataract threshold dose analysis (89). These criteria include accurate lens dosimetry models as well as methods to extract complete records of exposure history and type. Since the exposure history from diagnostic CT exams is well documented in a patient's medical record, the population of patients chronically exposed to radiation from head CT studies may be an interesting area to explore for further research in radiation cataractogenesis. Since children are more susceptible to the effects of radiation, the pediatric patient population is an important cohort to study because about 70% of pediatric CT scans are of the head (90).

1.8.1 Challenges in Lens Dose Estimation in Individuals Receiving Head CT Exams

While individuals exposed to radiation from diagnostic CT are an interesting population for studies in this area, there are some challenges in estimating lens dose from head CT exams. At a given institution, there are often a variety of head imaging protocols that use different technical factors (i.e. tube current, slice thickness, pitch, etc.) based upon the anatomy to be imaged. Anatomical features of the head that are frequently imaged by CT include the brain, sinuses, orbits, facial bones, and temporal bones. It is expected that the lens dose will vary among different imaging protocols, as well as vary based upon the size of the patient getting imaged. Since CT imaging is a highly dynamic field, it is also likely that protocols change over time. Additionally, there are different lens dose reduction methodologies that can be implemented in head imaging protocols, such as organ-based tube current modulation (OB-TCM) or tilting the gantry to avoid the orbit in brain imaging. Therefore, an accurate lens dosimetry model would then account for differences in imaging protocols, differences in head size, and the use of any dose reduction methods.

In addition to an accurate dosimetry model, knowledge of all exposures to radiation from head CT is required in order to estimate the lens dose in any given individual. Before the advent of electronic medical records (EMRs), this information would have been solely based upon exposure history questionnaires. Since an EMR at a given institution contains all information regarding imaging exams that took place there,

this can provide somewhat more of an accurate exposure history rather than a questionnaire. However, this may not be the complete exposure history picture as the individuals could have received imaging exams at outside institutions, such as outpatient clinics or other hospitals.

1.8.2 Objectives and Scope of Research

The overall goal of this project is to derive an accurate model to estimate the lens dose from head CT scans and to determine a methodology to reconstruct cumulative lens dose from head CT scans in patients at our institution. To achieve this, a standard CT dose metric ($CTDI_{vol}$) will be used to account for any differences in head imaging protocols (Chapter 2). The effect of OB-TCM (Chapter 3) and gantry angulation (Chapter 4) will also be accounted for in this dosimetry model. The use of $CTDI_{vol}$ is advantageous because it is recorded in a patient's EMR for each CT imaging exam. So, finally, retrospective reviews of medical records will be performed in the pediatric (Chapter 5) and adult (Chapter 6) populations at our institution. These retrospective studies will collect head CT exam information, including $CTDI_{vol}$, for selected patients from the two populations and reconstruct lens doses using the dosimetry model derived in Chapters 2 through 4.

2. A Method to Estimate the Radiation Dose to the Lens of the Eye using the $CTDI_{vol}$

2.1 Introduction

Radiation dose to the lens of the eye from CT is expected to vary depending on the type of imaging protocol, the scanner model, and the age of the patient receiving the exam. Recent studies have showed that the lens dose in pediatric head CT can range from 8.2 to 143.3 mGy (91-94). For CT imaging of the head in adults, the lens dose has been shown to range from 25.1 to 103.5 mGy (95-98). Additionally, studies have shown that there is an inter-institutional variability in the dose to the lens from head CT based upon the scanner make and model (95, 96). One potential method for estimating patient-specific lens doses without the knowledge of the scanner model is through the use of the CT dose index.

2.1.1 Measurement of $CTDI_{vol}$

The CT dose index represents the average dose in a cylindrical phantom from a single scan and is used as a standardized dose metric for CT imaging protocols (99). The dose index commonly reported by scanners is the volumetric CT dose index ($CTDI_{vol}$). $CTDI_{vol}$ is measured using a polymethyl methacrylate (PMMA) cylindrical phantom that has a diameter of either 16 cm or 32 cm, which represent the head or the body, respectively. A 100-mm pencil ion chamber is placed in five different locations within the phantom (Figure 2.1). Four of these are peripherally located within the phantom and

are represented by letters “B” through “E” in Figure 2.1. There is one central location, which is represented by the letter “A” in Figure 2.1.

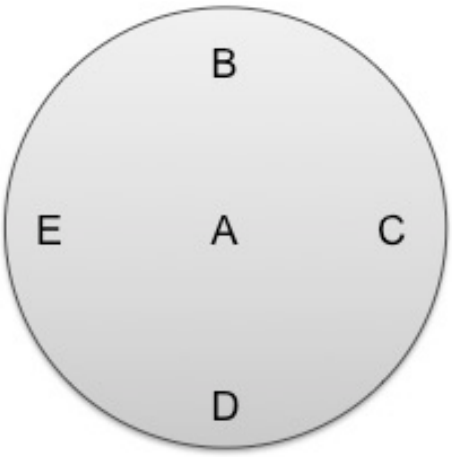

Figure 2.1: Schematic of the CTDI phantom

The phantom is scanned with a standard protocol for either head or body imaging, and ion chamber measurements are taken at each of the 5 locations in the phantom. The radiation dose in a 100-mm long section of the phantom in the z-axis is given by equation 2.1.

$$CTDI_{100} = \left(\frac{1}{NT}\right)\int_{-50\,mm}^{+50\,mm} D(z)\,dz \qquad (2.1)$$

In this equation, N is the number of slices for a single scan, T is the slice thickness, and D(z) is the z-axis dose profile for a single scan calculated from the ion chamber measurements.

The $CTDI_{vol}$ is then calculated from the central and peripheral $CTDI_{100}$ values with equation 2.2.

$$CTDI_{vol} = \frac{\left(\frac{2}{3}\right)CTDI_{100,peripheral} + \left(\frac{1}{3}\right)CTDI_{100,center}}{pitch} \quad (2.2)$$

In this equation, the peripheral CTDI ($CTDI_{100,peripheral}$) value is calculated as the average of the measurements made in locations B through E., the center CTDI ($CTDI_{100,center}$) is the ion chamber measurement at location A, and the pitch of the scan is the distance traveled by the table per rotation divided by the beam collimation (100).

The above section describes the measurements required to calculate $CTDI_{vol}$, but for each patient exam, the $CTDI_{vol}$ is estimated from look-up tables by the scanner based upon the exposure parameters for a given protocol.

2.1.2 Studies on CTDIvol-to-Organ Dose Estimation Methods

The use of $CTDI_{vol}$ provides a measure of scanner output that takes into account all technical parameters and allows for benchmarking of radiation dose against national averages for a given examination. However, since $CTDI_{vol}$ represents the average dose in either a 16 or 32 cm diameter cylindrical PMMA phantom (100), it is well understood that this value should not be used for patient-specific dose estimates (101), which are dependent upon scanner output and patient size. A recent study produced scanner-independent $CTDI_{vol}$-to-organ dose conversion coefficients for whole body CT scans (102). This method was extended to include size-specific conversion coefficients for abdominal CT examinations (103), which was expanded upon by AAPM Task Group 204 (104). Similar methods were used to measure $CTDI_{vol}$-to-organ dose conversion

coefficients for axial and helical head CT examinations (105). However, the last study focused solely on the lens dose from the routine brain imaging protocol. Since exposure parameters vary based upon the anatomy to be imaged, the first aim of this study was to measure the lens dose in phantoms of different sizes from a variety of different head imaging protocols used at our institution. The second aim was to determine a patient size-specific method to estimate lens dose from $CTDI_{vol}$.

2.2 Materials and Methods

2.2.1 CT Scanners and Beam Data

The two scanners used for data collection include the Discovery 750 HD CT scanner (*GE Healthcare*, Waukesha, WI) and the SOMATOM Definition Flash CT scanner (*Siemens Healthcare*, Erlangen, Germany); pictures of these scanners are shown in Figures 2.2a and 2.2b, respectively. At the time of data collection, these scanners represented the newest models from both manufacturers at our institution. An overview of the technical specifications of these systems is given in Table 2.1

Table 2.1: Overview of the system specifications of the two scanners used for dose measurements

Scanner	Tube voltage settings (kV)	Tube current range (mA)	Number of detector rows	Rotation times (s)
Discovery 750 HD	80, 100, 120, 140	10-835	64 x 0.625 mm	0.35-2
SOMATOM Definition Flash	80, 100, 120, 140	20-800	64 x 0.6 mm	0.28-1

a)

b)

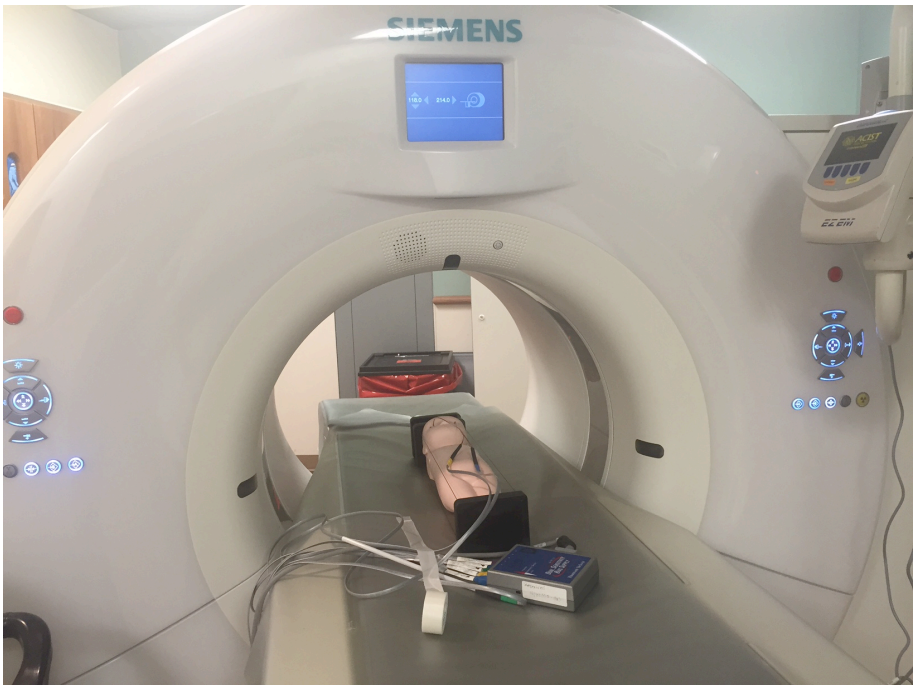

Figure 2.2: Picture of the newborn anthropomorphic phantom on the a) Discovery 750 HD CT scanner and b) SOMATOM Definition Flash CT scanner

For radiation dosimetry purposes, it is imperative to know the quality of the beam for a given CT scanner. Quantities that describe the quality of the beam include the tube voltage, the half-value layer (HVL), and total filtration (TF). The HVL is the filtration necessary to reduce the beam to one half of its original intensity. The TF is the sum of the inherent filtration (the window of the x-ray tube) and the added filtration (any filter added in between the tube housing and the collimator) of the x-ray tube; filtration eliminates low-energy photons that contribute to patient dose but not to image formation. To measure these quantities, the Piranha 557 (*RTI Electronics*, Molndal, Sweden), which is a x-ray quality control meter, was placed in the beam of both the Discovery 750 HD and SOMATOM Definition Flash scanners. The CT tube was operated in planar scan mode with the tube fixed at the top of the gantry, which corresponds to an anterioposterior (AP) projection. The scan parameters and measured tube voltage, HVL, and TF for each scanner are listed in Table 2.2.

Table 2.2: Scan parameters and beam quality measurements

Scanner	Scan Parameters	Tube Voltage (kV)	HVL (mm Al)	TF (mm Al)
Discovery 750 HD	120 kV, 10 mAs	118.3	7.53	9.3
SOMATOM Definition Flash	120 kV, 10 mAs	115.0	7.60	10.0

2.2.2 Anthropomorphic Phantoms and Head Imaging Protocols

Six anthropomorphic phantoms (*CIRS*, Norfolk, VA) were used for all radiation dose measurements. The representative ages of the six phantoms were newborn (Model 703-D), 1-year-old (Model 704-D), 5-year-old (Model 705-D), 10-year-old (Model 706-D), adult female (Model 702-D), and adult male (Model 701-D). The phantoms are comprised of materials that simulate different tissue types, including bone, soft tissue, spinal cord, spinal disks, lung, and brain (106). The phantoms are made of 2.5 cm thick individual contiguous slabs. Relevant data related to the phantoms is listed in Table 2.3. The 5-year-old through adult male phantoms do not have leg attachments, which is why the total number of slabs is greater for the 1-year-old compared to the 5-year-old.

Table 2.3: Relevant data related to the anthropomorphic phantoms. The phantoms were designed to be representative of humans with the heights and weights listed in this table.

Phantom	Height (cm)	Weight (kg)	Total number of slabs
Newborn	51	3.5	20
1-year-old	75	10	29
5-year-old	110	19	26
10-year-old	140	32	32
Adult female	160	55	38
Adult male	173	73	39

The individual slabs contain predrilled holes for placement of radiation detectors. For dose measurement in all six phantoms, one high-sensitivity Model TN-1002RD (*Best Medical*, Canada) metal oxide semiconductor field-effect transistor

(MOSFET) was placed in each predrilled location for the lens of the eye (Figure 2.3). MOSFET detectors have been previously validated against thermoluminescent dosimeters (TLDs) for organ dose measurement (107).

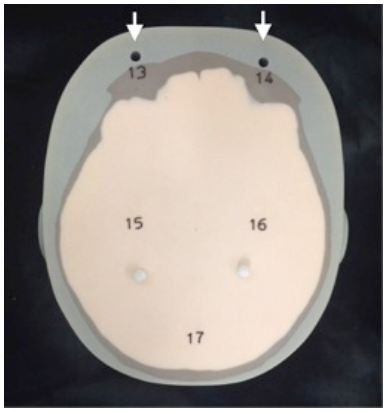

Figure 2.3: Location of predrilled holes for dosimeter placement in 10-year-old phantom

Each phantom was scanned with five different head imaging protocols at 120 kV. These protocols have different exposure techniques based upon the area of anatomy to be imaged. Factors that change among the different protocols include the tube current, field of view (FOV), pitch, scan length, $CTDI_{vol}$, and dose length product (DLP). The protocol parameters for the Discovery 750 HD scanner and the SOMATOM Definition Flash scanner are listed in Table 2.4 and Table 2.5, respectively. There was one extra protocol that the newborn and 5-year-old phantoms were scanned with on the Discovery 750 HD scanner; this is the Craniofacial HD protocol, which is the same as the Craniofacial protocol but with increased tube current. Examples of how the scan range varies among protocols are shown in Figure 2.4a-d.

Table 2.4: Protocol parameters for the Discovery 750 HD scanner

Phantom	Protocol	Tube Current (mAs/rot)	FOV (cm)	Pitch	$CTDI_{vol}$ (mGy)	DLP (mGy-cm)
Newborn	Brain	25.0	18.0	Axial	4.5	44.5
	Sinus	42.5	15.0	Axial	7.6	45.4
	Facial Bones	70.0	15.0	Axial	12.5	99.6
	Orbits	70.0	15.0	Axial	12.5	49.8
	Craniofacial	24.5	20.0	0.97	4.9	72.1
	Craniofacial HD	98.0	20.0	0.97	19.6	293.5
1-year-old	Brain	25.0	20.0	Axial	4.5	53.4
	Sinus	42.5	15.0	Axial	7.6	45.4
	Facial Bones	70.0	15.0	Axial	12.5	149.5
	Orbits	70.0	15.0	Axial	12.5	99.6
	Craniofacial	24.5	20.0	0.97	4.9	88.3
5-year-old	Brain	77.5	22.0	Axial	13.8	165.5
	Sinus	70.0	16.0	Axial	12.5	124.5
	Facial Bones	87.5	16.0	Axial	15.6	217.9
	Orbits	87.5	16.0	Axial	15.6	124.5
	Craniofacial	24.5	20.0	0.97	4.9	101.1
	Craniofacial HD	98.0	20.0	0.97	19.8	404.1
10-year-old	Brain	100.0	22.0	Axial	20.0	279.5
	Sinus	97.5	16.0	Axial	19.5	155.7
	Facial Bones	167.5	16.0	Axial	33.4	468.1
	Orbits	126.0	16.0	Axial	25.2	150.9
	Craniofacial	167.5	24.0	0.97	33.6	740.6
Adult female	Brain	167.5	22.0	Axial	33.4	468.1
	Sinus	105.0	16.0	0.97	20.7	243.6
	Facial Bones	125.0	16.0	0.97	24.9	412.2
	Orbits	105.0	16.0	0.97	19.8	119.5
	Craniofacial	167.5	24.0	0.97	33.7	802.0
Adult male	Brain	167.5	22.0	Axial	33.4	468.1
	Sinus	105.0	16.0	0.97	20.8	249.7
	Facial Bones	125.0	16.0	0.97	25.0	412.7
	Orbits	105.0	16.0	0.97	20.1	136.1
	Craniofacial	167.5	24.0	0.97	33.8	862.3

Table 2.5: Protocol parameters for the SOMATOM Definition Flash scanner

Phantom	Protocol	Tube Current (mAs/rot)	FOV (cm)	Pitch	$CTDI_{vol}$ (mGy)	DLP (mGy-cm)
Newborn	Brain	48.0	15.0	0.60	12.0	123.0
	Sinus	30.0	15.0	0.60	7.4	41.0
	Facial Bones	60.0	15.0	0.60	15.0	86.0
	Orbits	42.0	15.0	0.60	10.5	53.0
	Craniofacial	24.0	15.0	0.60	6.1	87.0
1-year-old	Brain	48.0	18.0	0.60	12.2	166.1
	Sinus	30.0	22.0	0.60	7.7	58.6
	Facial Bones	60.0	18.0	0.60	15.3	207.1
	Orbits	42.0	15.0	0.60	10.7	86.2
	Craniofacial	24.0	20.0	0.60	6.1	107.3
5-year-old	Brain	48.0	22.0	0.60	12.0	195.0
	Sinus	30.0	15.0	0.60	7.6	84.0
	Facial Bones	60.0	20.0	0.60	15.0	224.0
	Orbits	42.0	15.0	0.60	10.5	104.0
	Craniofacial	24.0	22.0	0.60	6.1	118.0
10-year-old	Brain	157.0	22.0	0.55	44.2	726.0
	Sinus	55.0	15.0	0.55	15.0	154.0
	Facial Bones	110.0	16.0	0.55	30.3	558.0
	Orbits	110.0	16.0	0.55	30.3	328.0
	Craniofacial	110.0	24.0	0.55	30.3	631.3
Adult female	Brain	124.0	22.0	0.55	34.2	529.3
	Sinus	55.0	16.0	0.55	15.0	188.8
	Facial Bones	110.0	16.0	0.55	30.3	526.3
	Orbits	110.0	15.0	0.55	30.3	217.2
	Craniofacial	110.0	24.0	0.55	30.3	766.8
Adult male	Brain	124.0	22.0	0.55	34.2	594.1
	Sinus	55.0	16.0	0.55	15.0	226.1
	Facial Bones	110.0	16.0	0.55	30.3	526.4
	Orbits	110.0	15.0	0.55	30.3	217.3
	Craniofacial	110.0	24.0	0.55	30.3	743.1

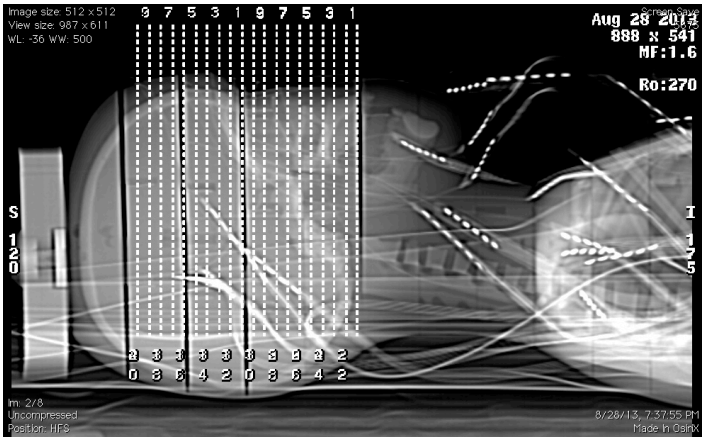
Image size: 512 x 512
View size: 987 x 611
WL: -36 WW: 500
Aug 28 2013
888 x 541
MF:1.6
Ro:270
S
I
Im: 2/8
Uncompressed
Position: HFS
8/28/13, 7:37:55 PM
Made in OsiriX

a)

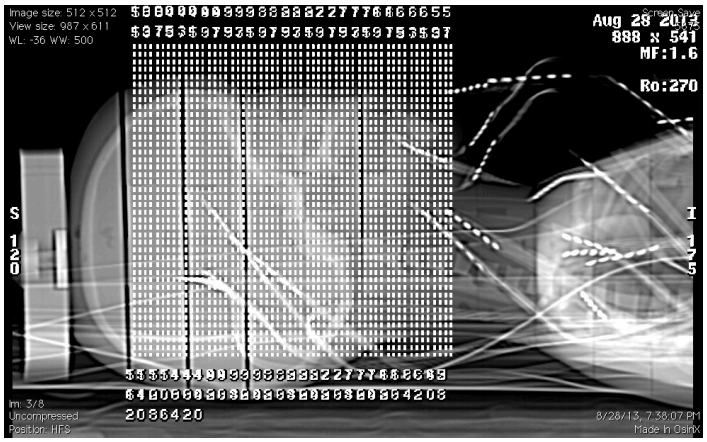
Image size: 512 x 512
View size: 987 x 611
WL: -36 WW: 500
Aug 28 2013
888 x 541
MF:1.6
Ro:270
S
I
Im: 3/8
Uncompressed
Position: HFS
8/28/13, 7:38:07 PM
Made in OsiriX

b)

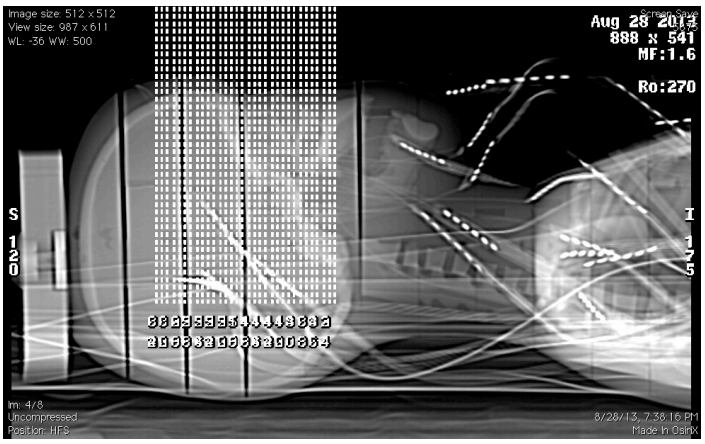
Image size: 512 x 512
View size: 987 x 611
WL: -36 WW: 500
Aug 28 2013
888 x 541
MF:1.6
Ro:270
S
I
Im: 4/8
Uncompressed
Position: HFS
8/28/13, 7:38:16 PM
Made in OsiriX

c)

d) 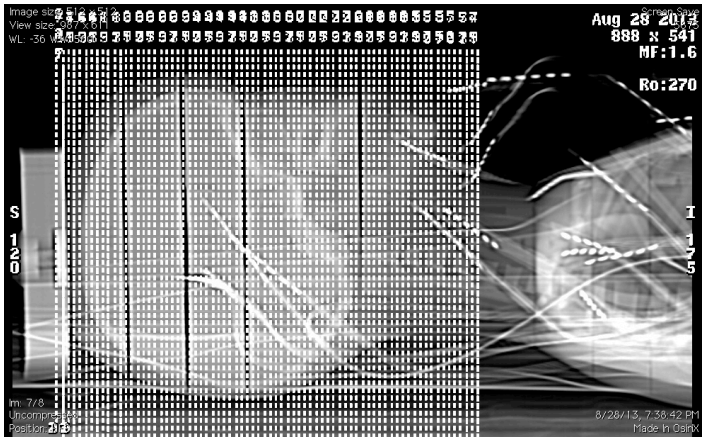

Figure 2.4: Scan range for the a) sinus, b) facial bones, c) orbits, and d) craniofacial protocols on the Discovery 750 HD scanner. In these figures, the placement of the dashed lines indicates the z-axis location of each image slice in the scan. The density of the dashed lines is related to the slice thickness; the less number of lines within a given scan range indicates a larger slice thickness. The y-axis length of the dashed lines indicates the reconstruction field of view (FOV); smaller FOVs reduce the pixel size, which helps to increase the spatial resolution. The wires are associated with the MOSFET dosimeters, and the rectangular piece to the left of the head is the top of the phantom's reinforcement base.

2.2.3 MOSFET Calibration

Calibration of the MOSFET dosimeters was necessary in order to convert the raw millivolt readings measured by the dosimeter to absorbed dose in soft tissue. The calibration procedure involved simultaneously exposing MOSFETs and an ion chamber calibrated by an Accredited Dosimetry Calibration Laboratory (ADCL) to a 120 kV x-ray beam of the same quality as that used during dose measurements. The experimental set-up involved placing the MOSFETs adjacent to the active volume of the ion chamber, which was positioned at the isocenter of the beam (Figure 2.5). The MOSFETs and ion chamber were positioned on a piece of 2.0 cm thick Plexiglas to simulate backscatter. A

piece of radiochromic film was placed under the calibration set-up to ensure that the ion chamber and all MOSFETs were positioned within the beam.

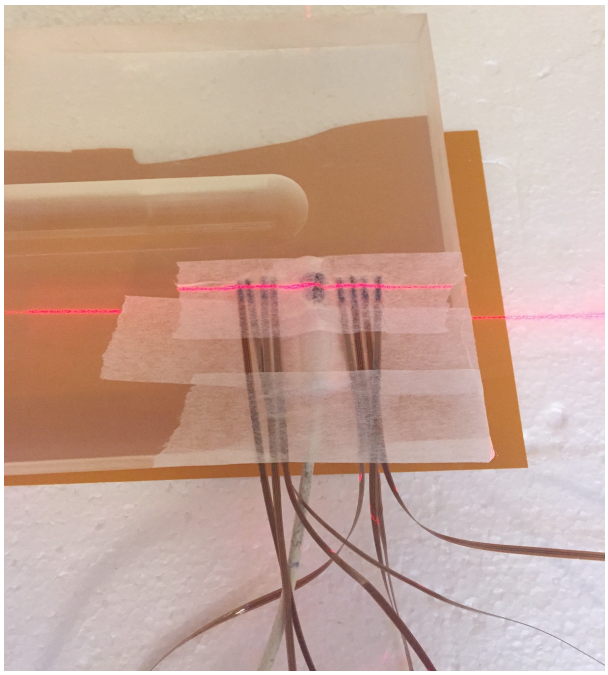

Figure 2.5: Picture of the MOSFET calibration set-up. The ion chamber is placed within a groove in the Plexiglas block, and is positioned at the isocenter of the CT gantry. The MOSFETs are placed on top of the block adjacent to the center of the ion chamber.

Once the irradiation was complete, the voltage was read off of the MOSFET detectors with the AutoSense™ PC Software (TN-RD-45), and the calibration factors were calculated using equation 2.3:

$$CF_{MOSFET} = \frac{\Delta V}{CF_{IC} \times f \times Rdg_{IC}} \tag{2.3}$$

In equation 2.3, CF_{MOSFET} is the individual calibration factors for each MOSFET (units: mV/cGy), ΔV is the voltage shift measured by each MOSFET in mV, CF_{IC} is the ion

chamber calibration factor (units: Roentgen/reading), f is the f-factor for soft tissue, and Rdg_{IC} is the raw ion chamber reading.

The f-factor is used to relate the absorbed dose measured in one medium to that of a different medium from a radiation beam of the same mono-energetic energy. For this experiment, the f-factor was calculated using the mass energy absorption coefficient of soft tissue and air at the effective energy of the CT beam (equation 2.4).

$$f = 0.876 \times \frac{\left(\frac{\mu_{en}}{\rho}\right)_{\text{soft tissue}}}{\left(\frac{\mu_{en}}{\rho}\right)_{\text{air}}} \tag{2.4}$$

Since diagnostic x-ray equipment emits radiation with a spectrum of energies, the mono-energetic effective energy is used as the measure of beam quality when determining the mass energy absorption coefficients for the f-factor calculation. To determine the effective energy of the CT beams for each scanner at 120 kV, the measured HVL (Table 2.2) and information about each x-ray tube was input into the SpekCalc beam spectrum simulation software (108-110). The effective energy, which is the energy of a monoenergetic beam that will produce the same first HVL as the CT beam (110), for each scanner at 120 kV, as well as the calculated f-factor is listed in Table 2.6.

Table 2.6: Scanner-specific effective energy and f-factors

Scanner	Effective Energy (keV)	f-factor (cGy/R)
Discovery 750 HD	52.5	0.934
SOMATOM Definition Flash	52.7	0.934

2.2.4 Dose Measurements

On each scanner, radiation dose was measured in the six phantoms for the protocols listed in Tables 2.4 and 2.5. After irradiation, the voltage was read off of the MOSFET detectors with the AutoSense™ PC Software. This software applies the individual MOSFET calibration factors (in mV/cGy) directly to the raw voltage readings (in mV) to obtain the absorbed dose (in cGy) using equation 2.5:

$$Dose\ (cGy) = \frac{\Delta V\ (mV)}{CF\ \left(\frac{mV}{cGy}\right)} \tag{2.5}$$

The dose measurements were exported to an Excel file after each run of a protocol; there were three runs for each imaging protocol. Since the lower limit of detection of the MOSFETs required to achieve about 10% uncertainty among multiple measurements is just under 0.5 cGy (107), scans were repeated as many as three times for each run in some cases to ensure the total voltage shift measured by the MOSFET

would correspond to at least that dose level. The average lens dose and standard deviation were calculated for each protocol from the three runs.

2.2.5 Definition of Age-Specific $CTDI_{vol}$-to-Lens Dose Conversion Factors

In order to determine the $CTDI_{vol}$-to-lens dose conversion factors, the $CTDI_{vol}$ values for each protocol were recorded from the structured dose report generated by the scanner. The contents of the structured dose report vary by scanner manufacturer, but they typically contain the two common dose indices ($CTDI_{vol}$ and DLP) and the phantom used to calculate those quantities (the 16 cm or 32 cm CTDI phantom) for each imaging series. Examples of a structured dose reports for the Discovery 750 HD and SOMATOM Definition Flash are shown in Figures 2.6 and 2.7, respectively.

Patient Name: GE ADULT NEURO — Exam no: 12230
Accession Number: — Jun 16 2015
Patient ID: ZZZZZZ — Discovery CT750 HD
Exam Description:

Dose Report

Series	Type	Scan Range (mm)	CTDIvol (mGy)	DLP (mGy-cm)	Phantom cm
1	Scout	-	-	-	-
2	Axial	I12.250-S127.515	32.30	468.14	Head 16
3	Axial	I12.250-S127.515	32.30	468.14	Head 16
4	Axial	I12.250-S127.515	32.30	468.14	Head 16
5	Helical	I105.500-S127.000	33.78	862.47	Head 16
9	Helical	I105.500-S127.000	33.81	863.13	Head 16
13	Helical	I105.500-S127.000	33.74	861.43	Head 16
14	Axial	I12.250-S129.305	15.71	230.58	Head 16
14	Axial	I12.250-S129.305	15.71	230.58	Head 16
15	Axial	I12.250-S129.305	15.71	230.58	Head 16

1/5

Figure 2.6: Structured dose report from the Discovery 750 HD scanner

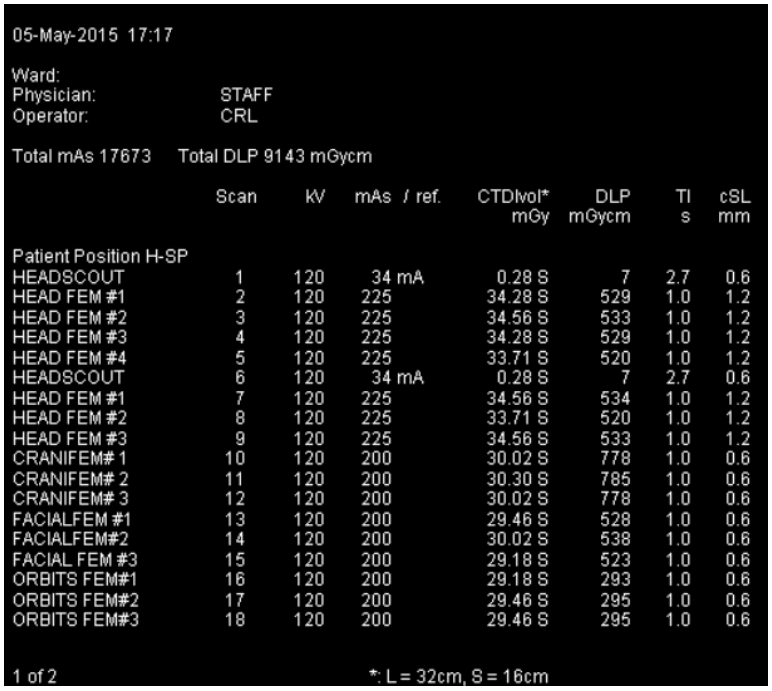

05-May-2015 17:17

Ward:
Physician: STAFF
Operator: CRL

Total mAs 17673 Total DLP 9143 mGycm

	Scan	kV	mAs / ref.	CTDIvol* mGy	DLP mGycm	TI s	cSL mm
Patient Position H-SP							
HEADSCOUT	1	120	34 mA	0.28 S	7	2.7	0.6
HEAD FEM #1	2	120	225	34.28 S	529	1.0	1.2
HEAD FEM #2	3	120	225	34.56 S	533	1.0	1.2
HEAD FEM #3	4	120	225	34.28 S	529	1.0	1.2
HEAD FEM #4	5	120	225	33.71 S	520	1.0	1.2
HEADSCOUT	6	120	34 mA	0.28 S	7	2.7	0.6
HEAD FEM #1	7	120	225	34.56 S	534	1.0	1.2
HEAD FEM #2	8	120	225	33.71 S	520	1.0	1.2
HEAD FEM #3	9	120	225	34.56 S	533	1.0	1.2
CRANIFEM# 1	10	120	200	30.02 S	778	1.0	0.6
CRANIFEM# 2	11	120	200	30.30 S	785	1.0	0.6
CRANIFEM# 3	12	120	200	30.02 S	778	1.0	0.6
FACIALFEM #1	13	120	200	29.46 S	528	1.0	0.6
FACIALFEM#2	14	120	200	30.02 S	538	1.0	0.6
FACIAL FEM #3	15	120	200	29.18 S	523	1.0	0.6
ORBITS FEM#1	16	120	200	29.18 S	293	1.0	0.6
ORBITS FEM#2	17	120	200	29.46 S	295	1.0	0.6
ORBITS FEM#3	18	120	200	29.46 S	295	1.0	0.6

1 of 2 *: L = 32cm, S = 16cm

Figure 2.7: Structured dose report from the SOMATOM Definition Flash scanner

For each phantom, linear regression analysis was used to determine the relationship between the measured lens dose, D_{lens}, and the $CTDI_{vol}$ values retrieved from the structured dose reports in the form of equation 2.6:

$$D_{lens} = CF_{age} \times CTDI_{vol} \tag{2.6}$$

In this equation, CF_{age} is the slope of the linear fit and will serve as the age-specific $CTDI_{vol}$-to-lens dose conversion factor for each phantom. This was done for the phantom data collected on each scanner separately. To determine the feasibility of a scanner-independent (SI) conversion factor for each phantom, this procedure was repeated for each phantom by combining the dose data measured on both scanners. A flow chart explaining the methodology to derive the CF_{age} for each phantom is shown in Figure 2.8.

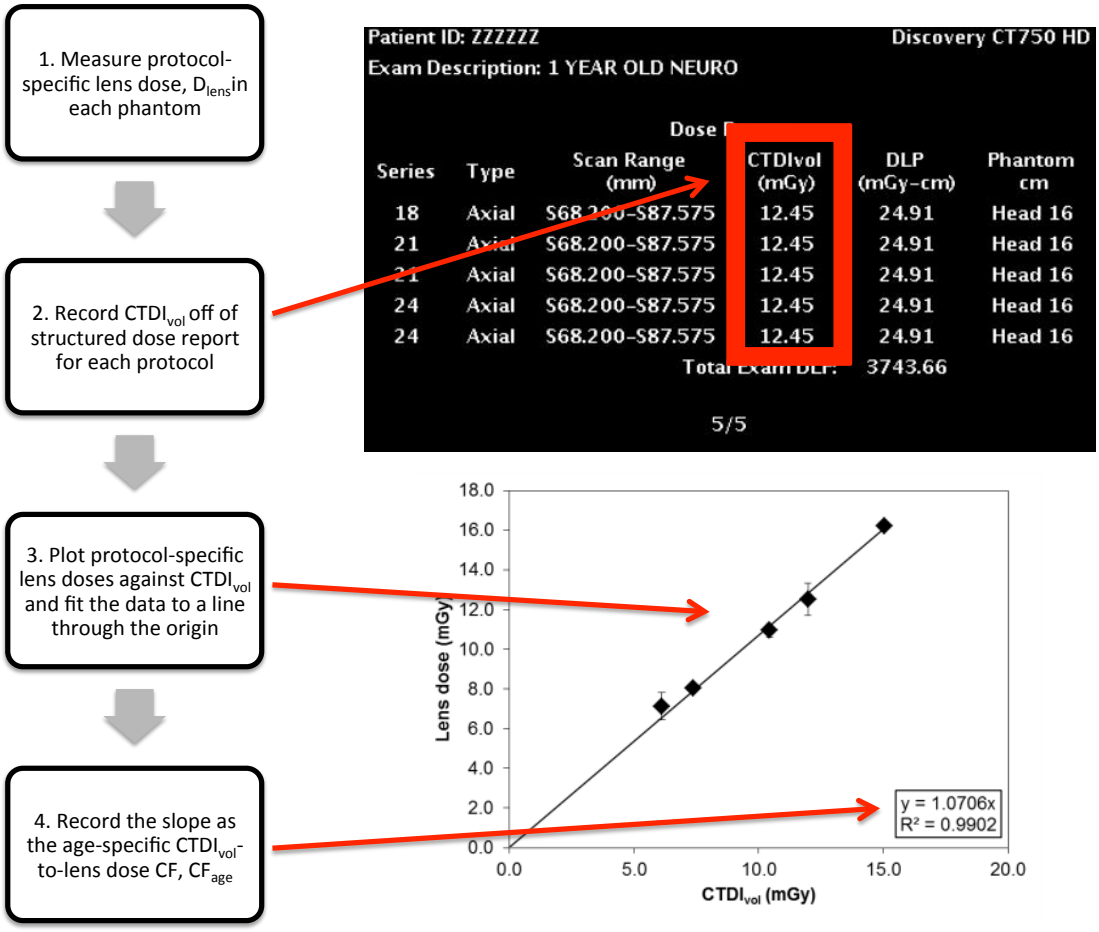

Figure 2.8: Methods to derive the age-specific $CTDI_{vol}$-to-lens dose CF (CF_{age}). This method was repeated for the data from each phantom on each scanner. To determine the scanner-independent CF_{age}, the lens dose and $CTDI_{vol}$ data from both scanners collected in steps 1 and 2 were plotted on the same graph for step 3 and the slope of the line (step 4) was the SI CF_{age} for each phantom.

2.2.6 Definition of Size-Specific $CTDI_{vol}$-to-Lens Dose Conversion Factors

Recent studies have shown that an exponential relationship exists between doses normalized to $CTDI_{vol}$ and patient size for different CT examinations, most likely due to the exponential nature of attenuation (102, 103, 105). Therefore, the relationship between $CTDI_{vol}$-to-lens dose CF and head size was investigated using the phantom data from

this study. To calculate the head size of each phantom, the anterioposterior (AP) and lateral (LAT) diameters were measured on an axial image in the supraorbital region of the head (Figure 2.9). The effective diameter was then calculated by taking the square root of the product of the AP and LAT dimensions (104).

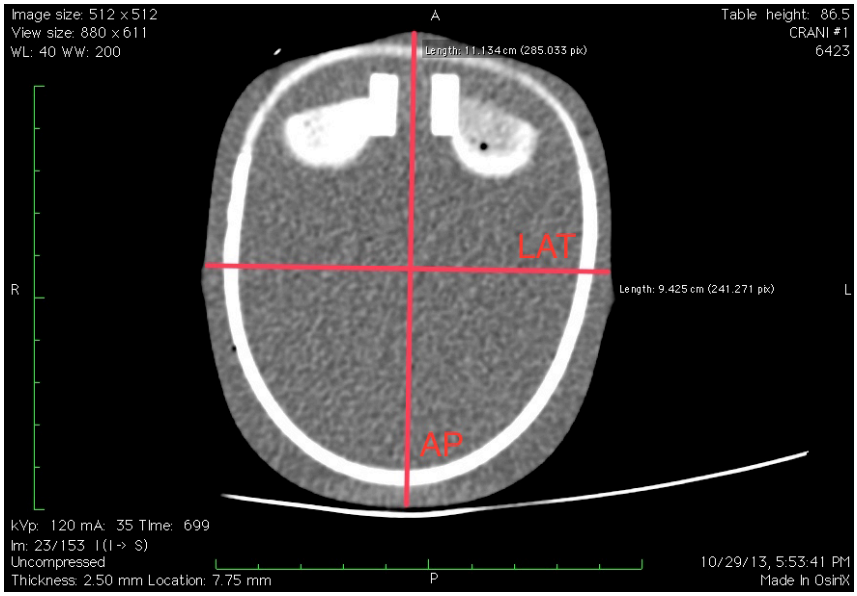

Figure 2.9: AP and LAT measurements of the newborn phantom's head

The effective diameter was plotted against the respective age-specific $CTDI_{vol}$-to-lens dose CF (CF_{age}), and exponential regression equations were obtained in the form of equation 2.7:

$$CF_{size} = \alpha e^{\beta d_{Eff}} \tag{2.7}$$

In this equation, α and β are constants, and d_{Eff} is the effective head diameter (in cm).

To evaluate the feasibility of using the scanner-independent (SI) exponential fit parameters for estimating lens doses on both scanners, the fitted lens dose values had to be calculated using the SI fit function. The methodology to calculate the fitted lens dose values is described in Figure 2.10. First, the effective diameters for each phantom were used to calculate CF_{size} from the SI exponential fit function. For each protocol that a given phantom was scanned with, the $CTDI_{vol}$, which was extracted from the structured dose report, was multiplied by the CF_{size} derived in the previous step for that particular phantom.

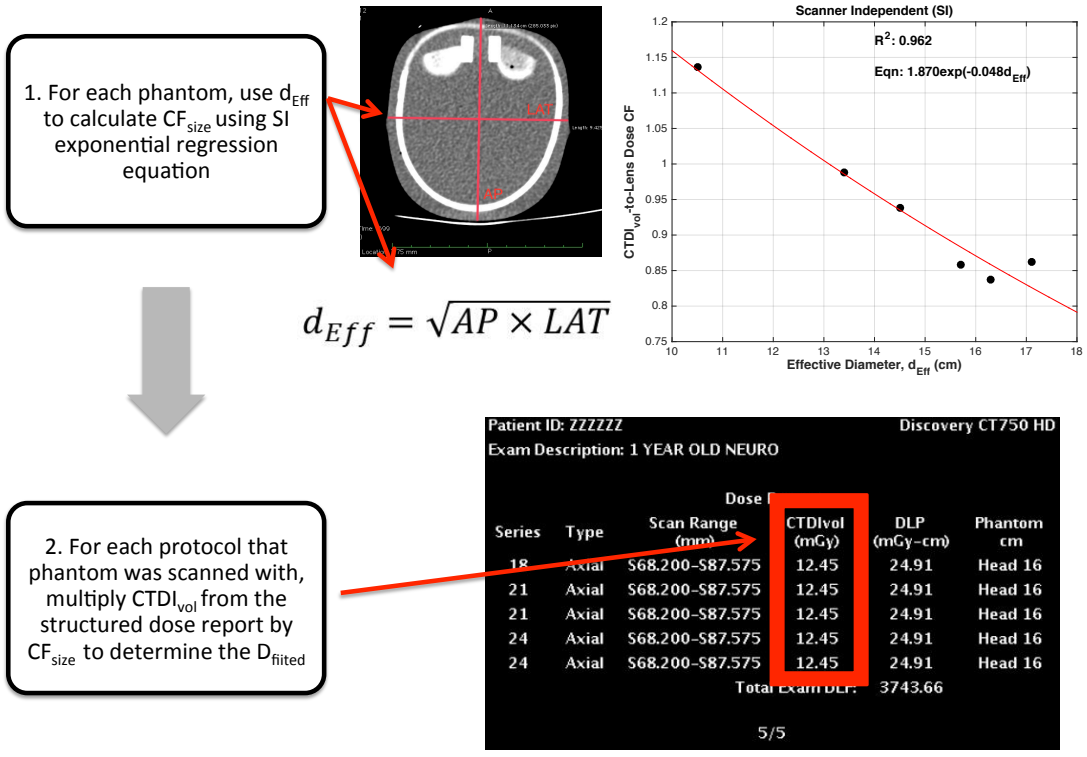

Figure 2.10: Methods used to calculate the fitted lens dose values for each phantom and protocol combination. This method uses the SI exponential regression equation and the effective diameter (d_{Eff}) to determine the size-specific $CTDI_{vol}$-to-lens dose CF (CF_{size}).

The difference between the measured and fitted values were calculated using equation 2.8:

$$Difference = 100 \times \left(\frac{\left| D_{measured} - D_{fitted} \right|}{D_{measured}} \right) \tag{2.8}$$

In this equation, $D_{measured}$ is a given protocol- and phantom-specific lens dose measured in this study, and D_{fitted} is the fitted value for the $CTDI_{vol}$ value corresponding to the scan where that protocol- and phantom-specific lens dose was measured.

2.3 Results

2.3.1 Protocol-specific Lens Dose

The protocol- and phantom-specific radiation dose to the lens from protocols on the Discovery 750 HD and SOMATOM Definition Flash scanners are displayed in Figures 2.11 and 2.12. For the Discovery 750 HD scanner, the lens dose (in mGy) ranged from 5.0 to 23.5 in the newborn, 4.7 to 13.1 in the 1-year-old, 4.2 to 19.6 in the 5-year-old, 16.6 to 31.6 in the 10-year-old, 16.5 to 30.5 in the adult female, and 18.2 to 31.7 in the adult male. For the SOMATOM Definition Flash scanner, the lens dose (in mGy) ranged from 8.0 to 16.2 in the newborn, 6.1 to 15.7 in the 1-year-old, 6.2 to 14.3 in the 5-year-old, 12.5 to 36.2 in the 10-year-old, 11.7 to 27.8 in the adult female, and 13.8 to 30.6 in the adult male. Tabular data of lens doses for each phantom and protocol measured on the Discovery 750 HD and SOMATOM Definition Flash scanners is listed in Appendix A. For each phantom, the lens dose varied by protocol, which reflects the variations in the

technical parameters among head imaging protocols (Tables 2.4 and 2.5). Technical parameters are selected for a given protocol based upon the anatomy to be imaged. Since the imaging protocols investigated in this study target different structures of the head, the technical parameters, and therefore dose, will vary for each. Additionally, the results show that the measured lens dose varies depending on phantom age. At our institution, different technical factors are utilized depending on the age of the patient who is receiving the CT scan; currently, head imaging protocols are separated into four different age groups including 0 to 3 years, 4 to 7 years, 8 to 12 years, and 12 years to adult. This is because less radiation is required to produce a given amount of image quality when scanning smaller patients compared to larger patients.

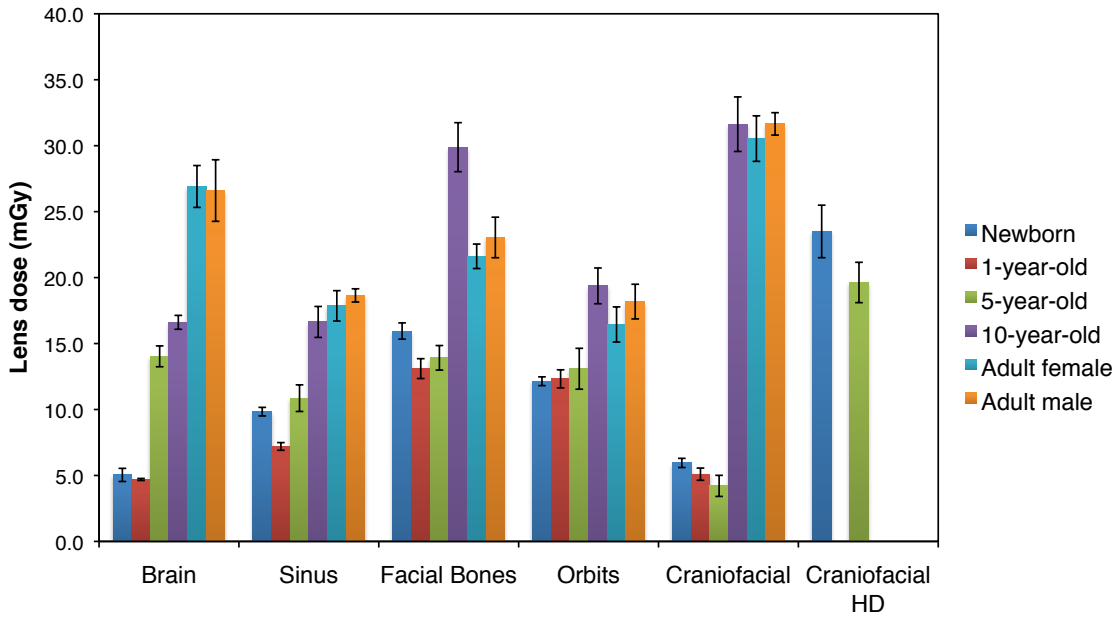

Figure 2.11: Protocol- and phantom-specific lens dose measured on the Discovery 750 HD scanner

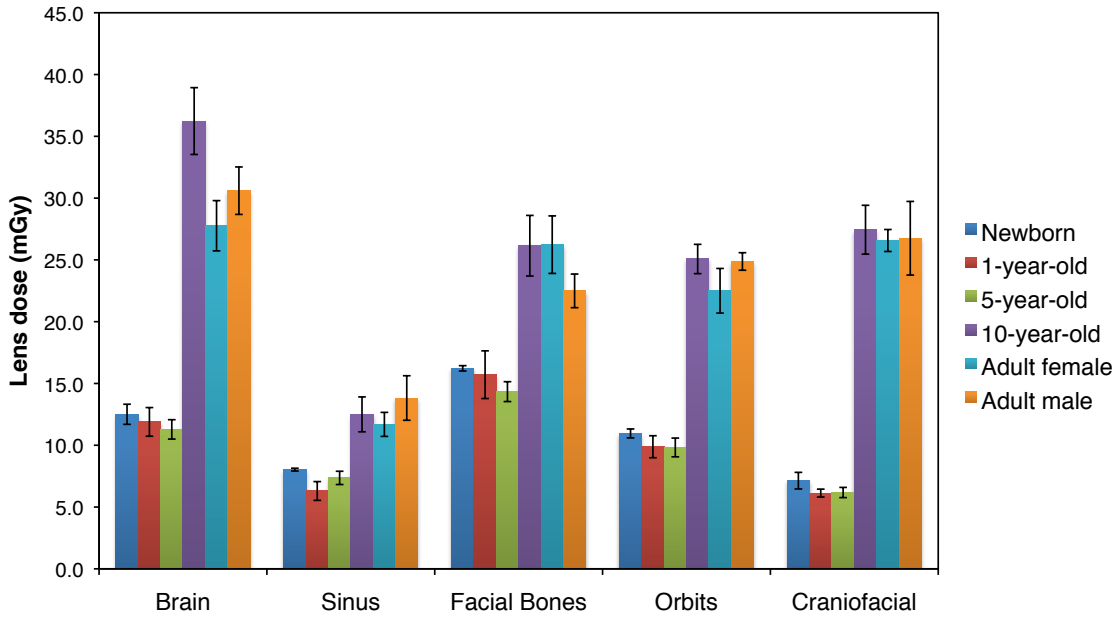

Figure 2.12: Protocol- and phantom-specific lens dose measured on the SOMATOM Definition Flash scanner

Between the two scanners, there are some differences in the measured lens doses likely due to variations in the technical parameters used for a given protocol on a particular CT scanner model. However, it should be noted that the goal of this study was not to make conclusions on which scanner had protocols with the lowest dose. To evaluate scanner performance, both radiation dose and image quality measurements should be made, but this is beyond the scope of this study.

2.3.2 Age-Specific $CTDI_{vol}$-to-Lens Dose CFs

For each phantom, the $CTDI_{vol}$-to-lens dose CFs are listed in Table 2.7. This table provides the CFs for the dose measurements from Discovery 750 HD scanner and the SOMATOM Definition Flash scanner. It also provides the scanner-independent (SI)

$CTDI_{vol}$-to-lens dose CFs, which were derived using the combined data from the two scanners. The $CTDI_{vol}$-to-lens dose CFs ranged from 0.86 to 1.18 on the Discovery 750 HD and 0.82 to 1.07 on the SOMATOM Definition Flash scanner. The SI method yielded CFs ranging from 0.84 to 1.14. In all three sets, the lower values correspond to phantoms with larger head sizes (i.e. adult) and the higher values correspond to phantoms with smaller head sizes (i.e. newborn). The dependence of the $CTDI_{vol}$-to-lens dose CFs on head size can be explained by considering the definition of $CTDI_{vol}$. For the case of a head imaging protocol, $CTDI_{vol}$ is the average dose to the center slice of a cylindrical phantom with a 16 cm diameter. Since this study is comparing doses measured in anthropomorphic phantoms with varying diameters to the dose measured in a 16-cm phantom, the $CTDI_{vol}$-to-lens dose CFs will differ based upon the size of the anthropomorphic phantom's head. For phantoms with smaller head sizes, the CF will be higher because smaller diameters result in less attenuation of the radiation beam through the head, yielding an increase in lens dose. As the phantom's head size increases, the CF will decrease because there is more attenuation of the radiation beam through the head, resulting in decreased lens dose.

Table 2.7: Age-specific $CTDI_{vol}$-to-lens dose conversion factor (CF_{age}) and coefficient of determination (R^2) calculated for each phantom

Phantom	Discovery 750 HD		SOMATOM Definition Flash		SI	
	CF_{age}	R^2	CF_{age}	R^2	CF_{age}	R^2
Newborn	1.18	0.96	1.07	0.99	1.14	0.94
1-year-old	1.01	0.99	0.97	0.96	0.99	0.97
5-year-old	0.93	0.95	0.95	0.99	0.94	0.97
10-year-old	0.88	0.94	0.85	0.98	0.86	0.95
Adult female	0.86	0.96	0.82	0.94	0.84	0.94
Adult male	0.88	0.90	0.84	0.90	0.86	0.89

2.3.3 Size-Specific $CTDI_{vol}$-to-Lens Dose Estimation Method

The effective diameter, d_{Eff}, measured for each phantom is listed in Table 2.8. These values were plotted against the respective $CTDI_{vol}$-to-lens dose CF and fitted to an exponential function in the form of equation 2.7.

Table 2.8: Measured AP and LAT head diameters and calculated values of effective diameter for each phantom

Phantom	AP diameter (cm)	LAT diameter (cm)	Effective diameter, d_{Eff} (cm)
Newborn	11.1	9.8	10.5
1-year-old	14.8	12.2	13.4
5-year-old	15.9	13.3	14.5
10-year-old	17.1	14.4	15.7
Adult female	19.3	13.8	16.3
Adult male	20.5	14.4	17.1

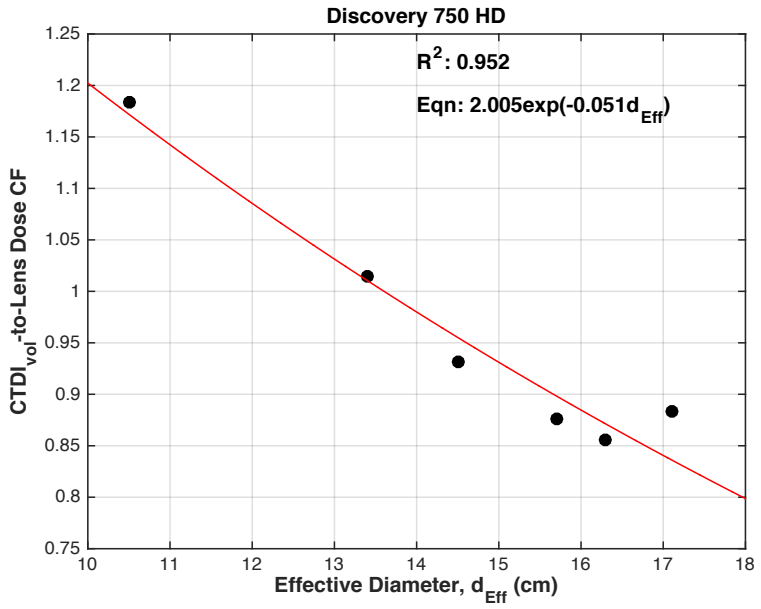
Discovery 750 HD
R2: 0.952
Eqn: 2.005exp(-0.051dEff)
CTDIvol-to-Lens Dose CF
Effective Diameter, dEff (cm)
1.25
1.2
1.15
1.1
1.05
1
0.95
0.9
0.85
0.8
0.75
10
11
12
13
14
15
16
17
18

a)

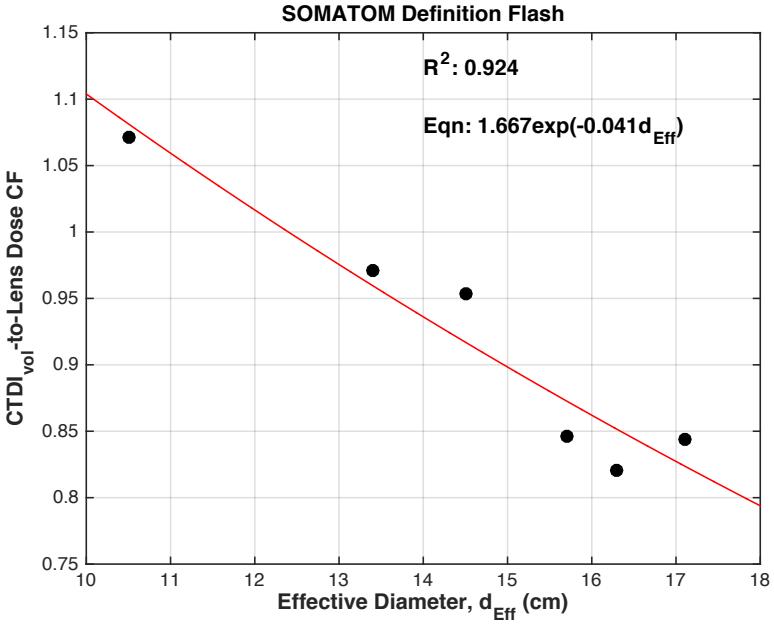
SOMATOM Definition Flash
R2: 0.924
Eqn: 1.667exp(-0.041dEff)
CTDIvol-to-Lens Dose CF
Effective Diameter, dEff (cm)
1.15
1.1
1.05
1
0.95
0.9
0.85
0.8
0.75
10
11
12
13
14
15
16
17
18

b)

c)

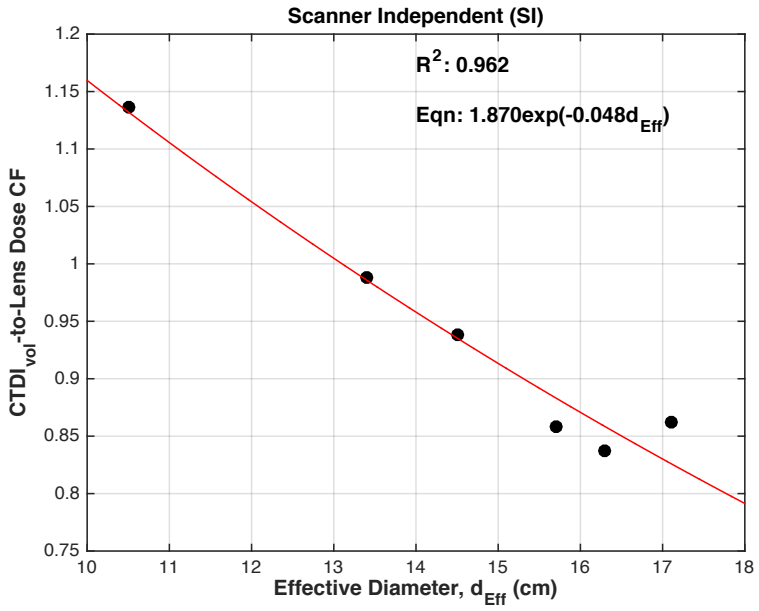

Figure 2.13: Relationship between the $CTDI_{vol}$-to-lens dose CF and effective diameter for the data collected on the a) Discovery 750 HD scanner and b) SOMATOM Definition Flash scanner. Graph c displays the relationship between the $CTDI_{vol}$-to-lens dose CF and effective diameter for the scanner-independent case.

The relationship between the $CTDI_{vol}$-to-lens dose CF and d_{Eff} for the Discovery 750 HD data set, the SOMATOM Definition Flash data set, and the SI data set are displayed in Figures 2.13a, b, and c, respectively. Additionally, a compiled list of the fit parameters for each of the three data sets is given in Table 2.9. The R^2 values for the Discovery 750 HD data set, the SOMATOM Definition Flash data set, and SI data set were 0.95, 0.92, and 0.96, respectively, indicating this is likely a good model for the relationship between the $CTDI_{vol}$-to-lens dose CF and d_{Eff}.

Table 2.9: Exponential fit parameters, α and β, and the coefficient of determination (R^2) for the data from the Discovery 750 HD scanner, SOMATOM Definition Flash scanner, and SI case. These parameters can be used to calculate the size-specific $CTDI_{vol}$-to-lens dose CF from the effective head diameter.

	Exponential regression coefficients		Coefficient of determination
	α	β	R^2
Discovery 750 HD	2.005	-0.051	0.95
SOMATOM Definition Flash	1.667	-0.041	0.92
Scanner-independent (SI)	1.870	-0.048	0.96

Using the exponential fit parameters derived from the SI data set, fitted values were calculated using all of the $CTDI_{vol}$ values recorded from the experiment. The difference between the fitted and measured values at each $CTDI_{vol}$ is shown in Figure 2.15. In this figure, the dotted line marks a difference of 10% and the dashed line marks a difference of 15%. A histogram showing the number of values that fell within a given percentage range is displayed in Figure 2.16. Overall, 84% of the fitted values agreed within 10% of the measured values, and 97% of the fitted values agreed within 15% of the measured values. This suggests that the fit parameters derived from the SI data set can be used to estimate lens dose fairly accurately without knowledge of scanner model.

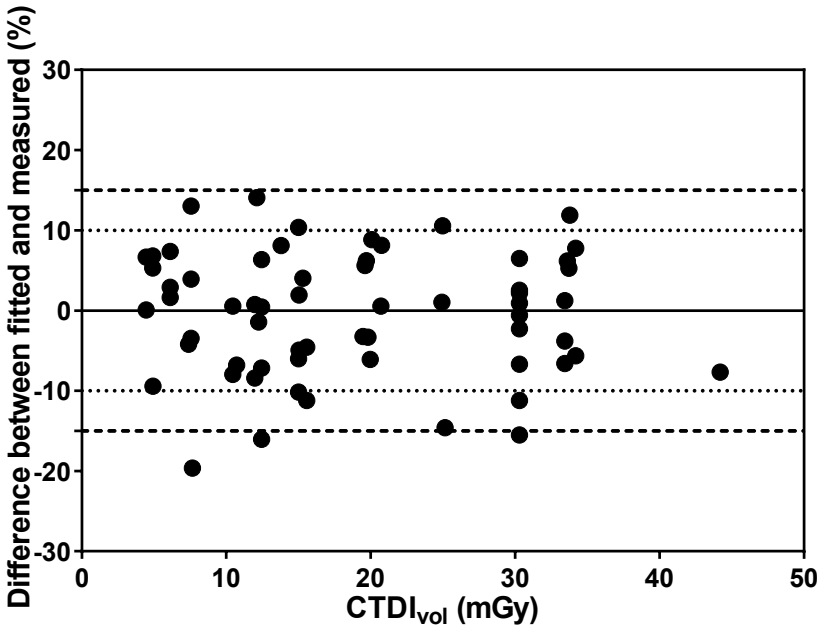

Figure 2.14: Plot of difference between the fitted and measured values in percentages. The fitted values were calculated using CF_{size} for each phantom and the $CTDI_{vol}$ recorded during dose measurements for each phantom and protocol

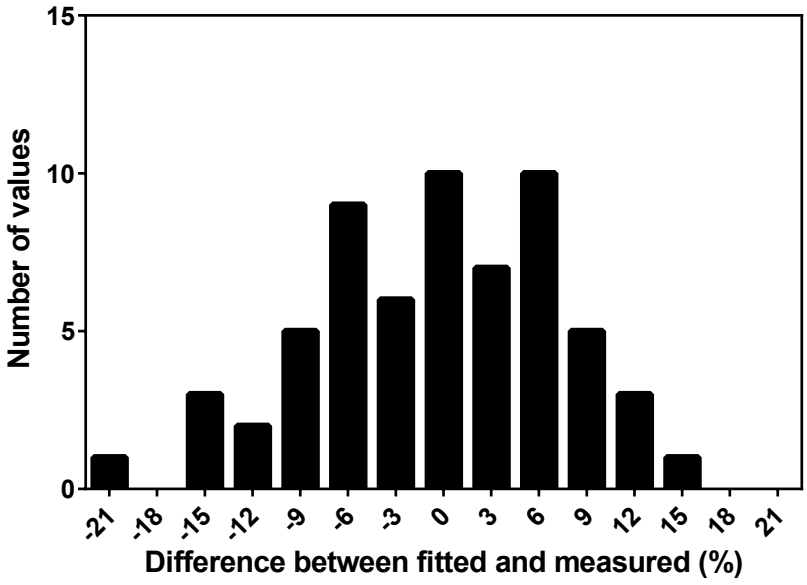

Figure 2.15: Histogram of the differences between the measured and fitted lens dose values

2.4 Conclusions

Since there has been a wide range of lens doses from head CT scans published in current literature (91-93, 95, 96), the purpose of this study was to measure the lens dose from the most current head CT protocols at our institution. The results of this study showed that lens dose from a single head CT examination ranged from 4.2 to 36.2 mGy depending on the protocol and the phantom age. These values are much lower than the recently suggested threshold dose of 500 mGy for cataract induction (56, 81). Additionally, these values were on the lower end of the 8.2 to 143.3 mGy range of lens doses reported in other recent studies (91-93).

Since head size can vary between children of the same age (111) and since recent studies have shown that there is an exponential relationship between $CTDI_{vol}$-to-organ dose CFs and patient size (102, 103, 105), the second purpose of this study was to determine the feasibility of a patient size-specific $CTDI_{vol}$-to-lens dose CF estimation method. The results of the exponential regression analysis demonstrated that there was an exponential relationship between the effective head diameter and $CTDI_{vol}$-to-lens dose CF, with R^2 values ranging from 0.92 to 0.96. Additionally, the majority of the fitted lens dose values, which were computed using the $CTDI_{vol}$-to-lens dose CF calculated with the SI exponential fit parameters, fell within 10-15% of the measured values from the phantom study, suggesting that this is a fairly accurate method of estimating lens dose from the $CTDI_{vol}$ with knowledge of the patient's head size.

One of this study's limitations is that it only considered radiation dose to the lens and resulting CT dose index-to-organ dose CFs for two different scanners. This technique must be investigated for scanners from various manufacturers. However, the results demonstrate that it is possible to estimate lens dose from $CTDI_{vol}$ using the derived scanner-independent fit parameters for these two scanner models.

A limitation of using point dosimeters to measure dose in superficial organs from helical scans is that the start position of the tube can influence the measured readout. While some of the protocols in this study were acquired helically, there were three runs performed for each protocol, and sometimes runs were repeated up to three times before the readout occurred. Therefore, the effect of the tube start position on the measured readout was likely averaged out over the multiple runs.

3. Effect of Organ-Based Tube Current Modulation on $CTDI_{vol}$-to-Lens Dose Estimation Methods

3.1 Introduction

In an effort to decrease dose to the lens while maintaining image quality in the brain, organ-based tube current modulation (OB-TCM) reduces the tube current over a certain angular extent anteriorly and then increases the tube current for the remainder of the rotation (Figure 3.1). Reducing the tube current anteriorly reduces the number of photons that impinge on the anterior surface of the head, thus reducing dose. Increasing the tube current posteriorly allows for image quality to be maintained while still reducing dose to the lens due to beam hardening.

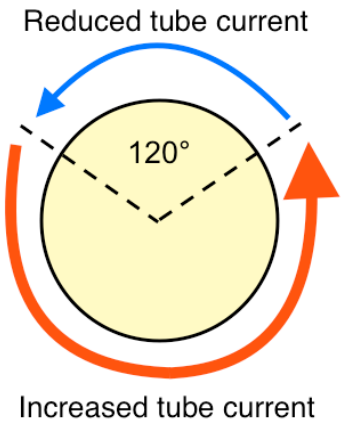

Figure 3.1: Schematic of the OB-TCM methodology

A recent study has shown that a commercially available OB-TCM software (X-CARE, *Siemens Healthcare*, Erlangen, Germany) reduces the tube current by 75% over the anterior 120 degrees of the tube rotation, and then increases it by 25% for the remaining portion of the rotation (112). Studies on OB-TCM in head CT have shown that the dose

to the lens of the eye can be reduced by 19 to 34% (112-116). However, these studies have not investigated the impact of OB-TCM on size-specific methods to estimate lens dose from $CTDI_{vol}$. Thus, the aim of this chapter is to measure the radiation dose to the lens of the eye in phantoms with different head sizes and to determine a method to estimate lens dose from $CTDI_{vol}$ for protocols with OB-TCM.

3.2 Materials and Methods

3.2.1 CT Scanner and Beam Data

The one scanner used for data collection was the SOMATOM Definition Flash CT scanner (*Siemens Healthcare*, Erlangen, Germany). Out of the two scanners used for dose measurements in Chapter 2, this scanner was the only model with OB-TCM software. Beam quality information for this scanner was previously measured and is listed in Table 2.2.

3.2.2 Anthropomorphic Phantoms and Head Imaging Protocols

The same six anthropomorphic phantoms described in Section 2.2.2 were used for dose measurements. Each phantom was scanned with five different head imaging protocols at 120 kV. These protocols were designed to be similar to the protocols listed in Table 2.5; the major difference between them is the implementation of the OB-TCM software. The protocol parameters for the SOMATOM Definition Flash scanner with OB-TCM are listed in Table 3.1. Examples of how the scan range varies among protocols are shown in Figures 2.4a-d.

Table 3.1: Parameters for protocols with OB-TCM on the SOMATOM Definition Flash scanner

Phantom	Protocol	Tube Current (mAs/rot)	FOV (cm)	Pitch	$CTDI_{vol}$ (mGy)	DLP (mGy-cm)
Newborn	Brain	46.0	6.0	0.60	11.6	157.0
	Sinus	28.0	10.0	0.60	7.2	54.7
	Facial Bones	58.0	12.0	0.60	14.7	154.5
	Orbits	41.0	10.0	0.60	10.2	68.3
	Craniofacial	23.0	18.0	0.60	5.6	87.0
1-year-old	Brain	46.0	20.0	0.60	11.8	150.7
	Sinus	29.0	15.0	0.60	7.4	64.0
	Facial Bones	59.0	15.0	0.60	15.1	204.0
	Orbits	42.0	15.0	0.60	10.5	98.0
	Craniofacial	23.0	20.0	0.60	5.9	99.0
5-year-old	Brain	46.0	20.0	0.60	11.8	156.3
	Sinus	28.0	15.0	0.60	7.4	72.8
	Facial Bones	59.0	15.0	0.60	15.1	219.1
	Orbits	41.0	15.0	0.60	10.5	97.7
	Craniofacial	22.0	20.0	0.60	5.9	115.7
10-year-old	Brain	154.0	22.0	0.55	43.9	638.0
	Sinus	54.0	16.0	0.55	15.1	152.0
	Facial Bones	108.0	16.0	0.55	29.7	435.0
	Orbits	108.0	16.0	0.55	29.8	269.3
	Craniofacial	108.0	24.0	0.55	30.0	616.0
Adult female	Brain	121.0	22.0	0.55	34.3	529.0
	Sinus	54.0	16.0	0.55	14.9	206.0
	Facial Bones	107.0	16.0	0.55	29.6	529.7
	Orbits	108.0	15.0	0.55	29.4	294.3
	Craniofacial	108.0	24.0	0.55	30.1	780.3
Adult male	Brain	122.0	22.0	0.55	34.3	529.3
	Sinus	54.0	16.0	0.55	14.7	203.7
	Facial Bones	108.0	16.0	0.55	30.0	613.3
	Orbits	108.0	15.0	0.55	29.7	298.0
	Craniofacial	108.0	24.0	0.55	30.0	778.0

3.2.3 MOSFET Calibration

The MOSFET calibration procedure was the previously described in Section 2.2.3.

3.2.4 Dose Measurements

The dose measurement procedure was previously described in Section 2.2.4.

3.2.5 Magnitude of Dose Reduction with Organ-Based Tube Current Modulation

The head imaging protocols from this chapter were designed to be nearly identical to the protocols for the SOMATOM Definition Flash scanner from Chapter 2 (listed in Table 2.5). The major difference is the use of the OB-TCM software for the protocols in this chapter. Therefore, the amount of dose reduction to the lens was calculated for each protocol using equation 3.1:

$$D_{savings}(\%) = 100 \times \left(1 - \frac{D_{OB-TCM}}{D}\right) \tag{3.1}$$

In this equation, $D_{savings}$ is the dose reduction percentage, $D_{OB\text{-}TCM}$ is the corresponding protocol- and phantom-specific lens dose measured while using the OB-TCM software, and D is the corresponding protocol- and phantom-specific lens dose measured on the SOMATOM Definition Flash scanner in Chapter 2.

The standard deviation of the dose savings, $\sigma_{savings}$ was calculated through propagation of error with equation 3.2:

$$\sigma_{savings}(\%) = 100 \times \left(\frac{D_{OB-TCM}}{D}\right) \times \sqrt{\left(\frac{\sigma_{OB-TCM}}{D_{OB-TCM}}\right)^2 + \left(\frac{\sigma_D}{D}\right)^2} \tag{3.2}$$

In this equation, $\sigma_{OB\text{-}TCM}$ is the standard deviation of the protocol- and phantom-specific lens dose measured for protocols with OB-TCM and σ_D is the standard deviation of the corresponding protocol- and phantom-specific lens dose measured on the SOMATOM Definition Flash scanner in Chapter 2.

3.2.6 Definition of Age-Specific $CTDI_{vol}$-to-Lens Dose CF

Methods to derive the age-specific $CTDI_{vol}$-to-lens dose CFs for each phantom were previously described in Section 2.3.2.

3.2.7 Definition of Size-Specific $CTDI_{vol}$-to-Lens Dose CF

The relationship between the $CTDI_{vol}$-to-lens dose CF and head size for protocols with OB-TCM was investigated using the phantom data from this study. Methods for calculating the effective head diameter, d_{Eff}, were previously described in Section 2.2.6, and the methods to derive the exponential regression equation were the same as that described in Section 2.3.3.

To evaluate the feasibility of using the derived exponential fit parameters for estimating lens doses from protocols with OB-TCM, the difference between the measured and fitted values was calculated using equation 2.8.

3.3 Results

3.3.1 Protocol-Specific Lens Dose

The protocol- and phantom-specific radiation dose to the lens from protocols utilizing OB-TCM software on the SOMATOM Definition Flash scanner is displayed in

Figure 3.2. The lens dose (in mGy) ranged from 6.4 to 13.4 in the newborn, 5.4 to 11.1 in the 1-year-old, 5.5 to 10.8 in the 5-year-old, 10.8 to 25.3 in the 10-year-old, 11.3 to 20.3 in the adult female, and 10.4 to 22.3 in the adult male. Tabular data of lens doses for each phantom and protocol is listed in Appendix A. For each phantom, the lens dose varied by protocol, which reflects the variations in the exposure parameters among head imaging protocols (Table 3.1). Exposure parameters are selected for a given protocol based upon the anatomy to be imaged. Since the imaging protocols investigated in this study target different structures of the head, the exposure parameters, and therefore dose, will vary for each. Additionally, the results show that the measured lens dose varies depending on phantom age. At our institution, different technical factors are utilized depending on the age of the patient who is receiving the CT scan; this topic was already discussed in Section 2.3.1.

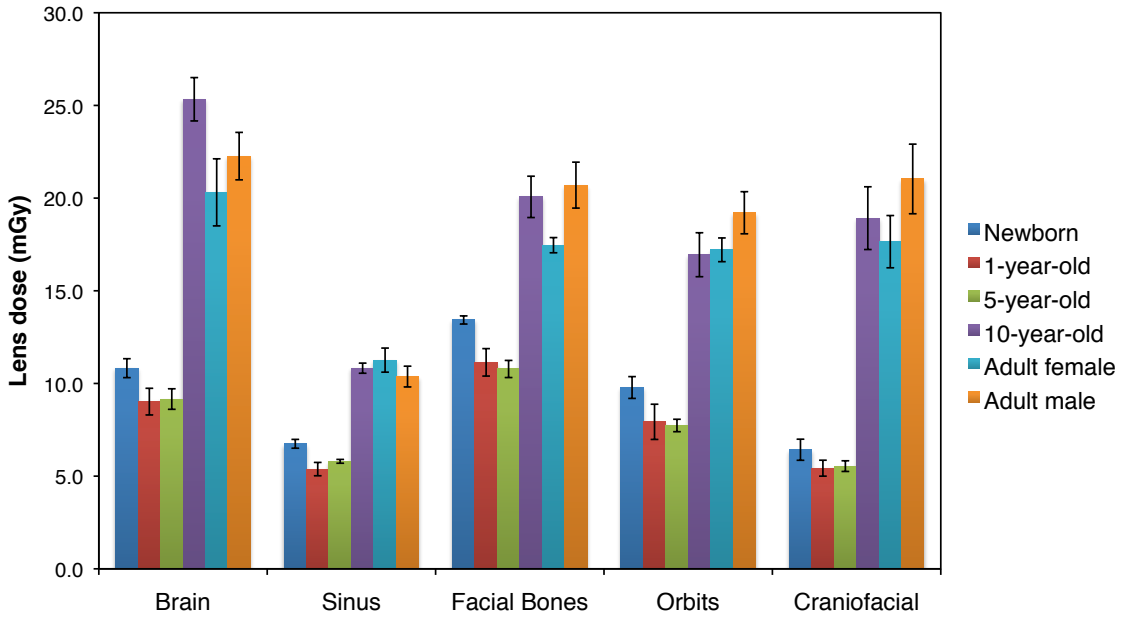

Figure 3.2: Protocol- and phantom-specific lens dose measured for head CT protocols with OB-TCM

3.3.2 Dose Savings for Head CT Imaging Protocols with OB-TCM

The protocol- and phantom-specific dose savings to the lens from protocols utilizing OB-TCM software on the SOMATOM Definition Flash scanner is displayed in Figure 3.3. Compared to the protocols without OB-TCM (from Chapter 2), the reduction in lens dose ranged from 9.9 to 17.3% in the newborn, 11.4 to 29.1% in the 1-year-old, 10.3 to 24.8% in the 5-year-old, 13.4 to 32.4% in the 10-year-old, 3.6 to 33.6% in the adult female, and 8.0 to 27.2% in the adult male. These results are consistent with the results of similar studies, which found the range of lens dose reduction to range from 19 to 34% (112-116).

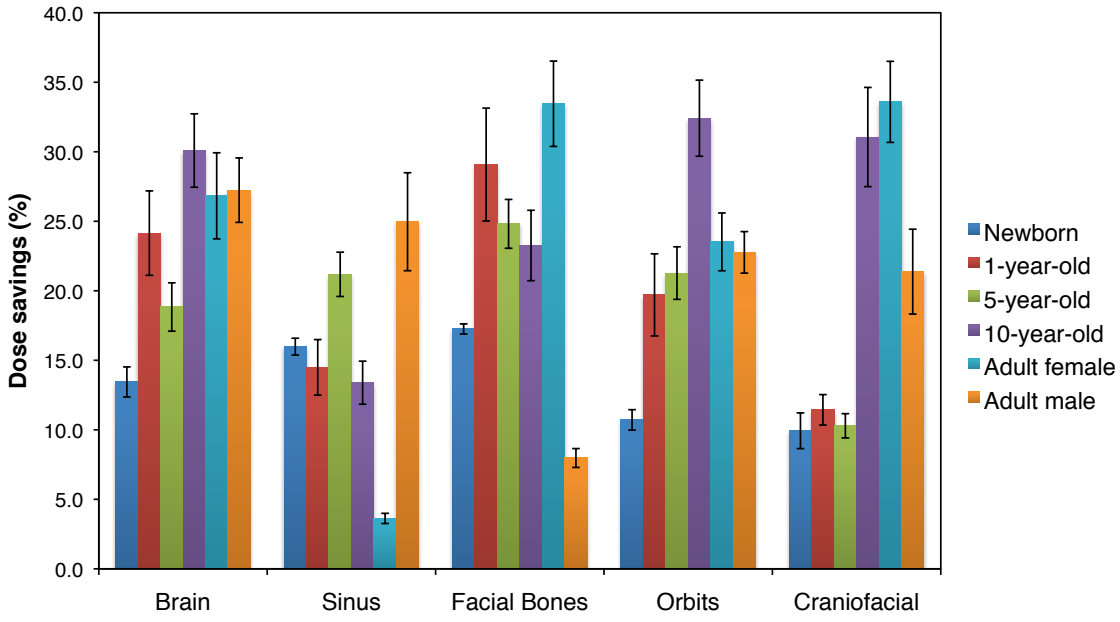

Figure 3.3: Reduction in lens dose for head CT protocols with OB-TCM

Generally, the dose reduction potential was greater in the phantoms with larger head sizes. In protocols with OB-TCM, the lens dose reduction is in part due to the decrease in tube current (and therefore decrease in the number of photons) anteriorly. To maintain image quality within the head, the tube current is increased posteriorly, which allows for an appropriate amount of photons to pass through the patient and reach the detector. Increasing the tube current posteriorly also takes advantage of beam hardening, where less lower energy photons, which contribute to dose but not image quality, make it to the lens on the anterior surface because they are attenuated more readily close to the posterior surface. In adult patients, more photons are attenuated by the time they reach the lens of the eye compared to pediatric patients because of the difference in axial head thickness. Therefore, it is understandable that the lens dose

reduction is greater in the phantoms with the larger head diameters (i.e. adult phantoms) compared to the ones with smaller head diameters (i.e. pediatric phantoms).

3.3.3 Age-Specific $CTDI_{vol}$-to-Lens Dose CF

For each phantom, the $CTDI_{vol}$-to-lens dose CFs for protocols utilizing OB-TCM software on the SOMATOM Definition Flash scanner are listed in Table 3.2. The $CTDI_{vol}$-to-lens dose CFs ranged from 0.60 to 0.93, with the lower values corresponding to the phantoms with larger head sizes (i.e. adult) and the higher values corresponding to the phantoms with smaller head sizes (i.e. newborn). The dependence of the $CTDI_{vol}$-to-lens dose CFs on head size was discussed in Section 2.3.2 for protocols that do not utilize any dose reduction methods; similar trends were observed for protocols that utilize the OB-TCM dose reduction method. For phantoms with smaller head sizes, the CF will be higher than those with larger head sizes because smaller axial patient thicknesses result in less attenuation of the radiation beam before reaching the lens of the eye. As the phantom's head size increases, the CF will decrease because the larger head size attenuates more of the radiation beam before reaching the lens, which results in decreased lens dose. Unlike the CFs derived in Chapter 2, the maximum value does not exceed a value of 1.0. For the case of a head imaging protocol that utilizes OB-TCM, $CTDI_{vol}$ is still the weighted average dose from central and peripheral measurements to the center slice of a cylindrical phantom with a 16 cm diameter. Therefore, the high mA region posteriorly will essentially cancel out the effect of the low mA region anteriorly

on peripheral $CTDI_{vol}$ measurements. It is understandable that the CF_{age} will be less than 1 because the lens dose is measured in the low mA region, and the effect of the low mA region on peripheral $CTDI_{vol}$ measurements is cancelled out by the increased mA posteriorly.

Table 3.2: Age- specific $CTDI_{vol}$-to-lens dose conversion factors (CF_{age}) and the coefficient of determination (R^2) for the head CT protocols with OB-TCM

Phantom	OB-TCM	
	CF_{age}	R^2
Newborn	0.93	0.95
1-year-old	0.76	0.95
5-year-old	0.75	0.91
10-year-old	0.61	0.91
Adult female	0.60	0.87
Adult male	0.67	0.97

3.3.4 Size-Specific $CTDI_{vol}$-to-Lens Dose Conversion Factors

The effective diameter, d_{Eff}, was previously measured for each phantom in Chapter 2 and the values are listed in Table 2.8. The d_{Eff} values for each phantom were plotted against the respective age-specific $CTDI_{vol}$-to-lens dose CF and fitted to an exponential function in the form of equation 2.7. The relationship between the $CTDI_{vol}$-to-lens dose CF and d_{Eff} for the OB-TCM protocols on the SOMATOM Definition Flash

scanner is displayed in Figure 3.4. Additionally, a compiled list of the fit parameters for this data set is given in Table 3.3. The R^2 value for the OB-TCM data set was 0.87.

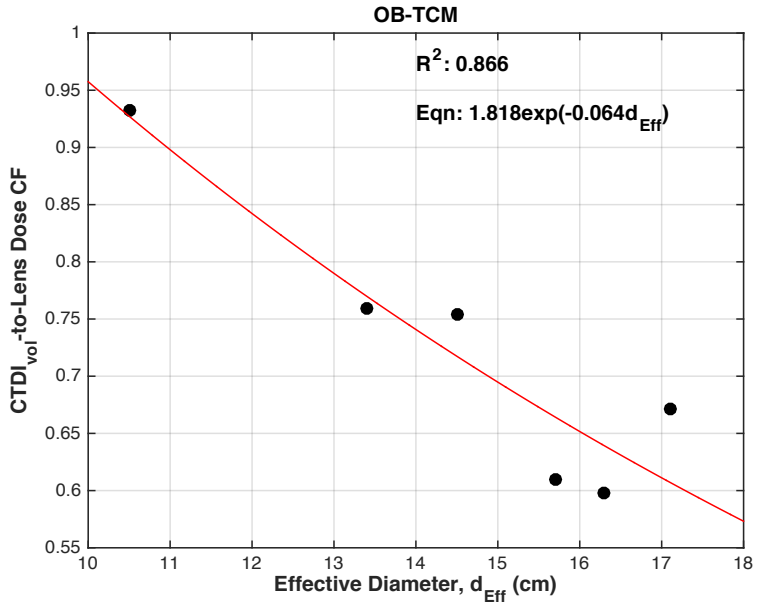

Figure 3.4: Relationship between the $CTDI_{vol}$-to-lens dose CF for head CT protocols with OB-TCM

Table 3.3: Exponential fit parameters for head CT protocols with OB-TCM. These parameters can be used to calculate the size-specific $CTDI_{vol}$-to-lens dose CF (CF_{size}) from the effective head diameter.

	Exponential regression coefficients		Coefficient of determination
	α	β	R^2
OB-TCM	1.818	-0.064	0.87

Using the exponential fit parameters derived from the OB-TCM data set, fitted values were calculated using all of the $CTDI_{vol}$ values recorded from the experiment. The

difference between the fitted and measured values at each $CTDI_{vol}$ corresponding to the measured value is shown in Figure 3.5. In this figure, the dotted line marks a difference of 10% and the dashed line marks a difference of 15%. A histogram showing the number of values that fell within a given percentage range is displayed in Figure 3.6. Overall, 70% of the fitted values agreed within 10% of the measured values, 87% agreed within 15% of the measured values, and 93% agreed within 18% of the measured values. This suggests that the fit parameters derived from the OB-TCM data set and knowledge of the head size can be used to estimate lens dose with moderate accuracy for protocols that utilize OB-TCM software.

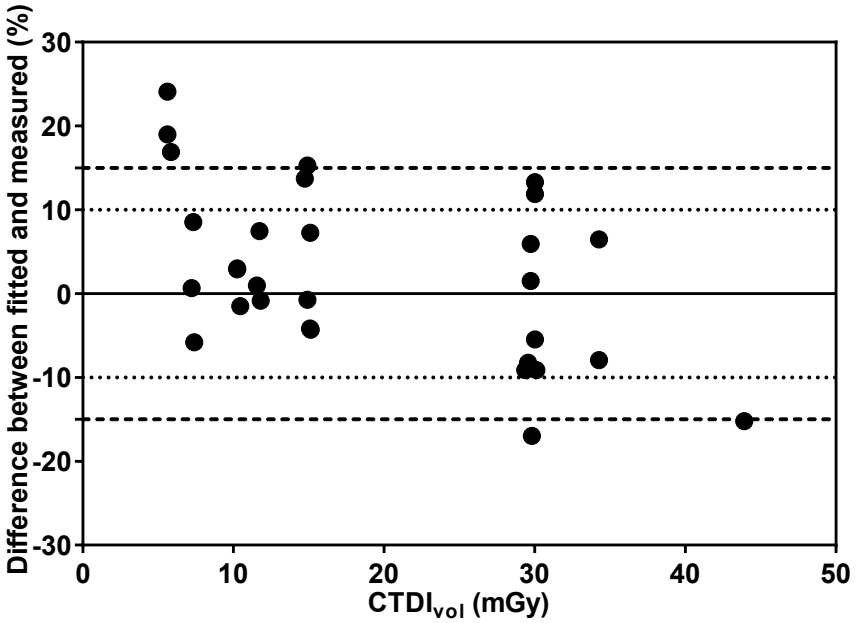

Figure 3.5: Plot of difference between the fitted and measured values in percentages. The fitted values were calculated using CF_{size} for each phantom and the $CTDI_{vol}$ recorded during dose measurements for each phantom and protocol

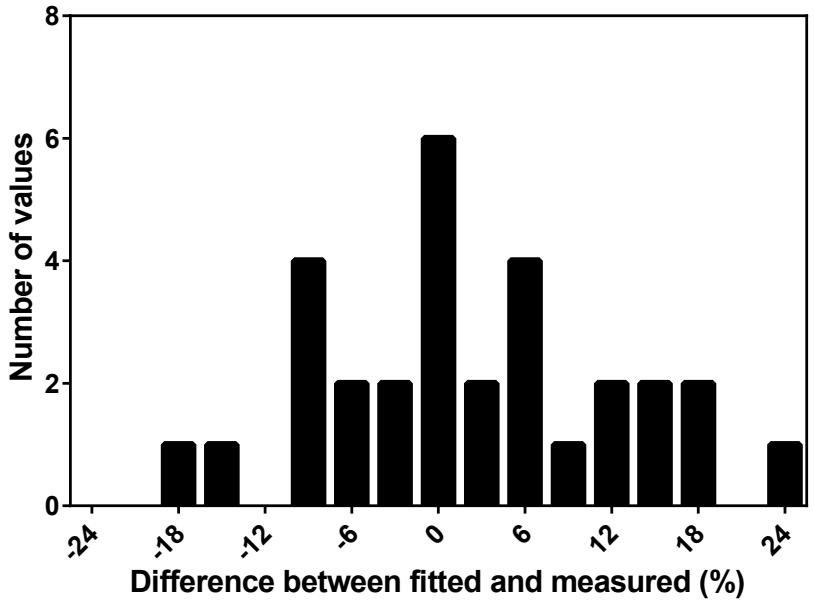

Figure 3.6: Histogram of the differences between the measured and fitted lens dose values

3.4 Conclusions

The amount of dose reduction to the lens of the eye when OB-TCM software is utilized in head CT protocols has been shown to range from 18 to 34% (112-116). However, the effect of patient head size on the dose reduction potential has not been investigated. Therefore, the purpose of this study was to measure the lens dose in phantoms ranging in age from newborn to adult when scanned with head CT protocols with OB-TCM. The lens doses measured in this study ranged from 5.4 to 25.3 mGy depending on the protocol and the phantom age. Compared to the protocols without OB-TCM reported in Chapter 2, the average lens dose reduction with OB-TCM was 13.5% for the newborn, 19.8% for the 1-year-old, 19.3% for the 5-year-old, 26.0% for the

10-year-old, 24.2% for the adult female, and 20.9% for the adult male. The dose reduction potential was lower for phantoms with smaller heads, likely due to reduced attenuation by underlying tissues compared to larger head sizes.

As in Chapter 2, the second goal of this study was to determine feasibility of a patient size-specific $CTDI_{vol}$-to-lens dose CF estimation method when OB-TCM is implemented in head CT protocols. The results of the exponential regression analysis demonstrated that there was a reasonable exponential relationship between the effective head diameter and $CTDI_{vol}$-to-lens dose CF, with a R^2 value of 0.87 for the fitted function.

When considering the error associated with the size-based method, the majority of the fitted lens dose values, which were computed using the $CTDI_{vol}$-to-lens dose CF calculated with the OB-TCM exponential fit parameters, fell within 15-18% of the measured values from the phantom study. The higher error compared to that of the fitting functions derived in Chapter 2 may be due to issues not explored in this study, such as the effect of patient positioning on the measured lens dose when OB-TCM is implemented. The OB-TCM software used in this study has been shown to reduce the tube current by 75% over the anterior 120 degrees of the tube rotation, and then increase it by 25% for the remaining portion of the rotation on the same scanner model used in this study's dose measurements (112). Rotation or off-centered positioning of the patients head can therefore affect whether the lens is located in the area of decreased tube current or increased tube current; this would have a great influence on the resulting

lens dose. One study found that lens dose can be increased by up to 18% when patients are shifted vertically downward from the isocenter in scans with OB-TCM (116). Another study found that lowering the phantom below isocenter led to reduced dose savings, but no trend based on distance from isocenter could be discerned with their current data (114).

Despite the greater error associated with the OB-TCM exponential fitting function, it can still provide a decent estimate of lens dose when protocols employ this dose reduction method. Additionally, to put this in perspective, the main use of the method derived in this study was to reconstruct cumulative lens doses from historical patient data. So if a patient receives one exam on a scanner equipped with OB-TCM and they were off-centered in the gantry, that one exam is only a single contribution to the entire cumulative lens dose, which is comprised of doses from several exams on different scanner models. The likelihood of a given patient having multiple exams where they were off-centered when scanned with an OB-TCM protocol is small. Therefore, the added error in the cumulative lens dose from that one exam is also likely to be trivial.

4. Effect of Gantry Angulation on $CTDI_{vol}$-to-Lens Dose Estimation Methods

4.1 Introduction

In CT imaging of the brain, the positioning of the head or the angle of the gantry influences whether the lens is irradiated directly by the primary beam or indirectly by scattered radiation. The lens is irradiated directly when the orbitomeatal line is used as the baseline (117). However, the lens can be avoided by angling the gantry such that the beam is parallel to the supraorbital plane (117); a schematic of the theory behind gantry angulation in brain CT is shown in Figure 4.1. Gantry angulation has been shown to decrease the radiation dose to the lens by 7.6 to 87.0% (115, 117, 118).

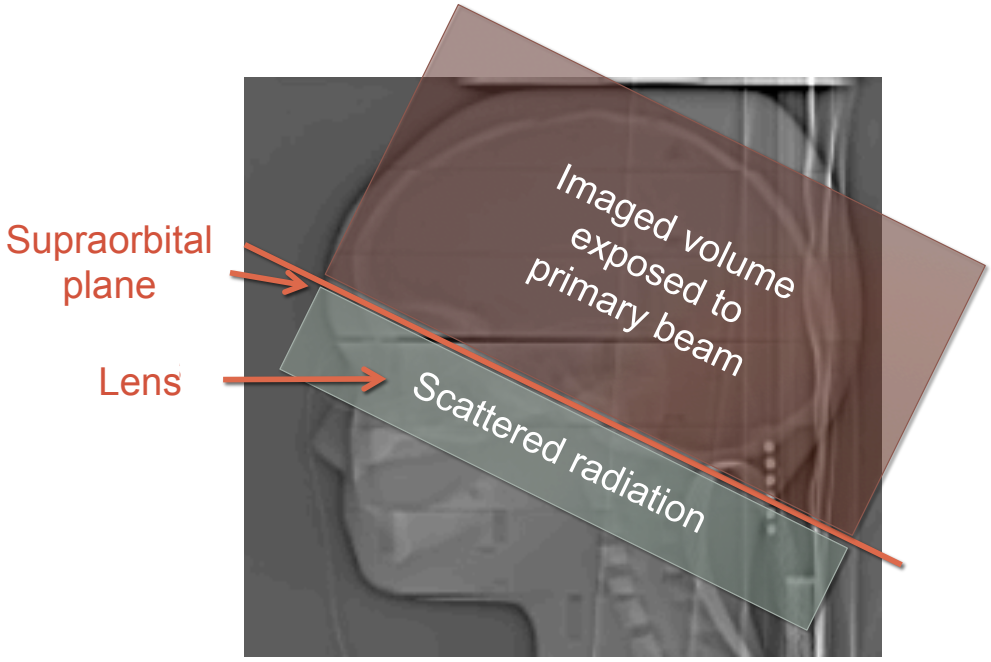

Figure 4.1: Schematic of the theory behind gantry angulation in brain CT. The gantry is angled such that it is parallel to the supraorbital plane, which allows the entire brain volume to be imaged while avoiding the lens.

If the orbits are avoided when gantry angulation is implemented, the lens would primarily be exposed to scattered radiation. The amount of dose to the lens would then depend upon how far away the lens is from the imaged volume. There has only been one study to investigate lens dose as a function of distance from the primary beam scan range to the lens of the eye in CT imaging of the head with gantry angulation (119). This was performed using Monte Carlo (MC) simulations and mathematical phantoms ranging in age from newborn to 15-years-old; the results of this study showed that the lens dose decreases as distance from the primary beam scan range increases (119). However, this study did not provide distance-specific $CTDI_{vol}$-to-lens dose conversion factors. Thus, the aim of this chapter is to investigate the effect of distance from the scan range on lens dose in CT imaging of the brain with gantry angulation.

4.2 Materials and Methods

4.2.1 CT Scanner and Beam Data

The one scanner used for data collection was the Discovery 750 HD scanner (GE Healthcare, Waukesha, WI). Out of the two scanners used for dose measurements in Chapter 2, this scanner was the only model capable of gantry angulation. Beam quality information for this scanner was previously measured and is listed in Table 2.2.

4.2.2 Anthropomorphic Phantoms, Radiochromic Film and TLD Placement, and Head Imaging Protocols

The same six phantoms described in Section 2.2.2 were used for the measurements explained in this chapter.

For dose measurement in all six phantoms, two TLD chips (TLD-100, *Thermo Fisher Scientific*, Franklin, MA) were placed in each predrilled location for the lens of the eye (Figure 2.4). TLDs were chosen for this experiment because they are more sensitive to radiation, with the lower limit of their useful range being 10 μGy (120), compared to MOSFETs, which have a lower limit of 1 cGy (121).

Radiochromic film that has been validated for use in radiation dosimetry was used to assess where the dose contribution from the primary beam ends in relation to the orbit when gantry angulation is used in brain imaging protocols. One piece of radiochromic film (Gafchromic XR-QA2, *Ashland, Inc*., Covington, KY) was placed in between the slabs superior and inferior to the slab that contained predrilled locations for the lens in each phantom. The lateral scout image showing the placement of the radiochromic film and TLDs within the 10-year-old phantom is displayed in Figure 4.2; the lateral scout images showing the placement of the radiochromic film and TLDs within the rest of the anthropomorphic phantoms are displayed in Appendix B.

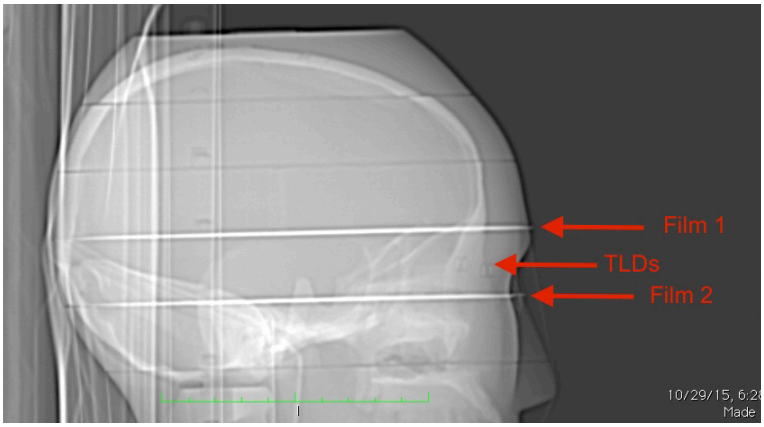

Figure 4.2: Placement of the radiochromic film and TLDs within the 10-year-old anthropomorphic phantom

Gafchromic XR-QA2 is a self-developing, refractive-type film that is sensitive to a dose range of 0.1 to 20 cGy and an energy range of 20 to 200 kVp (122). It consists of four layers including a 97 μm thick yellow polyester layer, a 20 μm thick pressure sensitive adhesive layer, a 25 μm thick active layer, and a 97 μm thick opaque white polyester layer (122). Exposure to ionizing radiation causes a solid-state polymerization reaction in the film, which results in changes to the optical density (OD) in the exposed areas (123, 124). Digitization of the film before and after irradiation allows for the calculation of the net optical density (netOD) using equation 4.1 (124, 125); calibration curves can be generated to convert netOD to absorbed dose.

$$netOD = OD_{post} - OD_{pre} = \log_{10}\left(\frac{I_0}{I_{post}}\right) - \log_{10}\left(\frac{I_0}{I_{pre}}\right) = \log_{10}\left(\frac{I_{pre}}{I_{post}}\right) \quad (4.1)$$

In this equation, OD_{post} is the optical density of the post-irradiation film, OD_{pre} is the optical density of the pre-irradiation film, I_0 is the intensity of the flat field scan, I_{post} is

the post-irradiation scanner light intensity values, and I_{pre} is the pre-irradiation scan light intensity values (124). Digitization was performed on an EPSON 10000XL scanner (*EPSON America*, Long Beach, CA) using the 48-bit color mode with a resolution of 72 dpi. This was performed prior to exposure to obtain I_{pre}. Post-irradiation digitization was performed 24-hours after exposure to allow for film polymerization (124). Every effort was made to ensure that the pre- and post-irradiation films were scanned in the same orientation and the same place on the scanner.

Each phantom was scanned with the brain imaging protocol at 120 kV. The gantry was angled such that the entire volume of the brain was imaged while trying to avoid scanning the lens of the eye with the primary beam. An example of the scan range when gantry angulation is implemented is shown in Figure 4.3. The parameters for the brain protocol with gantry angulation on the Discovery 750 HD scanner are listed in Table 4.1.

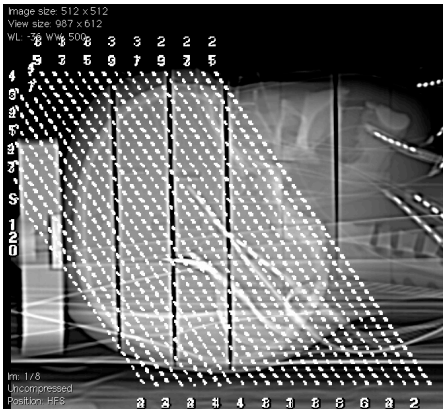

Figure 4.3: Example of a scan range on a lateral scout with gantry angulation for the brain imaging protocol on the Discovery 750 HD scanner. The angle of the dashed lines off of vertical indicates the angle of the gantry during image acquisition.

Table 4.1: Parameters for the brain imaging protocol with gantry angulation used during dose measurements

Phantom	Gantry angle (degrees)	Tube Current (mAs/rot)	FOV (cm)	Pitch	$CTDI_{vol}$ (mGy)	DLP (mGy-cm)
Newborn	18.0	52.5	18.0	Axial	9.7	101.9
1-year-old	12.5	52.5	20.0	Axial	9.1	112.1
5-year-old	20.0	77.5	22.0	Axial	13.0	193.0
10-year-old	22.0	100.0	22.0	Axial	18.5	279.5
Adult female	12.5	167.5	22.0	Axial	32.7	468.1
Adult male	8.5	167.5	22.0	Axial	33.1	468.1

4.2.3 Calibration of Radiochromic Film and TLDs

Calibration of the TLDs and radiochromic film was necessary in order to convert from the raw nanoColoumb and netOD readings by the respective dosimeters to absorbed dose in soft tissue. Prior to irradiation, the TLDs that were used for phantom measurements and calibration were annealed using a TLD-annealing furnace (168-300, *Radiation Products Design, Inc.*, Albertville, MN). Additionally, a piece of radiochromic film was cut into 5 small squares (approximately 2.5 cm x 2.5 cm) which were scanned prior to irradiation using the procedure described in Section 4.2.2; this provided the pre-calibration film images for the film analysis.

The calibration procedure involved simultaneously exposing two TLDs, one small piece of radiochromic film, and an ion chamber calibrated by an Accredited

Dosimetry Calibration Laboratory (ADCL) to an x-ray beam of the same quality as that used during dose measurements at 120 kV. The experimental set-up involved placing the TLDs and radiochromic film adjacent to the active volume of the ion chamber, which was positioned at the isocenter of the beam (Figure 4.4). The TLDs, radiochromic film, and ion chamber were positioned on a piece of 2.0 cm thick Plexiglas. A piece of radiochromic film was placed under the calibration set-up to ensure that the ion chamber and all dosimeters were positioned in the beam.

To provide the range of CT doses to determine calibration curves, four different sets of dosimeters were exposed at varying tube current settings (10-50 mA) at 120 kV. Additionally, two TLDs and one piece of radiochromic film were left unexposed for background correction. After at least 24 hours post-irradiation, the TLDs from both the phantom measurements and calibration were read using an automatic TLD reader (Harshaw 5500, *Thermo Fisher Scientific, Inc*., Waltham, MA) under nitrogen gas flow. Also at 24 hours post-irradiation, the calibration films were scanned using the procedure described in Section 4.2.2.

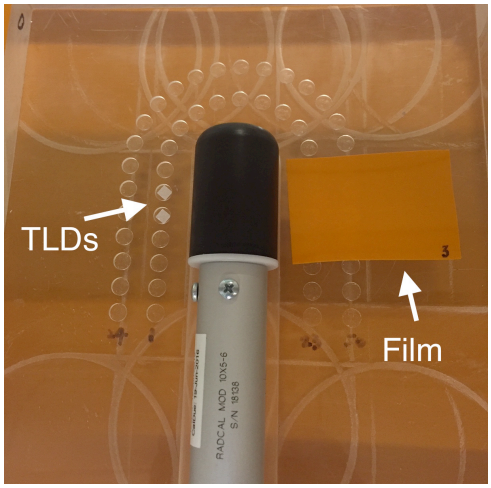

Figure 4.4: Set-up of the TLD and radiochromic film calibration. The ion chamber is place within a groove in the Plexiglas block such that the center of the chamber is at the same level of the TLDs and film.

To determine the calibration curve for the TLDs, the two TLD measurements were averaged at each dose level. The average measurement (in nC) was plotted against the absorbed dose to soft tissue. The absorbed dose from the ion chamber measurements was calculated using equation 4.2:

$$D_{\text{soft tissue}} = Rdg_{IC} \times CF_{IC} \times f \tag{4.2}$$

In equation 4.2, $D_{soft\ tissue}$ is the dose to soft tissue (in cGy), Rdg_{IC} is the raw ion chamber reading CF_{IC} is the ion chamber calibration factor (units: Roentgen/reading), and f is the f-factor for soft tissue. The f-factor used for this scanner is listed in Table 2.6. The average TLD measurement was plotted against the respective $D_{soft\ tissue}$ value, and linear regression analysis was used to determine the calibration fitting function in the form of equation 4.3. In this equation, m and b are fit parameters and nC is the raw light output reading measured by the TLD reader in nano-Coloumbs.

$$Dose = m \times nC + b \tag{4.3}$$

The film calibration curve was determined using a MATLAB® code adapted from software that was developed for a PhD dissertation by Sam Brady (St. Jude Children's Hospital) (126). Both the pre- and post-calibration images were loaded into the software and regions-of-interest (ROIs) were drawn in each of the calibration films to measure the pre- and post-irradiation optical density, and the net optical density was calculated using equation 4.1. The raw ion chamber readings for each of the dose levels, as well as the ion chamber correction factor and f-factor, were input into the software. Using these values, the software converted the raw ion chamber readings to absorbed dose in soft tissue (equation 4.2) and provided a modified exponential fitting function to convert the net optical density to absorbed dose in the form of equation 4.4 (123, 124).

$$Dose = a \times \left(e^{b \times netOD} - 1 \right) \tag{4.4}$$

In this equation, a and b are fit parameters, and $netOD$ is the net optical density.

4.2.4 Radiochromic Film Analysis

All film data was analyzed using the same software tool used to produce the calibration curve; this tool is a MATLAB® code adapted from software that was developed for a PhD dissertation by Sam Brady (St. Jude Children's Hospital) (126). The software registered the pre- and post-irradiation digitized films, and converted the pixel intensity values to netOD using equation 4.1 (124). The netOD values were then

converted to absorbed dose in soft tissue using the calibration curve generated from the methods described in Section 4.2.3.

For each of the films, anterior-posterior line profiles were extracted from the dose matrices at the location of the lens of the eye. The depth of the primary beam scan range boundary ($d_{primary}$) in the phantom was visually located on the line profile (Figure 4.5a) and confirmed on the image of the film (Figure 4.5b), and the difference (Δd) between $d_{primary}$ and the depth of the lens (d_{lens}) was calculated using equation 4.5:

$$\Delta d = d_{primary} - d_{lens} \tag{4.5}$$

The value of d_{lens} was taken to be 0.3 cm, based off of depth measurements of the anterior chamber of the eye (127). This is also the depth listed by the Nuclear Regulatory Commission (NRC) in the Code of Federal Regulations (10 CFR 20.1003) for measurement of lens dose equivalent (128).

The dose to the lens was taken as the average dose across a region-of-interest 25 pixels in the x-direction, which is approximately 9 mm, and 1 pixel in the y-direction at d_{lens} for both the left and the right eyes; the diameter of the human lens is approximately 9 mm (129). The pixel size for each of the images was 0.353 mm in both the x- and y-directions. The average lens dose was normalized to the $CTDI_{vol}$ recorded off of the structured dose report, and plotted against Δd.

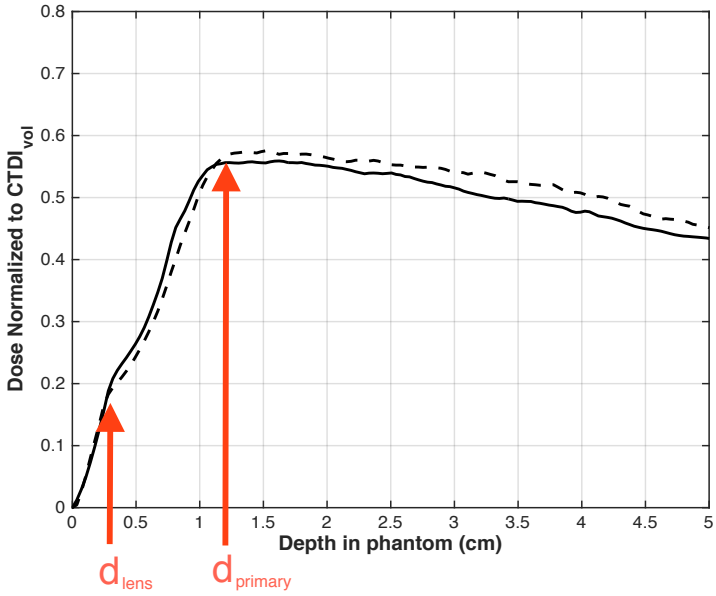

a)

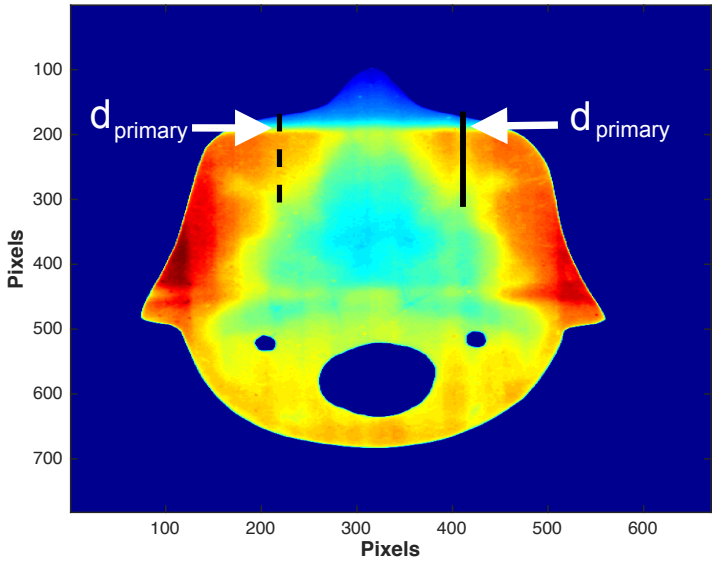

b)

Figure 4.5: Localization of primary beam depth on the a) the line profiles extracted from the radiochromic film and b) on the film itself. The depth of the lens was assumed to be 0.3 cm. The small circular regions that were cut out of the film were areas containing plugs that fit the two adjacent phantom slabs together. The large circular region was cut out of the film because this was the location of a cylindrical phantom insert that spanned two adjacent slabs. The dashed and solid lines on figure 4.5b are the locations of the line profiles plotted in figure 4.5a.

4.3 Results

The calibration curve and the fitting function dose error for the TLD measurements are displayed in Figures 4.6 and 4.7, respectively. The TLD calibration fit parameters, m and b, were determined to be 0.1485 and 0.0739, respectively, and the R^2 value was 0.995. The error in the fitting function did not exceed 8% for all the measured dose levels. The calibration curve and the fitting function dose error for the film measurements are displayed in Figures 4.8 and 4.9, respectively. The film calibration fit parameters, a and b, were determined to be 1.88 and 5.39, respectively, and the R^2 value was 0.9989. This fit equation yields dose values in units of cGy; during analysis, dose values were converted to mGy through multiplying initial values by a factor of 10. The error in the fitting function did not exceed 10% for all the measured dose levels.

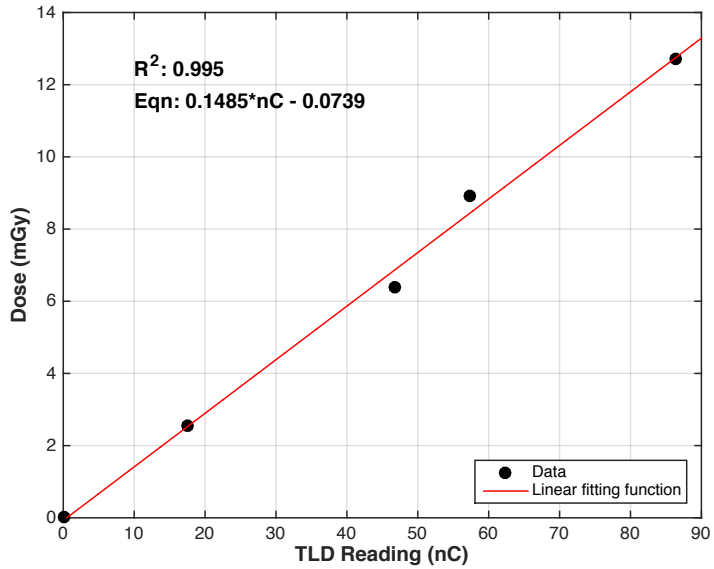

Figure 4.6: Calibration fitting function to convert from the raw TLD readings to absorbed dose

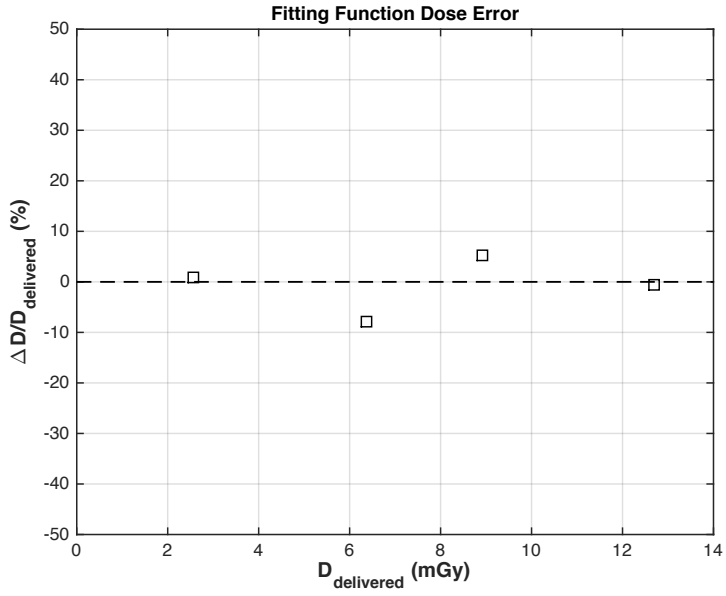

Figure 4.7: Plot of the error in the TLD calibration fitting function. The values plotted are the difference in percentage between the dose delivered to the TLD and the dose calculated using the fitting function.

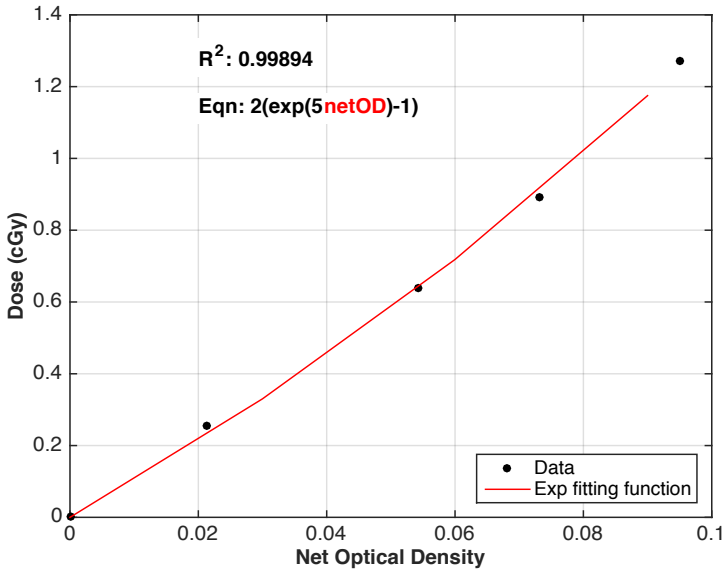

Figure 4.8: Calibration fitting function to convert from the net optical density measured on the radiochromic film to absorbed dose

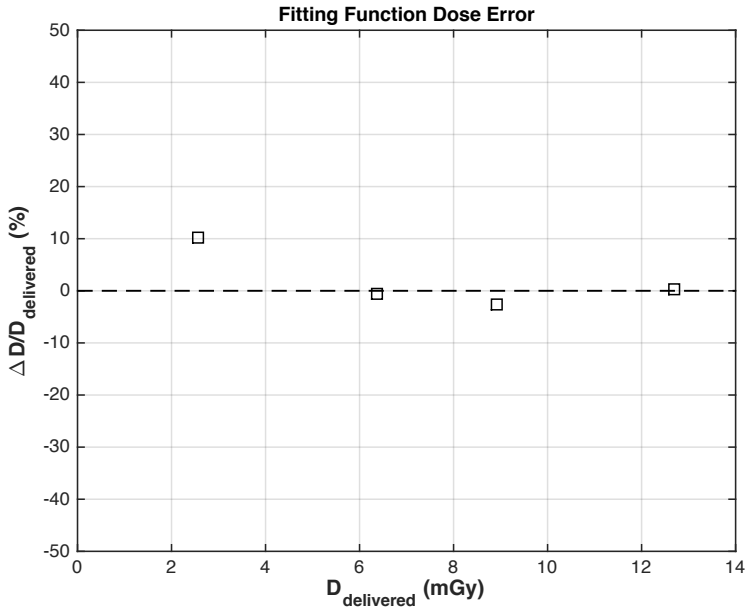

Figure 4.9: Plot of the error in the radiochromic film calibration fitting function. The values plotted are the difference in percentage between the dose delivered to the film and the dose calculated using the fitting function.

4.3.1 TLD Measurements of Lens Dose from Brain CT with Gantry Angulation

The average lens dose measured by the TLDs that were placed within the predrilled holes of the phantom are displayed in Figure 4.10; these doses ranged from 2.3 to 23.7 mGy depending on the phantom. The differences in lens dose are likely caused by differences in parameters of the imaging protocols (listed in Table 4.1) as well as the geometry of the physical phantoms, which change as the phantom age changes. However, gantry angulation may have contributed to the measured lens dose because the orientation and positioning of the scan range when the gantry is tilted influence whether or not the lens is located within the primary beam or within the scattered

region (Figure 4.1). The 2-D dose distributions measured by the radiochromic film can identify the cause of these differences and are discussed in the following section.

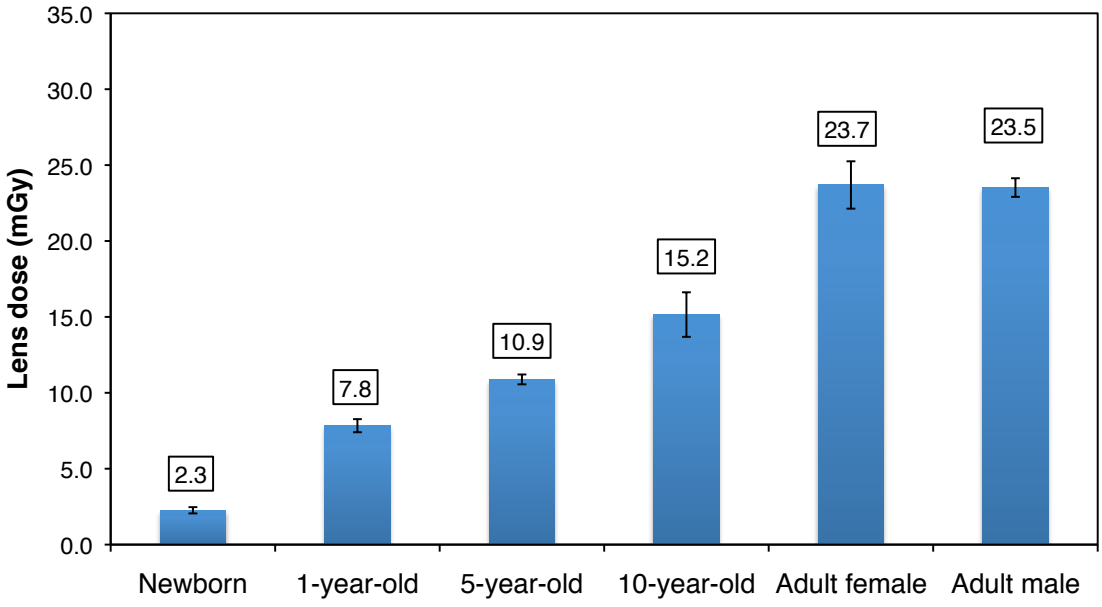

Figure 4.10: Radiation dose to the lens of the eye from the TLD measurements

4.3.2 Spatial Dose Distribution in the Head from Brain CT with Gantry Angulation

The 2-D distribution of dose measured with the radiochromic film within the phantom slices are shown in Figures 4.11a-f. In these figures, "Film 1" refers to the film placed superior to the lens location, and "Film 2" refers to the film placed inferior to the lens location.

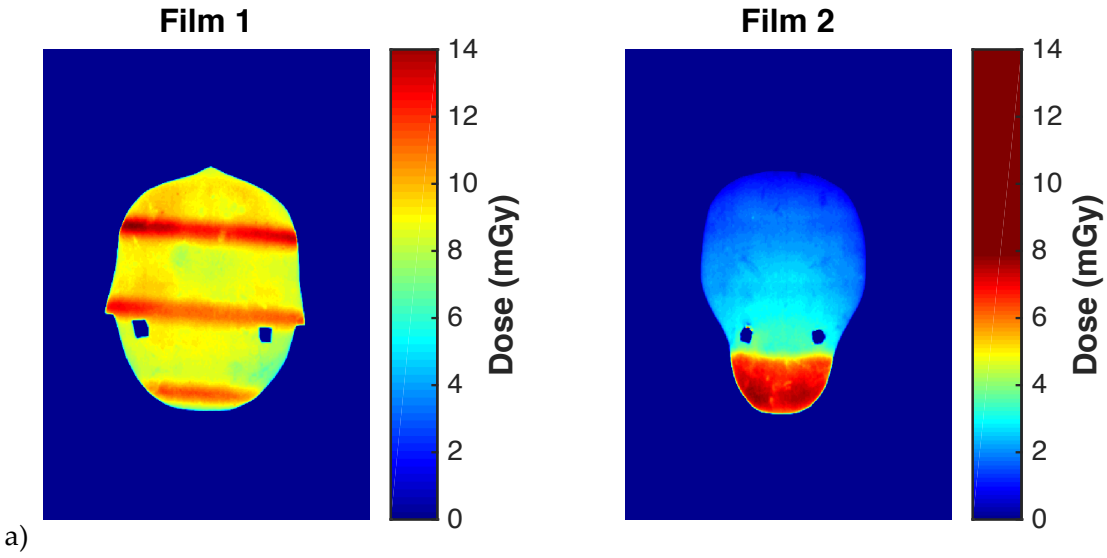
Film 1
Film 2
14
12
10
8
6
4
2
0
Dose (mGy)

a)

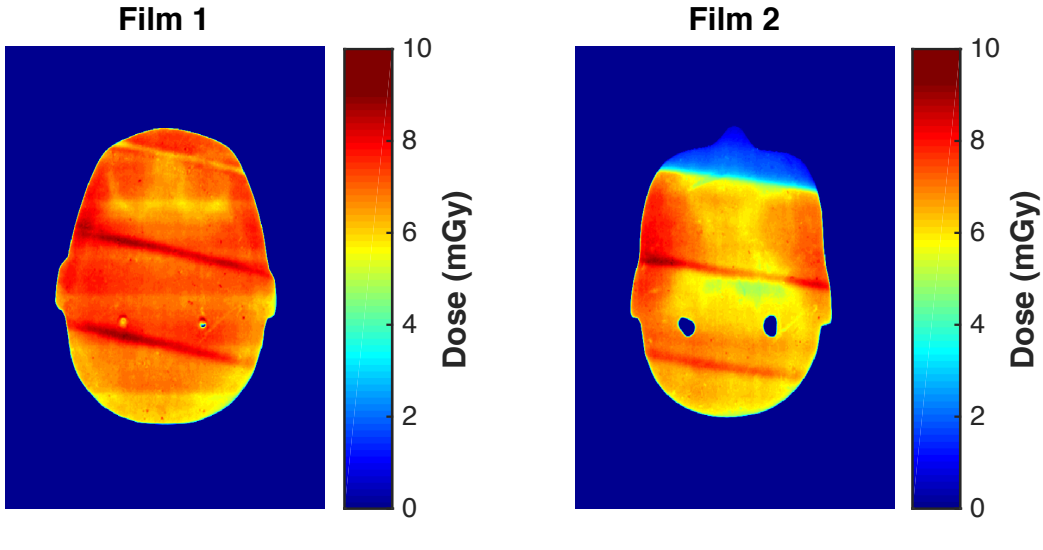
Film 1
Film 2
10
8
6
4
2
0
Dose (mGy)

b)

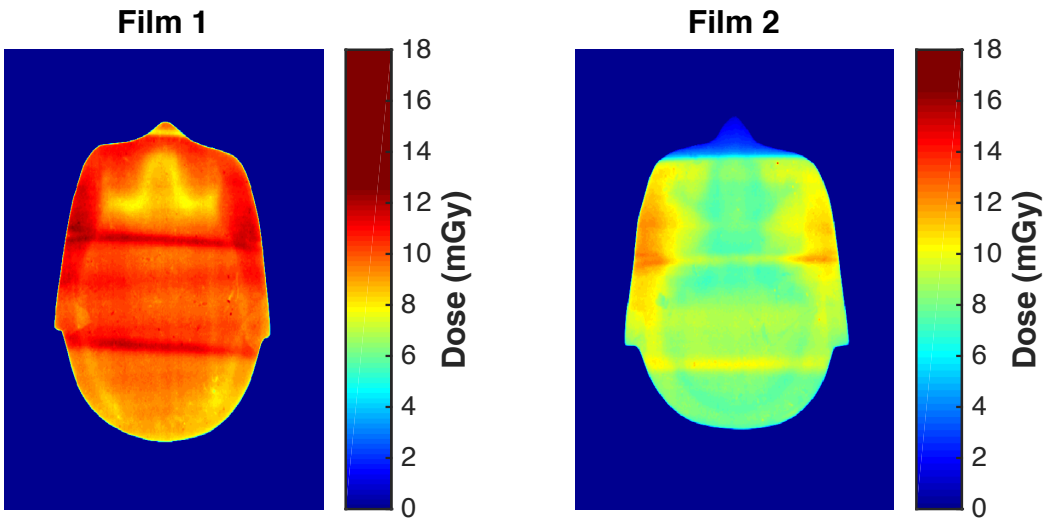
Film 1
Film 2
18
16
14
12
10
8
6
4
2
0
Dose (mGy)

c)

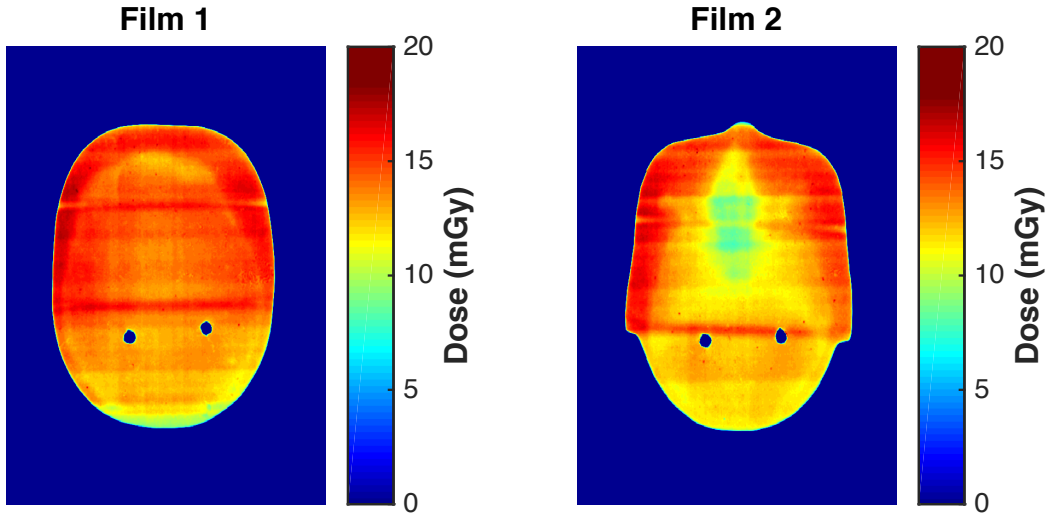
Film 1
Film 2
20
15
10
5
0
Dose (mGy)

d)

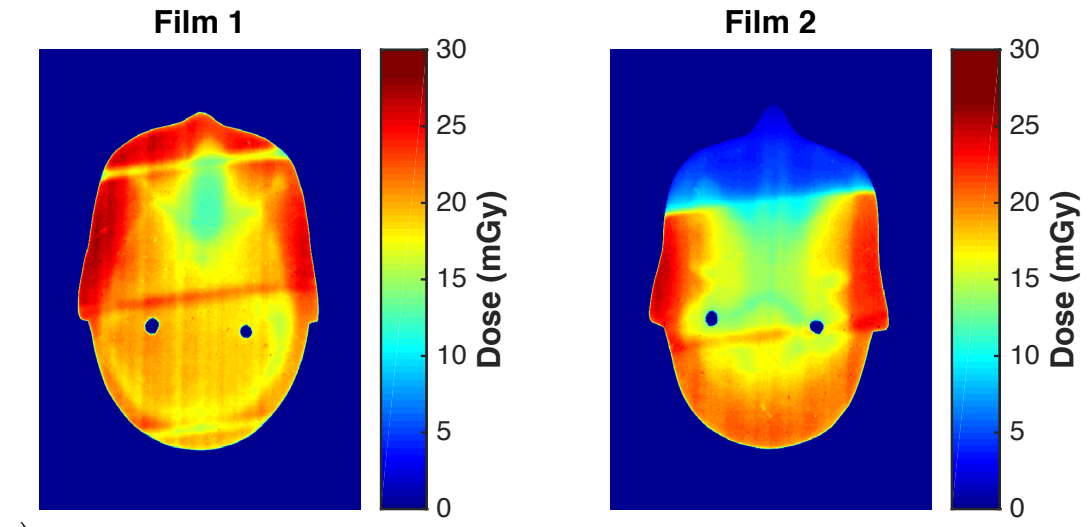

e)

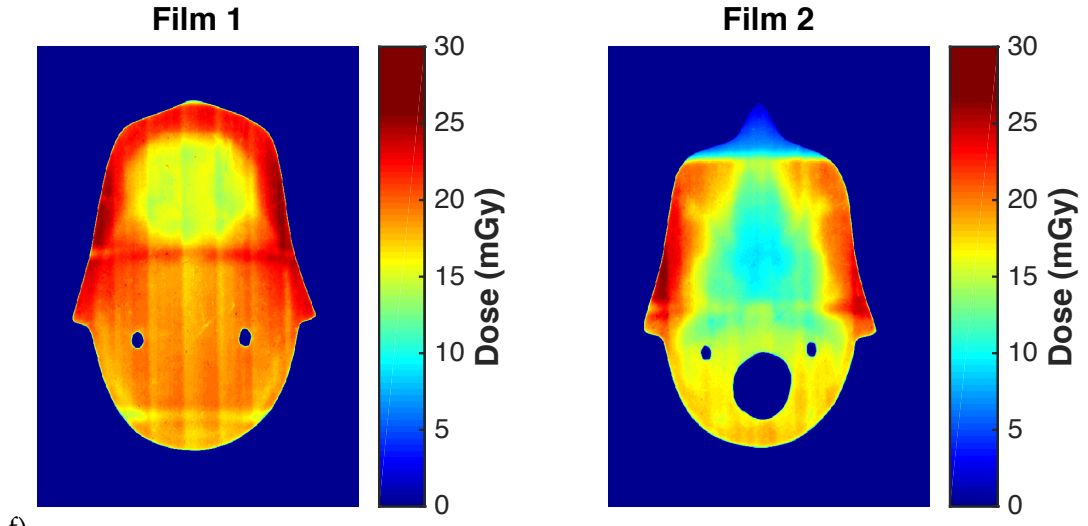

f)

Figure 4.11: Superior (left) and inferior (right) film measurements in the a) newborn, b) 1-year-old, c) 5-year-old, d) 10-year-old, e) adult female, and f) adult male phantoms. Film 1 and Film 2 refer to the films placed superior and inferior to the lens location, respectively. The small circular regions that were cut out of some of the films were areas containing plugs that fit the two adjacent phantom slabs together.

There are some inconsistencies with the dose distribution in the head, including the streaks of high dose regions that are particularly noticeable in the Newborn, 1-year-

old, and 5-year-old phantoms (Figures 4.11a-c). The cause of these streaks on the films is likely due to the gaps in the phantom between the slabs. The slabs of the phantoms were not tightened together using the bases because the top part of the base would serve as an attenuating material in the beam before it reached the phantom. Due to this, there were some air gaps between the slabs (Figure 4.12), which likely caused the streaks of higher dose on the films.

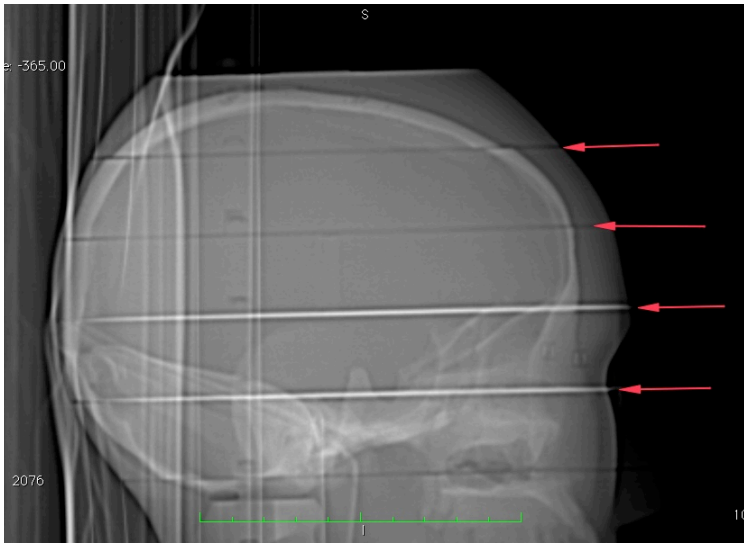

Figure 4.12: Lateral scout of the 10-year-old phantom. The arrows are pointing to the air gaps between the phantom slabs.

The effects of gantry angulation are particularly noticeable in Film 2 measured in the newborn, 1-year-old, 5-year-old, adult female, and adult male phantoms (Figures 4.11a, b, c, e, and f). These figures display clear delineation between the imaged volume (scanned with the primary beam) and the scattered dose region (located anteriorly by the orbits). Gantry angulation was not particularly evident in Film 1 of any of the phantoms, which is due to the fact that portions of the brain volume are present in this

area of the phantom. The scan range was positioned such that these portions of the brain volume would not be cut-off.

In Figures 4.11b and 4.11e, the lines signifying where the scan range ended in the 1-year-old and adult female are diagonal, which differ from the straight lines shown in the films from the 5-year-old and the adult male (Figures 4.11c and 4.11f). This is due to a slight rotation of the head in the 1-year-old and adult female phantoms during dose measurements. Figure 4.13 displays the lateral scout of the adult female; in this figure, the radiochromic film is not completely superimposed on itself, which indicates a slight rotation of the head. The lateral scout of the 1-year-old also shows rotation of the head, and is displayed in Appendix B.

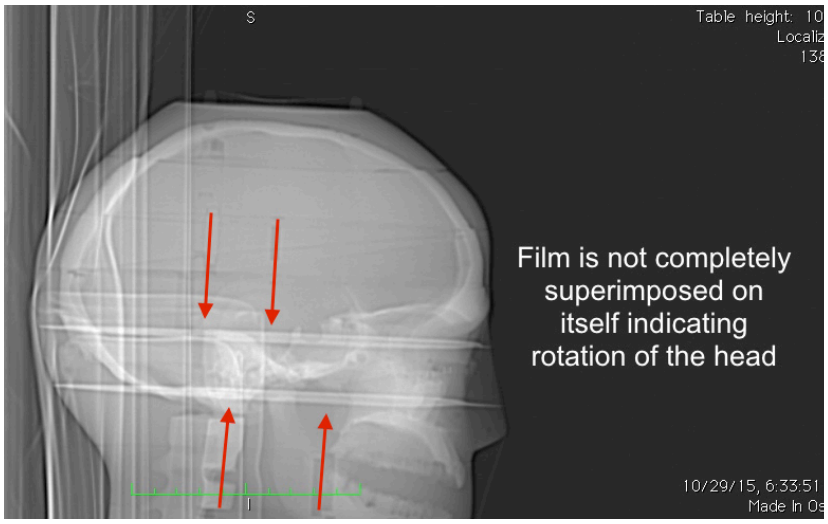

Figure 4.13: Lateral scout of the adult female. The film is not completely superimposed on itself (red arrows), which indicates a slight rotation of the head during dose measurements.

The average dose to the orbit at the depth of the lens (0.3 cm) measured on Films 1 and 2 for all phantoms is displayed in Figure 4.14. Except for the 10-year-old, the measured doses at the depth of the lens decreased substantially (ranging from 67 to 92%) on Film 2 compared to Film 1. This decrease is due to the fact that this region was located in the scattered dose region in Film 2 and was exposed to the primary beam in Film 1. The orbital dose measured in the 10-year-old was comparable between Film 1 and Film 2, which corresponds to the lack of a "cold" region (i.e. area not exposed with the primary beam) anteriorly in Figure 4.11d. In some cases, it is not possible to scan the entire brain volume and still avoid the lens when gantry angulation is employed, which is likely the case for the 10-year-old.

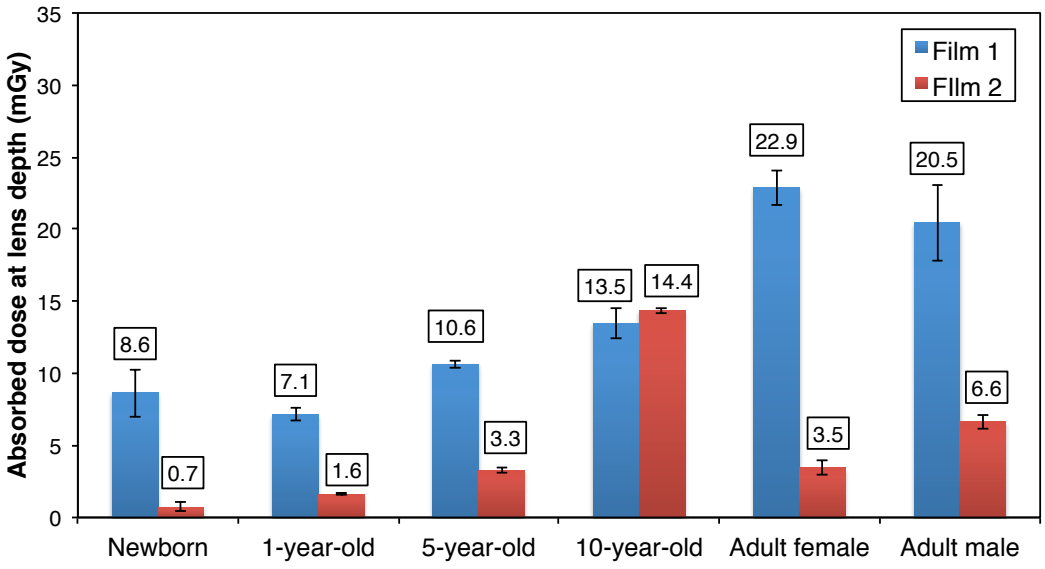

Figure 4.14: Radiation dose to the orbit at the depth of the lens, which is 0.3 cm from the anterior surface of the phantom. Film 1 and Film 2 refer to the superior and inferior films, respectively. The error bars indicate the standard deviation in the pixel values from the regions-of-interest extracted at the depth of the lens.

The difference in orbital dose measured in Films 1 and 2 compared to the TLD measurements are listed in Table 4.2. With the exception of the newborn phantom, the doses measured in Film 1 compared well to the TLD measurements with a range of 2.2 to 13.0%, which suggests that the TLDs placed in the predrilled location of the lens were included in the imaged volume for the 1-year-old through adult male phantoms despite employing gantry angulation. The newborn phantom had a much higher difference in orbital dose at the lens depth, with the dose measured in Film 1 being 282.0% higher than the TLD measurements. Since the gantry angulation in the protocol built to scan this phantom was extremely severe (Figure 4.11a), it is likely that the TLDs were exposed to only scattered radiation resulting in a much lower dose compared to that measured in Film 1. With the exception of the 10-year-old phantom, the difference was substantial for doses measured in Film 2 compared to the TLD measurements. This was because the lens dose measured in Film 2 was in the regions located anteriorly that were not exposed to the primary beam, and the TLDs (except for that of the newborn) were likely exposed to the primary beam, which was confirmed by the good agreement in dose compared to Film 1.

Table 4.2: Difference between the dose measured at the lens depth on Film 1 and Film 2 compared to the dose measured with TLDs

	Difference compared to TLD Measurements (%)	
Phantom	Film 1	Film 2
Newborn	282.0	68.4
1-year-old	9.1	79.5
5-year-old	2.2	70.0
10-year-old	11.1	5.2
Adult female	3.4	85.4
Adult male	13.0	71.8

In the four films where the scattered dose region was visible in the area of the orbit (Film 2 in Figures 4.11b, c, e, and f), line profiles in the anterior-posterior direction were extracted at the x-axis location of the lens of the eye and then the dose values were normalized to the respective $CTDI_{vol}$. The locations and plots of the line profiles are displayed in Figures 4.15a-d for the 1-year-old, 5-year-old, adult female, and adult male phantoms, respectively. Using the line profiles, the boundary between the dose contribution from the primary beam and scattered radiation was identified, and verified visually on the film images (discussed in Section 4.2.4).

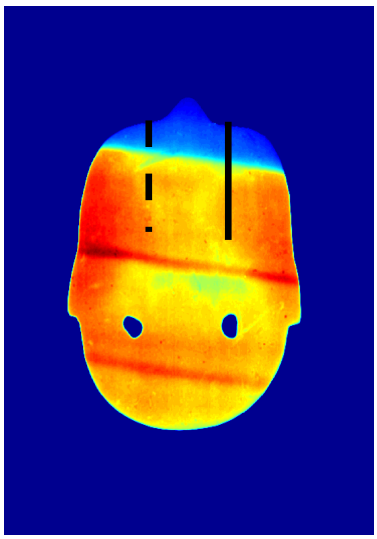

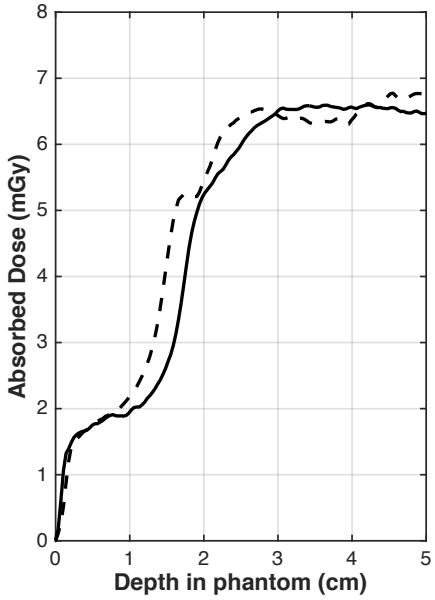
Absorbed Dose (mGy)
Depth in phantom (cm)
0
1
2
3
4
5
6
7
8

a)

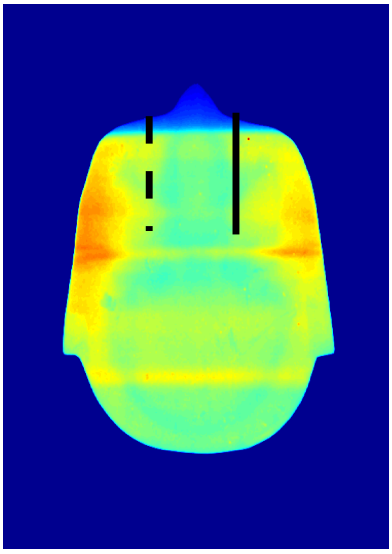

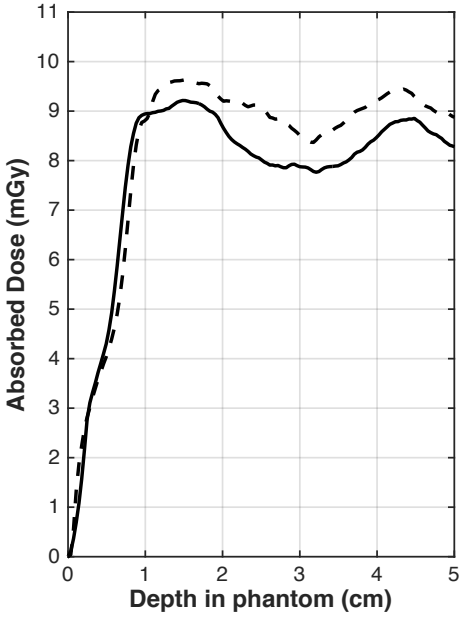
Absorbed Dose (mGy)
Depth in phantom (cm)
0
1
2
3
4
5
6
7
8
9
10
11

b)

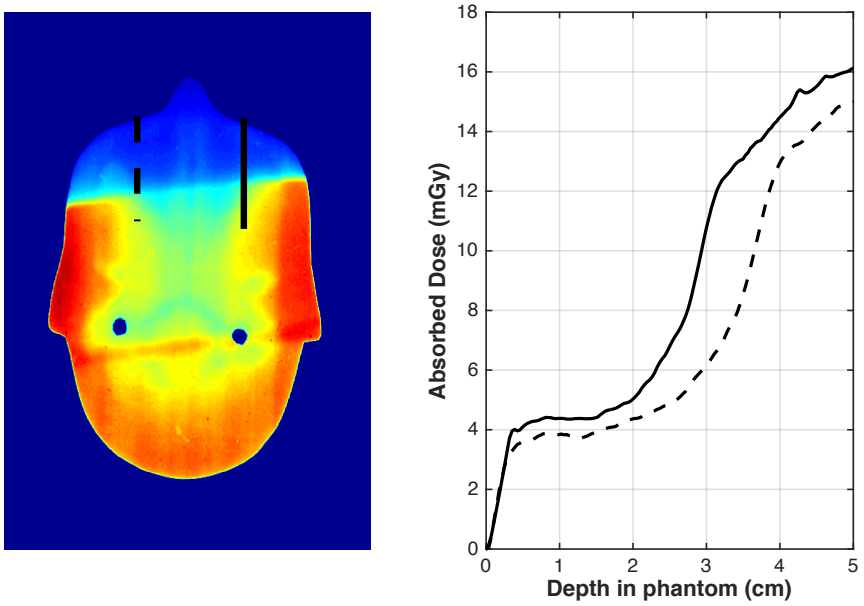

c)

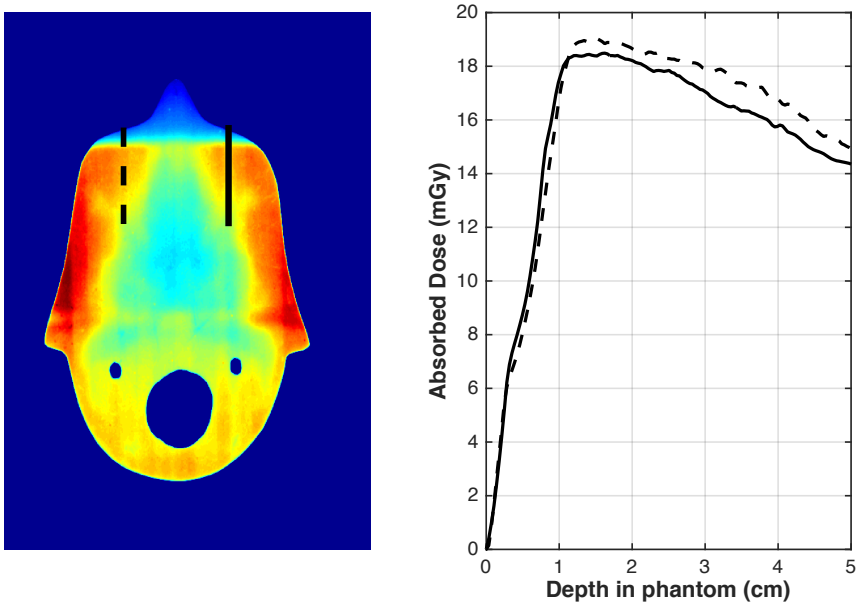

d)

Figure 4.15: Locations (left) and plot (right) of the line profiles from the film measurements in the a) 1-year-old, b) 5-year-old, c) adult female, and d) adult male phantoms. The x-axis on the line profile plot signifies the depth in the phantom from the anterior surface.

From the line profiles, the dose normalized to the respective $CTDI_{vol}$ was plotted against the distance anteriorly from the primary beam scan range boundary ($d_{primary}$); this is shown in Figure 4.16.

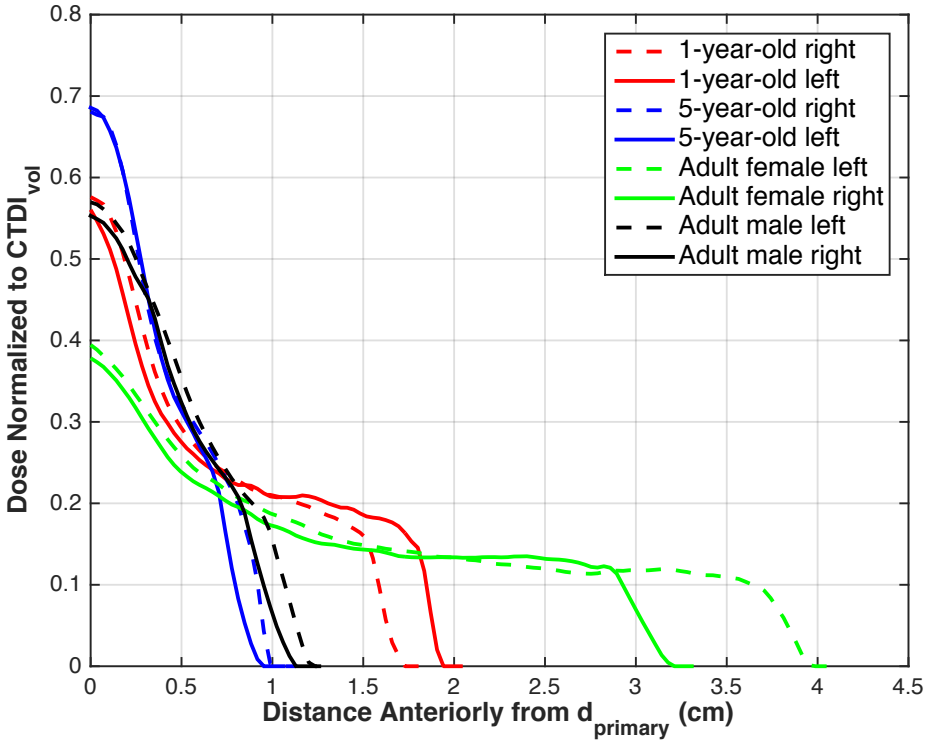

Figure 4.16: Plot of absorbed dose normalized to $CTDI_{vol}$ as a function of anterior distance from the primary beam scan range.

In Figure 4.16, the dose profiles in the scattered region for the 1-year-old, 5-year-old, adult female, and adult male appear to converge at a distance of about 0.5 cm from $d_{primary}$. Similar results were reported in a study using Monte Carlo simulations to determine the lens dose as a function of distance from the imaged volume (119). The different distances where the dose profiles fall-off to zero correspond to the phantom's

anterior surface; this is due to the fact that $d_{primary}$ was located at different depths within each of the different phantoms. However, the dose profiles seem to follow similar trends as each other and also agree with the expected shape of the scattered radiation dose profile in CT (130).

The doses at the depth of the lens in the scattered dose region from the 1-year-old, 5-year-old, adult female, and adult male were plotted against Δd, which is the difference between the depth of the primary beam scan range boundary ($d_{primary}$) and the depth of the lens (d_{lens}); this plot is displayed in Figure 4.17. The measured points were fit to a dual exponential function, which is the general shape of the contribution from the scatter tails to the radiation dose profile (130). Since the dose measured in these phantoms were in the regions not exposed to the primary beam, the dose contribution to these regions would be from scattered radiation, which is why a dual exponential function was used for the fit function. This equation could theoretically be used to determine the $CTDI_{vol}$-to-lens dose CF with knowledge of the distance from the primary beam scan range boundary to the lens in scans employing gantry angulation. The distance from the primary beam scan range to the lens could be measured using the image of the scan range overlaid on the lateral scout (Figure 4.3).

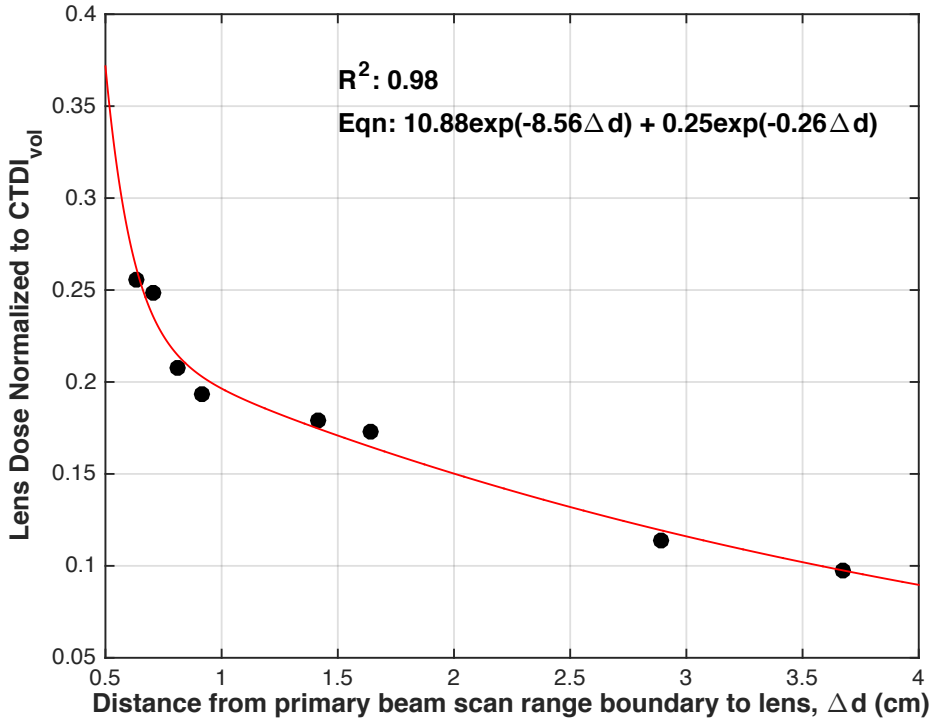

Figure 4.17: Plot of lens dose normalized to $CTDI_{vol}$ as a function of distance from the primary beam scan range boundary fit with a dual exponential function

To demonstrate the use of this function, the $CTDI_{vol}$-to-lens dose CF was calculated for the newborn phantom. The newborn phantom was chosen because the TLD measurements did not agree well with the measurements from either Film 1 or Film 2. The value of Δd was estimated using the angle of the gantry (18 degrees off perpendicular relative to the z-axis of the phantom from Table 4.1), the $d_{primary}$ value measured on Film 2 in Figure 4.10 ($d_{primary}$ = 7.02 cm), and the location of the TLDs using the scout (Figure 4.18).

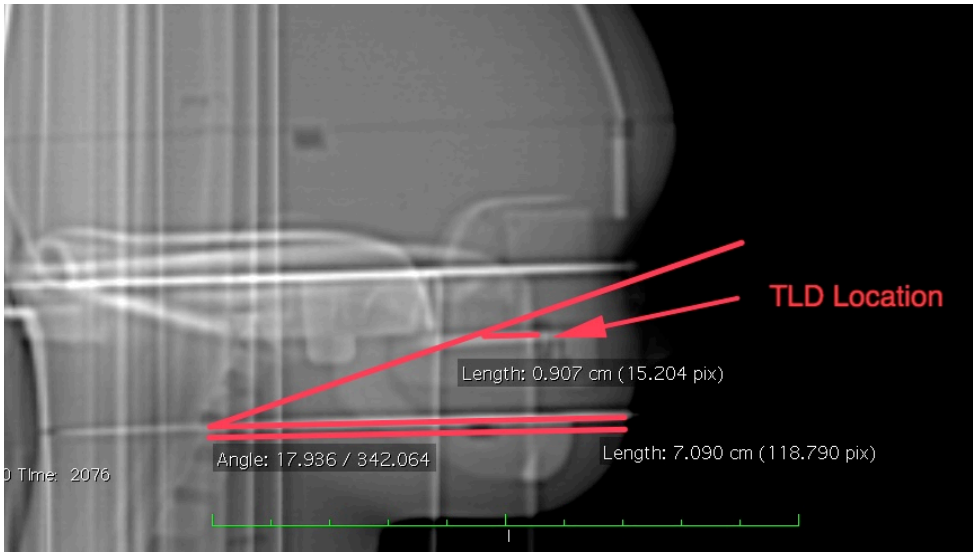

Figure 4.18: Measurement of Distance from Primary Beam Scan Range Boundary to TLD Location. The angled line corresponds to the angle of the gantry. The distance from the angled line to the TLD location was used as the value of Δd. The straight line at the bottom indicates the value of $d_{primary}$ measured on Film 2 from the newborn phantom.

The value of Δd, which in this case was the distance from $d_{primary}$ to the depth of the TLDs, was measured to be 0.907 cm. This value of Δd corresponded to a $CTDI_{vol}$-to-lens dose CF of 0.20 calculated using the fit function given in Figure 4.17. The $CTDI_{vol}$ used in the scan of the newborn ($CTDI_{vol}$ = 9.7 mGy) was multiplied by the $CTDI_{vol}$-to-lens dose CF, and the lens dose was determined to be 1.96 mGy. The calculated dose was comparable to the TLD measurements, with a dose difference of 13.3%.

4.4 Conclusions

In CT imaging of the brain, the dose to the lens of the eye can be reduced by angling the gantry or positioning the head such that the beam is parallel to the supraorbital plane (117). If the orbit is avoided when gantry angulation is implemented

in head CT, the lens would primarily be exposed to scattered radiation, and the amount of radiation dose it receives would be dependent upon the distance from the lens to the primary beam. One study investigated lens dose as a function of distance from the primary beam scan range to the lens of the eye in CT imaging of the head with gantry angulation and showed that the lens dose decreases as distance from the primary beam scan range increases (119). However, this study did not provide distance-specific $CTDI_{vol}$-to-lens dose conversion factors. Thus, the aim of this chapter was to investigate the effect of distance from the scan range on lens dose in CT imaging of the brain with gantry angulation.

The results of this study found that the average dose to the lens region decreased substantially for almost all the phantoms (ranging from 67 to 92%) when the orbit was in the scattered dose region (Film 2) compared to when it is scanned with the primary beam (Film 1). The lens dose measured in the 10-year-old was comparable between Film 1 and Film 2, which corresponds to the lack of a "cold" region anteriorly (i.e. a region not exposed to the primary beam) in this phantom. For this case, it is likely that, due to the phantom's anatomy, it was not possible to scan the entire brain volume and still avoid the lens with gantry angulation. The most important point to take away from this study is that gantry angulation did not result in a similar amount of dose reduction for each phantom. The effectiveness of this method to reduce lens dose is highly dependent

upon the shape and size of the head, which influences whether or not the angled scan range coverage can include the entire brain volume and still avoid the orbit.

To derive an equation that provides the $CTDI_{vol}$-to-lens dose CF based upon distance from the primary beam scan range to the lens, the lens doses from the scattered dose region in the 1-year-old, 5-year-old, adult female, and adult male were normalized to the respective $CTDI_{vol}$, plotted against Δd, and fit to a two-term exponential function, which is the general shape of the fall-off in dose spread functions (130). This equation was used to determine the distance-specific $CTDI_{vol}$-to-lens dose CF from the scan data for the newborn phantom, which was used to estimate lens dose with the respective $CTDI_{vol}$. The estimated lens dose was fairly comparable to the TLD measurement, with a 13% difference between the two. This equation could be used to determine the $CTDI_{vol}$-to-lens dose CF with knowledge of the distance from the primary beam scan range boundary to the lens in scans employing gantry angulation. However, in order to measure the distance from the primary beam scan range to the lens, the image of the scan range overlaid on the scout (Figure 4.2) is necessary, but this image is not always included with the set of tomographic images for a given exam.

Another point to discuss on gantry angulation is that it will likely not be a capability on future scanners. Scans without gantry angulation can be acquired faster compared to those with gantry angulation, which reduces motion artifacts. It is likely

that other dose reduction methods, like OB-TCM, will replace gantry angulation in head CT as the tilt capability on scanners is phased out.

5. Reconstruction of Radiation Dose to the Lens of the Eye in Pediatric Patients from CT Imaging of the Head

5.1 Introduction

The presence of lenticular opacities has been previously studied in individuals who were exposed to radiation as children and the findings seem to suggest that children's lenses may be particularly radiosensitive (64, 65, 69, 131). The populations investigated in these studies include children living close to the Chernobyl nuclear reactor (65), children receiving radiotherapy for skin hemangiomas (64), individuals who lived in radiocontaminated buildings in Taiwan (131), and atomic bomb survivors (69). However, there have been no investigations into the presence of lens opacities in children who have received multiple head CT examinations.

Several studies have investigated the cumulative radiation dose to the lens from repeated head CT scans in children (92, 132, 133). Holmedal *et al.* determined that cumulative lens doses to children who frequently undergo head CT scans for shunt-treated hydrocephalus range from 12 to 129 mGy (132). However, while it is established that CTDI and patient doses are not the same (101), this study estimated lens dose from measurements of $CTDI_{peripheral}$ (described in Section 2.1.1) in 10- and 16-cm diameter phantoms (132). Michel *et al.* determined that cumulative lens doses ranged from 50 to 970 mGy in children who were treated for cholesteatoma (92). This study only examined lens doses for 32 children and exposure history was determined with a medical questionnaire, which was confirmed through a review of medical records for 25 of the 32

subjects (92). Lastly, Bernier *et al.* determined that cumulative lens doses ranged from 0 to 1392 mGy in a study of 27,362 pediatric patients in France (133). However, this study estimated lens doses using technical parameters from general imaging protocols used in each hospital's radiology department; they did not account for differences in the technical parameters for each individual exam. Additionally, none of these studies have accounted for differences in patient head size, which would likely cause some discrepancies in reconstructed lens doses.

Thus, the objective of this chapter is to use the size-specific dose estimation methods (described in Chapter 2 and Chapter 3) to reconstruct lens doses in pediatric patients who received CT scans of the head at Duke University Medical Center.

5.2 Materials and Methods

A retrospective review of the radiology and electronic medical records was performed for 206 pediatric patients who underwent CT imaging of the head between 2009 and 2013. This retrospective review was part of an IRB-approved study (eIRB study Pro00048517); the protocol for this study is listed in Appendix C.

5.2.1 Patient Selection and Data Collection

A list of all head imaging exams that occurred between 2009 and 2013 was produced for patients ranging in age from 0- to 18-years-old. The head imaging exams included the brain ("CT Brain"), sinuses ("CT Sinus"), CT head angiography ("CTA Head"), orbits ("CT Orbital"), and temporal bones ("CT Temporal Bones") protocols.

The patient information that was acquired for each exam included the name, medical record number (MRN), date of birth, exam date, age at exam date, scanner room number, and the reason for the exam. The initial list contained approximately 10,000 exams.

To reduce the number of exams for data collection during the review of patient records, the exams were sorted by MRN for each year and patients were selected for record review if they received 4 or more head CT exams in one year. If a patient was selected, a search was performed in the exams for each of the other years included in this study; all exams listed for a patient between 2009 and 2013 were logged for collection of dose data (Figure 5.1). A total of 206 pediatric patients were selected for record review.

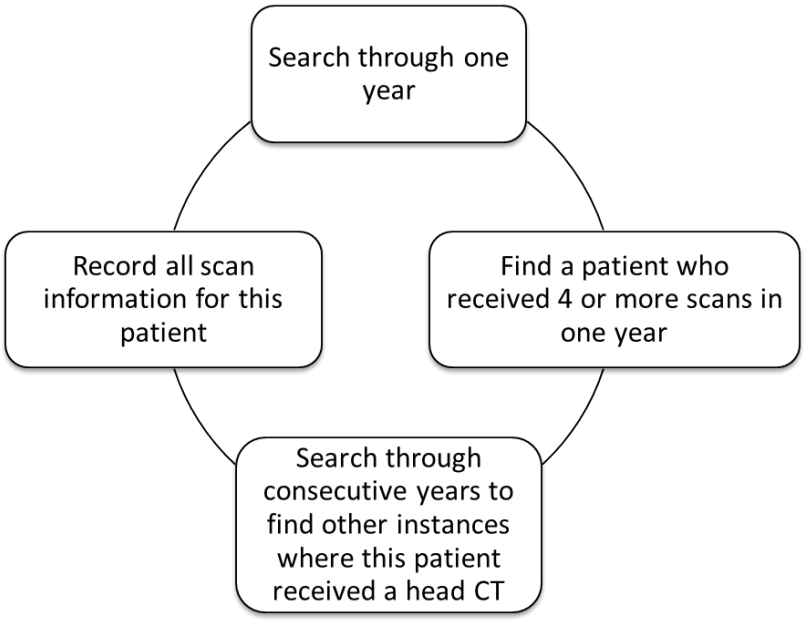

Figure 5.1: Methodology used to select patients for the retrospective study

The Maestro Care application was used to review the medical records of the patients selected for this study; this application was accessed via the Citrix Web Interface for Duke Health (https://awi.duhs.duke.edu/Citrix/XenApp/auth/login.aspx). After logging into Maestro Care, medical records were accessed by selecting the "Chart" tab on the upper toolbar of the home page (Figure 5.2).

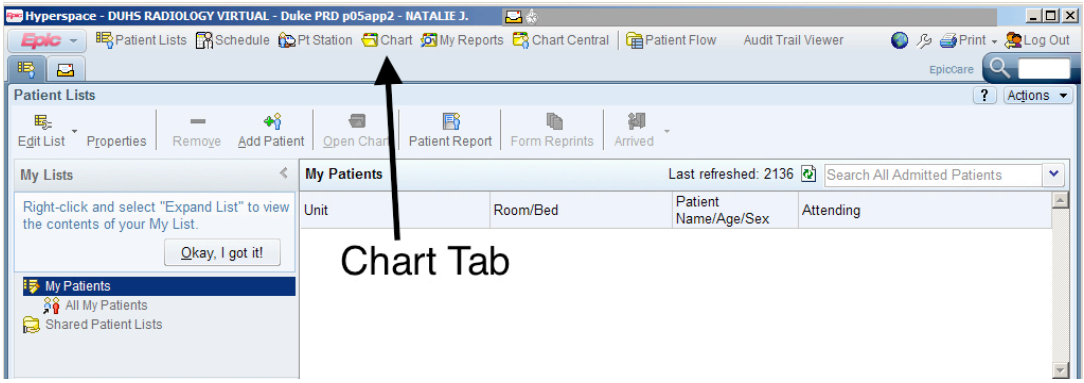

Figure 5.2: Location of the "Chart" tab on the Maestro Care home page

After the "Chart" tab was selected, a separate window appeared, which allowed the user to search for a medical record with patient identifiers such as name or MRN (Figure 5.3).

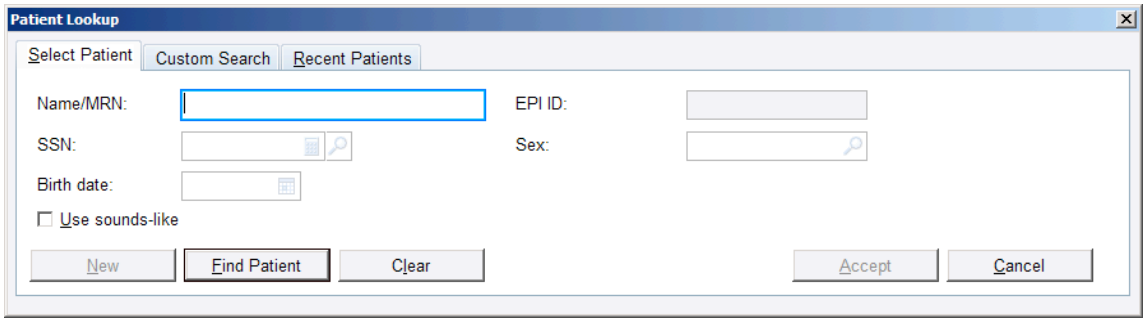

Figure 5.3: Patient lookup window in Maestro Care

After finding a patient's medical record, the "Chart Review" tab was selected, which accessed information such as medical encounters, test results, and imaging studies. In the "Chart Review" tab, the "Imaging" tab was selected, which accessed the patient's imaging history. The locations of the "Chart Review" and "Imaging" tabs are shown in Figure 5.4.

After finding the appropriate CT exam in the "Imaging" tab, the "Show available links" tool was selected, which provided options to view information related to the exam, such as the acquired images or the external result report. Since this study was interested in collecting data from the structured dose report, the "Show images" option was selected, which opened the DICOM imaging viewer. Typical imaging series found in the viewer for each exam included the scout image, the axial or helical tomographic images, and the structured dose report. Examples of structured dose reports are shown in Figures 2.6 and 2.7.

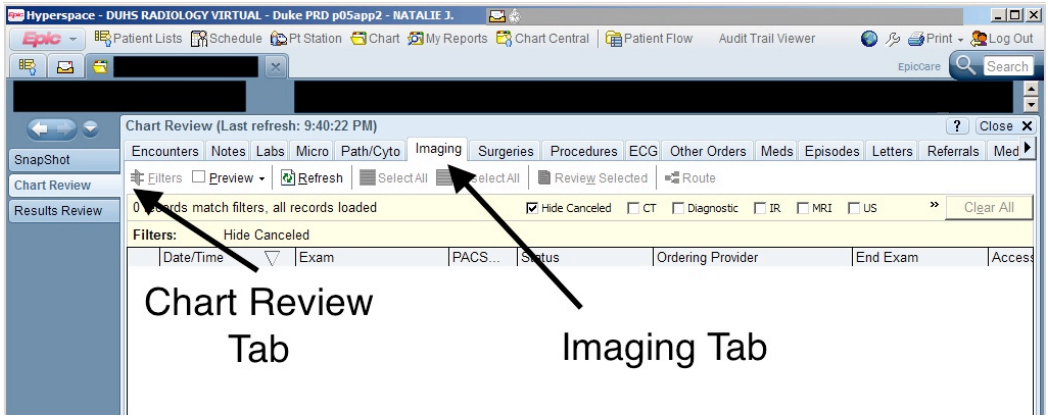

Figure 5.4: Location of the "Chart Review" and "Imaging" tabs in a chart accessed through Maestro Care

For each exam, the tomographic images were reviewed to ensure that the lens of the eye was included in the scan. Exams where gantry angulation is employed or when the patient's head is tilted down (which is similar to employing gantry angulation) comprise instances where the lens may not be included in the scan. If the lens of the eye was included in the scan, the $CTDI_{vol}$ was recorded in an Excel spreadsheet alongside the rest of the patient data related to the exam. If the lens was not included, the $CTDI_{vol}$ was not recorded and an explanatory note was made in the Excel spreadsheet for the particular exam. While it may be possible to reconstruct the lens dose with knowledge of the distance from the end of the scan to the lens (Figure 4.23), measurement of the distance would need to be made on the scout that displays the scan range (Figure 4.2), which was not always included in the images provided in the patient's medical record.

Lastly, AP and LAT diameters were measured in the supraorbital region of the head using methods described in Section 2.2.6. These values were recorded for each exam in the Excel spreadsheet alongside the $CTDI_{vol}$. Before beginning data analysis, patient identifiers, including name, MRN, and the month and day of the exam, were removed from the spreadsheet.

In order to identify which scanner model was used for each exam, a key was created that identified the scanner model housed in a given hospital room number for each year included in this study (Table 5.1). It was assumed that OB-TCM was employed for each head exam on Siemens scanners from the year 2010 onwards; the

year in which OB-TCM was implemented in head imaging protocols was confirmed with Carolyn Lowry, a head CT technologist at Duke University Medical Center.

To shorten some of the scanner names in Table 5.1, "DF" is used to represent the Definition Flash scanner, "L-XTRA" is used to represent the Lightspeed XTRA, and "D-750 HD" is used to represent the Discovery 750 HD. Of the scanners listed in Table 5.1, the Lightspeed, Lightspeed XTRA, VCT, and Discovery 750 HD scanners were manufactured by GE. The Definition and Definition Flash were manufactured by Siemens. The CereTom is a portable CT scanner and is manufactured by NeuroLogica.

Table 5.1: Locations of CT scanner models from 2009 to 2013

Room	2009	2010	2011	2012	2013
B5	Lightspeed	Lightspeed	Lightspeed	DF	DF
C1	VCT	Definition	Definition	DF	DF
C3	Lightspeed	Lightspeed	Lightspeed	D-750 HD	D-750 HD
J1	L-XTRA	L-XTRA	L-XTRA	Lightspeed	Lightspeed
J3	Lightspeed	Lightspeed	Lightspeed	Lightspeed	Lightspeed
CTER_1	VCT	VCT	VCT	Lightspeed	Lightspeed
CTER_2	-	-	VCT	Lightspeed	Lightspeed
CTS_3	-	-	D-750 HD	-	-
PO	-	CereTom	-	-	-

5.2.2 Size-Based Lens Dose Reconstruction

For each patient, the cumulative lens dose was calculated using equation 5.1. This equation requires knowledge of whether or not OB-TCM was implemented for a particular exam.

$$ {}_{cum}D_{lens} = \sum\left[\left(CF_{size} \times CTDI_{vol}\right) + \left({}_{OB-TCM}CF_{size} \times {}_{OB-TCM}CTDI_{vol}\right)\right] \quad (5.1) $$

In this equation, ${}_{cum}D_{lens}$ is the cumulative lens dose, CF_{size} is the size-based $CTDI_{vol}$-to-lens dose CF calculated using equation 2.6, $CTDI_{vol}$ is the volume CTDI recorded off of the structured dose report saved in the electronic medical record, ${}_{OB-TCM}CF_{size}$ is the size-based $CTDI_{vol}$-to-lens dose CF calculated using equation 2.6 for situations when OB-TCM is employed, and ${}_{OB-TCM}CTDI_{vol}$ is volume CTDI for scans in which OB-TCM is employed.

5.3 Results

5.3.1 Age-Head Size Relationship

The relationship between the effective head diameter and patient age is shown in Figure 5.5. This curve shows a rapid increase in head size in between 0 to 2 years old and then gradually increases with age after that. The pattern is similar to the head circumference growth reference charts from birth to adulthood in the United States published by Rollins *et al.* in 2010 (134).

The effective diameter values in the age group from 0 to 2 years old may not be completely indicative of head sizes in healthy children. This is because a large number of children receiving multiple head CTs have hydrocephalus, which is a condition of excessive fluid in the brain. Since the cranial fontanelles do not usually close until around 18 months of age, increased fluid in the head can result in an increase in head circumference in this age group.

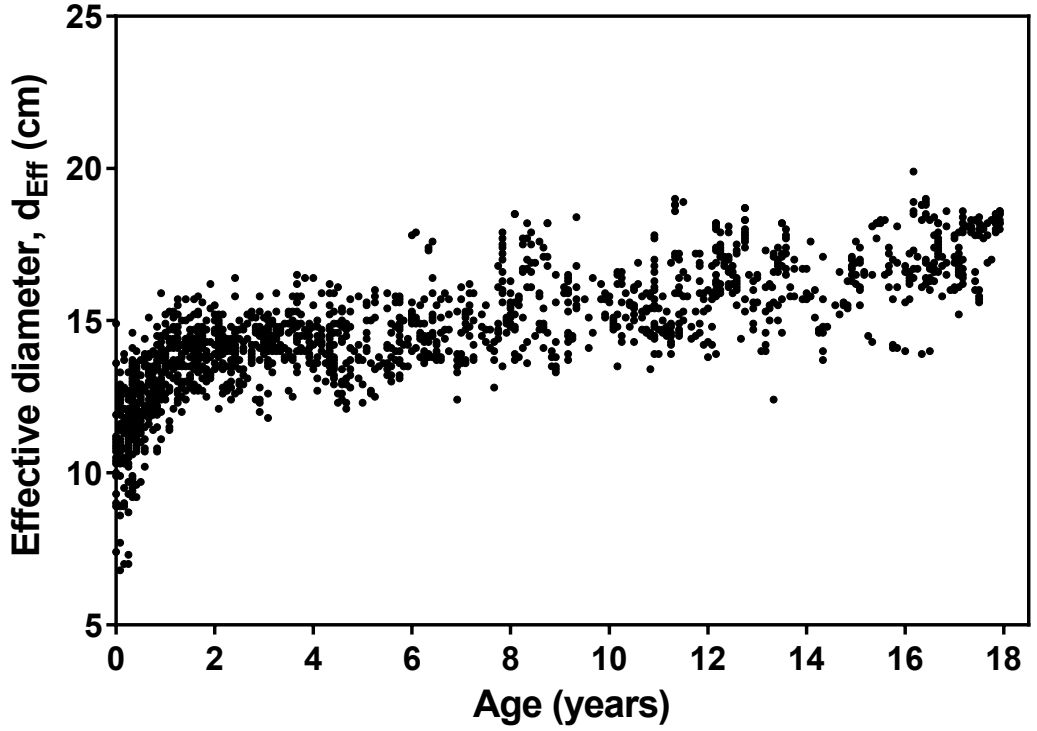

Figure 5.5: Relationship between age and effective head diameter from the pediatric patients included in this retrospective study

5.3.2 Exam Distribution

The distribution of the type of head CT exams for which dose data was collected in the retrospective pediatric patient study is displayed in Figure 5.6. Out of the 2149 head CT exams included in this study, the majority were CT imaging of the brain, followed by CT imaging of the sinuses, CT angiography of the head, and CT imaging of the orbits, and temporal bones. Since this study determined that CT imaging of the brain was the most prevalent protocol in pediatric patients who frequently receive head CT exams, the potential to reduce dose to the lens in this population is high if gantry angulation (or head tilt) is implemented on a regular basis.

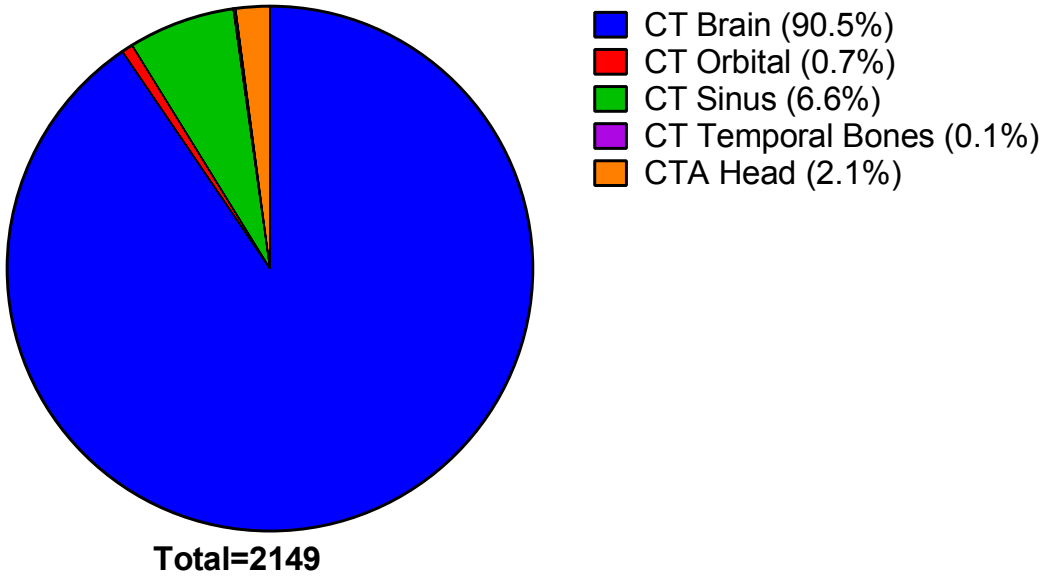

Figure 5.6: Distribution of head CT exams in the pediatric retrospective study

5.3.3 Lens Dose Per Head CT Exam

The distribution of lens dose per exam in the CT Brain protocol is listed in Table 5.2 for the 0 to 3, 4 to 7, 8 to 12, and 13 to 18 year old age groups. The data included in this table are the minimum, 25th percentile, median, 75th percentile, and maximum. The mean and standard deviation, and upper and lower 95% confidence intervals (CI) of the mean of the lens dose per exam in the CT Brain protocol are also listed in Table 5.2. In general, the results show that the lens dose increases as the age range increases, with the mean dose ranging from 14.5 in the 0 to 3 year olds up to 37.4 and 36.8 in the 8 to 12 and 13 to 18 year olds, respectively. This is perhaps due to the age-specific protocols used at our institution, which generally increase the tube current as the age range increases resulting in higher dose.

Table 5.2: Lens dose statistics for the CT Brain protocol in the pediatric retrospective study

	Lens dose (mGy)			
Age (years)	0-3	4-7	8-12	13-18
Number of values	855	348	354	318
Minimum	4.0	4.0	7.5	8.2
25th Percentile	12.3	12.5	31.2	31.0
Median	13.4	13.7	40.7	39.2
75th Percentile	14.7	19.9	44.7	41.8
Maximum	55.7	52.0	55.5	82.1
Mean	14.5	19.2	37.4	36.8
Standard deviation	5.0	11.7	10.2	8.2
Lower 95% CI of mean	14.1	18.0	36.4	35.9
Upper 95% CI of mean	14.9	20.5	38.5	37.7

Since there were only 15 values collected for the CT Orbital protocol, they were grouped all together instead of performing age-specific analysis. The minimum, 25th percentile, median, 75th percentile, maximum, mean and standard deviation, and upper and lower 95% CI of the mean are listed in Table 5.3 for the CT Orbital protocol. The mean lens dose per CT Orbital protocol was determined to be 15.1 ± 11.9 mGy. The high standard deviation is due to the fact that our sample size for this protocol is very low, and we are grouping all of the age ranges together, which vary in lens dose among each other.

Table 5.3: Lens dose statistics for the CT Orbital protocol in the pediatric retrospective study

	Lens dose (mGy)
Age (years)	0-18
Number of values	15
Minimum	4.7
25th Percentile	7.4
Median	8.4
75th Percentile	25.8
Maximum	47.4
Mean	15.1
Standard deviation	11.9
Lower 95% CI of mean	8.5
Upper 95% CI of mean	21.7

The distribution of lens dose per exam in the CT Sinus protocol is listed in Table 5.4 for the 0 to 3, 4 to 7, 8 to 12, and 13 to 18 year old age groups. Similar to the trend observed in the CT Brain protocol, the lens dose per CT Sinus exam increases with increasing age. The mean lens dose increased from 11.8 in the 0 to 3 year old to 21.6 in the 13 to 18 year olds. This could be due to the age-specific protocols used at our institution, which have variations in technical factors (i.e. tube current) resulting in variations in lens doses.

Table 5.4: Lens dose statistics for the CT Sinus protocol in the pediatric retrospective study

	Lens dose (mGy)			
Age (years)	0-3	4-7	8-12	13-18
Number of values	31	35	43	32
Minimum	3.5	2.2	4.6	9.4
25th Percentile	5.8	11.0	10.5	14.2
Median	11.6	12.0	18.4	24.2
75th Percentile	13.1	22.6	25.2	26.0
Maximum	28.3	48.1	49.2	41.9
Mean	11.8	16.6	19.4	21.6
Standard deviation	6.6	10.7	9.3	7.6
Lower 95% CI of mean	9.4	12.9	16.5	18.9
Upper 95% CI of mean	14.2	20.3	22.2	24.4

There were only three values collected for the CT Temporal Bones protocol, all of which were in the 13 to 18 year old age range. From these three values, the mean lens dose for the CT Temporal Bones protocol was determined to be 30.9 ± 2.9 mGy.

Since there were only 44 values collected for the CTA Head protocol, they were grouped all together instead of performing age-specific analysis. The minimum, 25th percentile, median, 75th percentile, maximum, mean and standard deviation, and upper and lower 95% CI of the mean are listed in Table 5.5 for the CTA Head protocol. The mean lens dose per protocol was determined to be 34.1 ± 18.9 mGy. Like the CT Orbital protocol, the high standard deviation is due to the fact that our sample size for this

protocol is very low, and we are grouping all of the age ranges together, which vary in lens dose among each other.

Table 5.5: Lens dose statistics for the CTA Head protocol in the pediatric retrospective study

	Lens dose (mGy)
Age (years)	0-18
Number of values	44
Minimum	5.6
25th Percentile	20.2
Median	31.7
75th Percentile	48.7
Maximum	104.8
Mean	34.1
Standard deviation	18.9
Lower 95% CI of mean	28.3
Upper 95% CI of mean	39.8

5.3.4 Cumulative Lens Dose

A histogram of the reconstructed cumulative lens dose is shown in Figure 5.7. In the pediatric patients included in this study, the cumulative lens dose ranged from 40 to 1020 mGy. If this study assumes the threshold dose proposed by the ICRP of 500 mGy (56), there were 17 out of 206 patients (8.3%) that received cumulative doses exceeding the dose threshold.

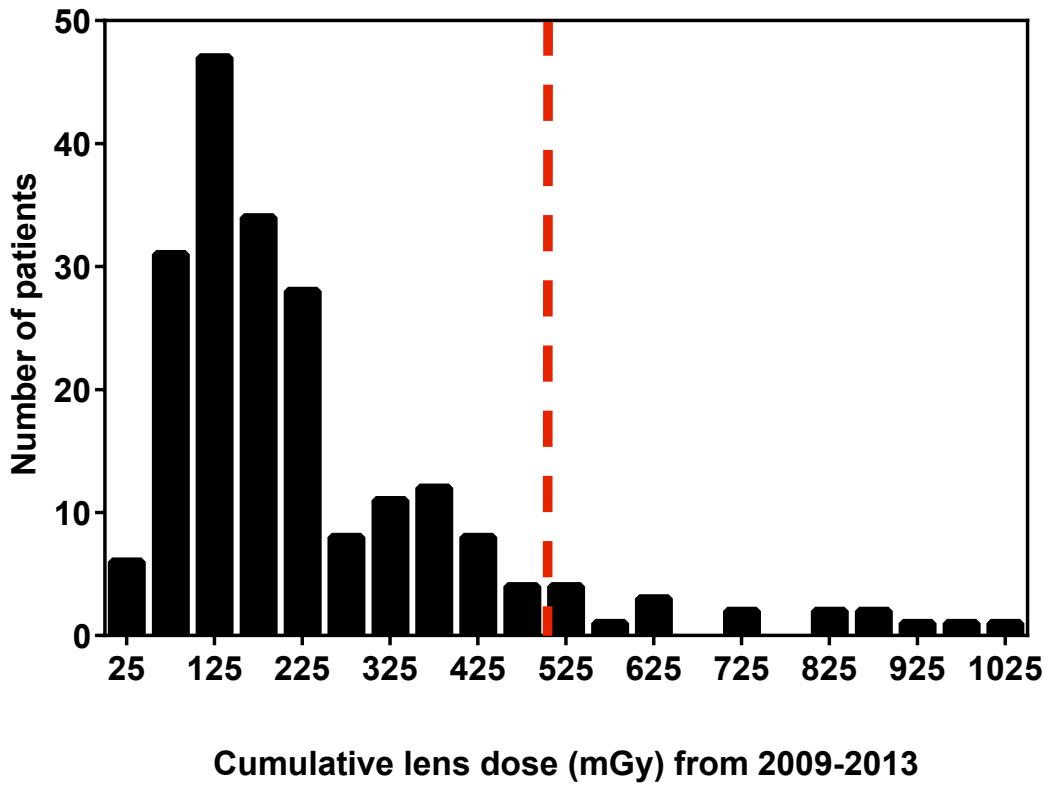

Figure 5.7: Histogram of cumulative lens dose from the pediatric retrospective study. The red dashed line represents the ICRP threshold dose for radiation-induced cataractogenesis.

The relationship between cumulative lens dose and total number of exams is displayed in Figure 5.8. In general, this figure shows a linear increase in the cumulative lens dose as the total number of exams increases. It has a fairly wide distribution, likely because the lens dose varies widely in children based upon their head size. Additionally, different technical factors are implemented in a given imaging exam based upon the age of the patient, which also influences the lens dose per exam.

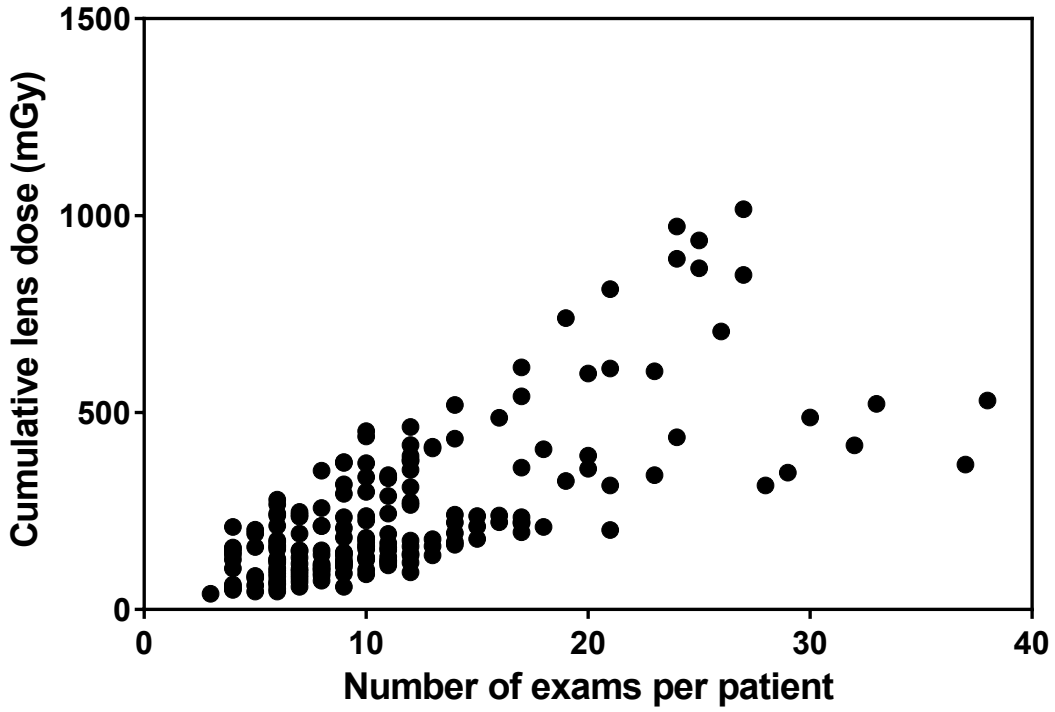

Figure 5.8: Relationship between cumulative lens dose and the number of exams per patient

5.3.5 Lens Dose per Year in Patients Exceeding the ICRP Threshold Dose for Cataract Formation

The lens dose per year in the 17 patients who had cumulative lens doses exceeding 500 mGy are displayed in Figure 5.9a-b. Of these 17 patients, there were 7 patients out of 206 (3.4%) that exceeded that value in one year, and no patient exceeded that value in more than one year. These patients include numbers 4 and 6 on Figure 5.9a, and 10, 11, 12, 16, and 17 on Figure 5.9b.

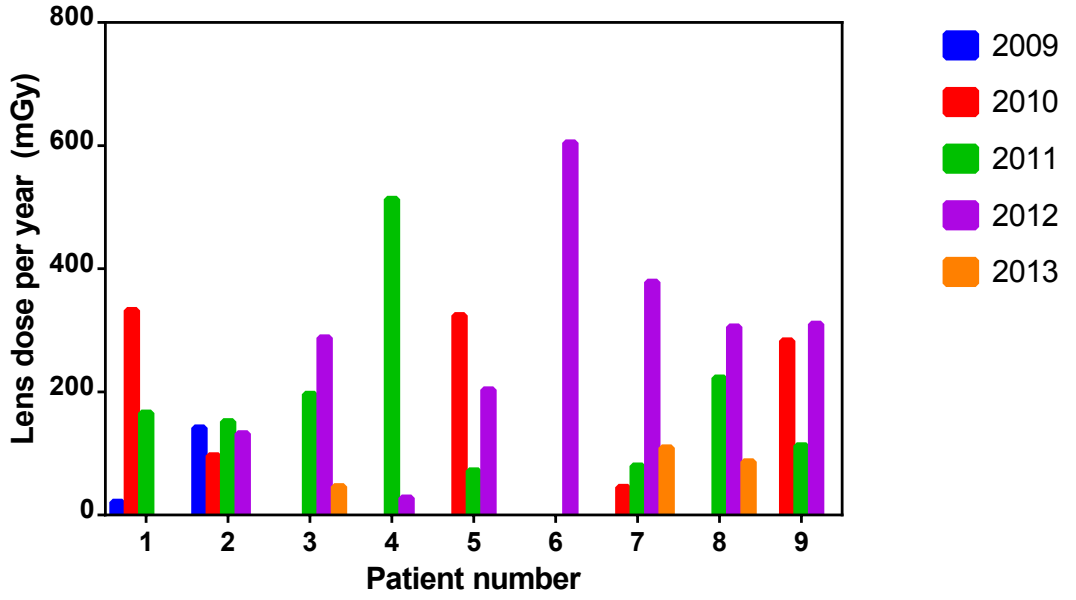

a)

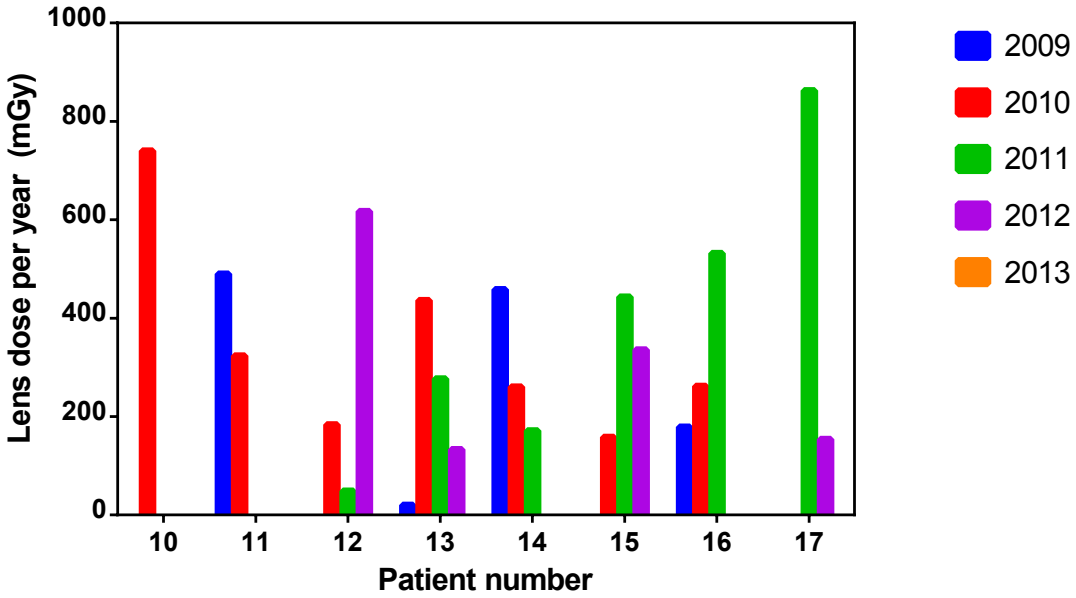

b)

Figure 5.9: Lens dose per year in the 17 patients that had cumulative lens doses exceeding the ICRP threshold dose of 500 mGy. a) Patients number 1 through 9; b) Patients numbers 10 through 17

5.3.5 Age-based Versus Size-based Cumulative Lens Dose Estimates

Cumulative lens doses were also calculated using the age-based method; the phantom age-based $CTDI_{vol}$-to-lens dose CFs are listed in Table 2.7 for the scanner-independent (SI) method, and Table 3.2 for the protocols with OB-TCM. The newborn CF was used if the patient was between 0 and 1 years of age. Like wise, the 1-year-old, 5-year-old, and 10-year-old CFs were used if the patient was between 1 and 5 years, 5 and 10 years, and 10 and 18 years, respectively. Once the appropriate $CTDI_{vol}$-to-lens dose CF for was used to convert $CTDI_{vol}$ to lens dose for each exam based upon scanner model, cumulative lens dose was calculated by summing the doses from all exams for each patient.

A plot of the age-based cumulative lens dose versus the size-based cumulative lens dose is shown in Figure 5.10. The age-based method overestimated the lens dose compared to the size-based method, which is indicated by a slope less than 1. However, this overestimation was less than 3%, which suggests that the age-based method can provide a good estimate of lens dose without having to measure head size.

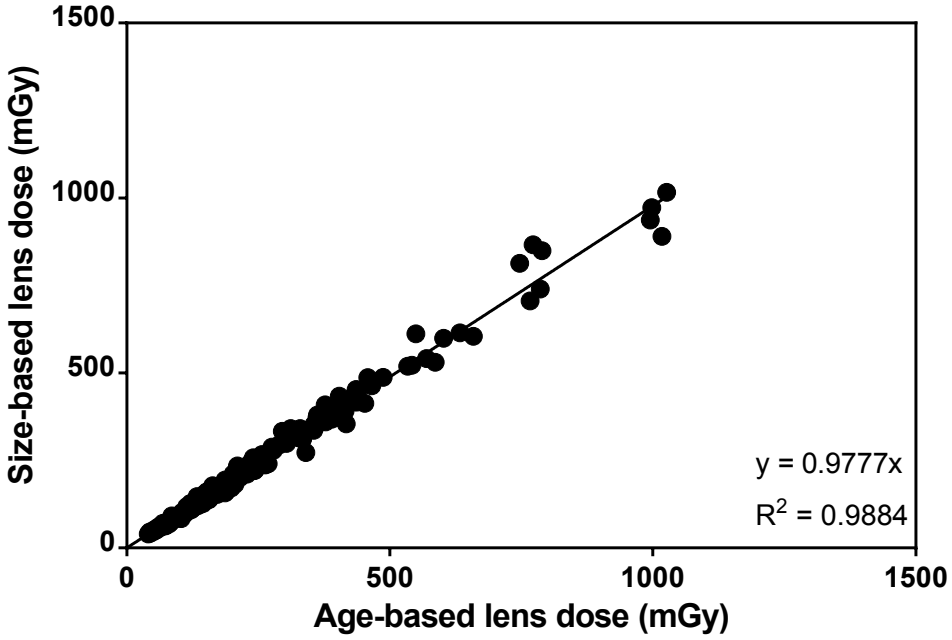

Figure 5.10: Comparison of size-based and age-based methods to calculate cumulative lens dose in children. The size-based method used the effective head diameter to calculate the $CTDI_{vol}$-to-lens dose CF. The age-based method used the patient age at the exam date to determine the appropriate phantom age-specific $CTDI_{vol}$-to-lens dose CF.

5.4 Conclusions

Several studies have investigated the cumulative radiation dose to the lens from repeated head CT scans in children and have found that this value can range from 0 to 1392 mGy (92, 132, 133). However, these studies have shortcomings in their dose estimation methodologies and none of them have accounted for differences in patient head size, which would likely cause some discrepancies in reconstructed lens doses. Thus, the objective of this chapter was to use the size-specific dose estimation methods

(described in Chapter 2 and Chapter 3) to reconstruct lens doses in pediatric patients who received CT scans of the head at Duke University Medical Center.

The results of this study have shown that lens dose can vary based upon age of the patient and also the imaging protocol (i.e. CT Brain, CT Sinus, etc.). This is primarily due to the fact that our institution uses different technical factors for a given head CT protocol based upon the age of the patient; the protocols are broken down into the age ranges of 0-3 years, 4-7 years, 8-12 years, and 13 and up. Additionally, technical factors vary between imaging protocols based upon the anatomy of interest.

The cumulative lens doses calculated in the pediatric retrospective study ranged from 40 to 1020 mGy (Figure 5.6), which is similar to the range calculated in other studies (92, 132, 133), and was observed to increase linearly as the total number of exams increased. There were 17 patients who received cumulative lens doses exceeding 500 mGy (threshold dose assumed by the ICRP in Publication 118 (56)). Out of those 17 patients, there were 7 that exceeded that value in one year.

It is important to note that the children receiving these exams are often extremely sick, and repeated imaging exams are warranted in order to help them become healthy or ensure that they remain healthy. Additionally, Duke University Medical Center is a level I trauma center and has a comprehensive cancer center, so our patient population may not be representative of every hospital in the United States. Further investigation into cumulative lens doses should be performed at different types of medical centers,

including smaller regional hospitals as well as other large academic medical centers, in order to see the complete picture on this topic. This cohort of individuals is particularly interesting from an epidemiological standpoint because they are children, and there has only been a few studies on the incidence of radiation-induced cataract in children (64, 65, 131). Additionally, the use of the exposure history from a patient's medical record allows for a more accurate estimate of lens dose as well as provides information on how frequent the patient was exposed to radiation (i.e. fractionation).

6. Reconstruction of Radiation Dose to the Lens of the Eye in Adult Patients from CT Imaging of the Head

6.1 Introduction

The presence of lenticular opacities has been previously studied in adults who have been exposed to radiation from diagnostic CT scans (74-77). The results of these studies are somewhat conflicting, with three studies suggesting that there is a relationship between history of x-ray exposure and cataract formation (74, 75, 77) and one study finding no significant relationship between the two (76). Three of the studies were limited by the fact that the radiology history of each subject was self-reported and either only a sample of the subjects had their medical records reviewed for accuracy or they were not validated at all (74-76). The fourth study was a nationwide population-based study in Taiwan (77). The participants in this study were enrolled in the Taiwan National Health Insurance Research Database, which allowed for direct access to their complete exposure histories. Their findings suggested that cataract incidence increases gradually with increasing frequency of CT examinations (77). However, none of these studies have investigated the cumulative lens dose received by their participants.

There have not been many studies on cumulative radiation dose to the lens from repeated head CT scans in adults. The one relevant study investigated the radiation dose to patients with chronic conditions; the cohort of patients in this study who received multiple head CT exams were those diagnosed with hydrocephalus. For this particular condition, they included pediatric and adults in their data set with an age range of 43.0 ±

31.9 (135). One of the limitations of this study is that they estimated lens dose using values from previously published studies. For CT imaging of the brain and orbits, they assigned mean lens dose values of 27 and 56 mSv, respectively (135). This is likely to cause high uncertainties in the dose estimates since technical factors, and therefore lens dose, will change based upon protocol, which is often age-specific (i.e. pediatric vs. adult).

While data has already been collected on cumulative lens dose in the pediatric population at our institution (Chapter 5), a study on the adult population is warranted in order to understand the complete picture of lens doses received by patients of different age groups. Thus, the objective of this chapter is to use the size-specific dose estimation methods (described in Chapter 2 and Chapter 3) to reconstruct lens doses in adult patients who received CT scans of the head at Duke University Medical Center.

6.2 Materials and Methods

A retrospective review of the radiology and electronic medical records was performed for 243 adult patients who underwent CT imaging of the head between 2009 and 2013. This retrospective review was part of an IRB-approved study (eIRB study Pro00048517); the protocol for this study is listed in Appendix C.

6.2.1 Patient Selection and Data Collection

The same methods used to collect data for the pediatric retrospective study, which are described in Section 5.2.1, were also used for data collection in the adult retrospective study.

AP and LAT diameters were measured in the supraorbital region of the head using methods described in Section 2.2.6. Since the adult head size remains relatively constant with age, this value was recorded for three exams for each patient in the Excel spreadsheet alongside the $CTDI_{vol}$.

6.2.2 Lens Dose Reconstruction

For each patient, the cumulative lens dose was calculated using equation 5.1, which is described in Section 5.2.2.

6.3 Results

6.3.1 Age-Head Size Relationship

The relationship between the effective head diameter and patient age is shown in Figure 6.1. While it is known that head size is related to height (136), this graph shows no drastic changes in head size like that observed in the 0 to 2 year-old age range in Figure 5.4 The effective head diameter measured in the adult patients in this study ranged from 14 to 20 cm.

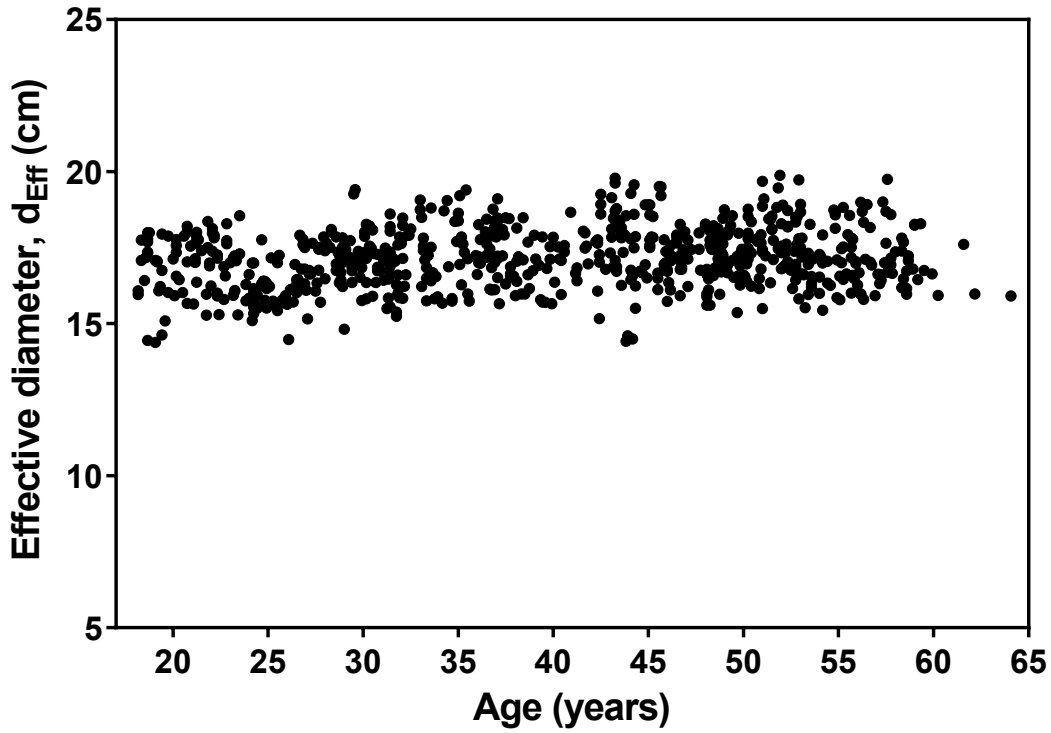

Figure 6.1: Relationship between the effective head diameter and age in the adult retrospective study

6.3.2 Exam Distribution

The distribution of the type of head CT exams for which dose data was collected in the retrospective adult patient study is displayed in Figure 6.2. Out of the 2619 head CT exams included in this study, the majority were CT imaging of the brain, followed by CT imaging of the sinuses, CT angiography of the head, and CT imaging of the orbits, and temporal bones. This distribution is almost identical to that observed in the pediatric retrospective study (Figure 5.5).

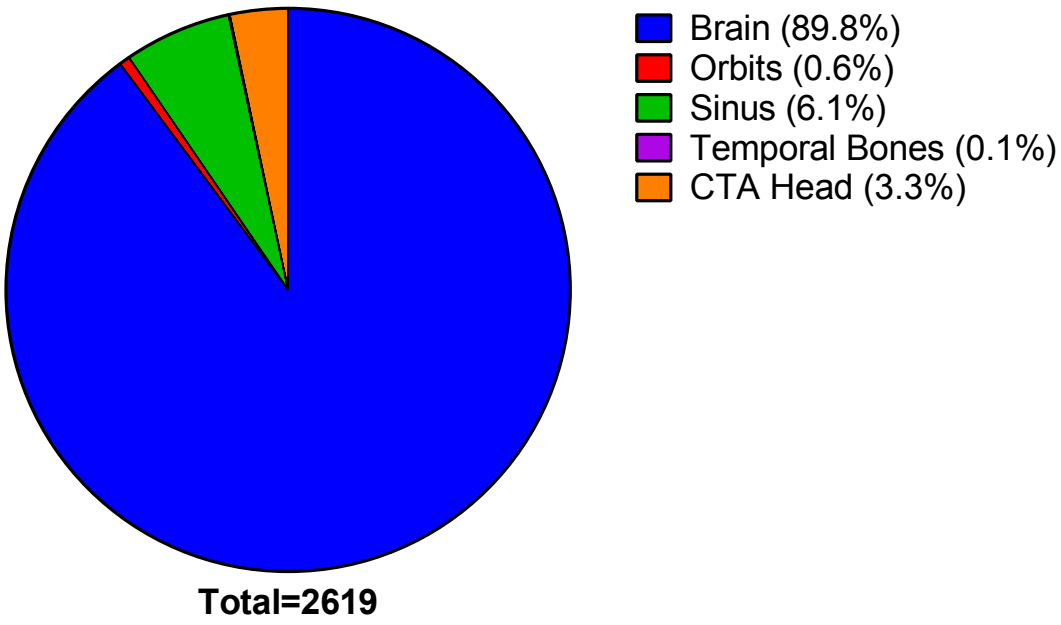

Figure 6.2: Distribution of head CT exams in the adult retrospective study

6.3.3 Lens Dose Per Head CT Exam

The distribution of lens dose per exam in the CT Brain protocol is listed in Table 6.1 for each year that data was collected for the adult retrospective study. The data included in this table are the minimum, 25th percentile, median, 75th percentile, and maximum. The mean and standard deviation, and upper and lower 95% confidence intervals (CI) of the mean of the lens dose per exam in the CT Brain protocol are also listed in Table 6.1. The results listed in this table show that the lens dose per CT Brain protocol decreased from 2009 to 2013, with the mean dose ranging from 39.3 mGy in 2009 to 31.1 mGy in 2013. Since CT imaging is a highly dynamic field, this could be due to changes in the protocols from 2009 to 2013, which would have an effect on the resulting lens dose.

Table 6.1: Lens dose statistics for the CT Brain protocol in the adult retrospective study

	Lens dose (mGy)				
	2009	2010	2011	2012	2013
Number of values	480	461	604	600	208
Minimum	27.4	4.2	5.2	6.5	23.3
25th Percentile	36.8	36.6	37.3	27.0	26.6
Median	39.0	38.7	39.5	34.6	30.8
75th Percentile	41.1	40.9	41.3	38.9	35.9
Maximum	162.3	55.5	83.9	57.5	45.1
Mean	39.3	38.4	38.9	33.3	31.1
Standard deviation	6.7	4.1	4.5	6.6	5.0
Lower 95% CI of mean	38.7	38.1	38.6	32.7	30.4
Upper 95% CI of mean	39.8	38.8	39.3	33.8	31.8

Since there were only 16 values collected for the CT Orbital protocol, they were grouped all together instead of analyzing the data by year. The minimum, 25th percentile, median, 75th percentile, maximum, mean and standard deviation, and upper and lower 95% CI of the mean are listed in Table 6.2 for the CT Orbital protocol. The mean lens dose per CT Orbital protocol was determined to be 23.1 ± 6.3 mGy.

Table 6.2: Lens dose statistics for the CT Orbital protocol in the adult retrospective study

	Lens dose (mGy)
	2009-2013
Number of values	16
Minimum	9.5
25th Percentile	20.1
Median	24.3
75th Percentile	28.3
Maximum	30.7
Mean	23.1
Standard deviation	6.3
Lower 95% CI of mean	19.7
Upper 95% CI of mean	26.4

The distribution of lens dose per exam in the CT Sinus protocol is listed in Table 6.3 for each year that data was collected for the adult retrospective study. Similar to the trend observed in the CT Brain protocol, the lens dose per CT Sinus exam decreased from 2009 to 2013. The mean lens dose was at its highest in 2009 with a value of 30.0 mGy, and it decreased to 17.9 mGy in 2012. This again could be due to changes in the technical factors used for the CT Sinus protocol across the five year period. However, the standard deviations on these values are quite large, most likely due to the small sample size for each year of this particular protocol.

Table 6.3: Lens dose statistics for the CT Sinus protocol in the adult retrospective study

	Lens dose (mGy)				
	2009	2010	2011	2012	2013
Number of values	42	43	20	48	8
Minimum	9.0	8.6	9.7	8.1	9.5
25th Percentile	22.7	20.6	22.7	9.3	17.8
Median	26.0	23.2	23.6	20.9	25.6
75th Percentile	40.3	24.3	25.3	23.8	27.0
Maximum	49.5	47.2	46.6	40.3	36.7
Mean	30.0	22.3	25.5	17.9	22.8
Standard deviation	11.0	7.1	8.2	7.5	7.9
Lower 95% CI of mean	26.6	20.1	21.7	15.7	16.2
Upper 95% CI of mean	33.5	24.4	29.4	20.1	29.5

There were only two values collected for the CT Temporal Bones protocol, both of which were from 2012. From these three values, the mean lens dose for the CT Temporal Bones protocol was determined to be 18.4 ± 0.0 mGy.

The distribution of lens dose per exam in the CTA Head protocol is listed in Table 6.4 for each year that data was collected for the adult retrospective study. Similar to the trend observed in the CT Brain and the CT Sinus protocols, the lens dose per CTA Head exam decreased from 2009 to 2013. The mean lens dose was at its highest in 2010 with a value of 38.5 mGy, and it decreased to 25.3 mGy in 2013. This again could be due

to changes in the technical factors used for the CTA Head protocol across the five year period. Again, the standard deviations of the mean are large, resulting from the small sample sizes per year.

Table 6.4: Lens dose statistics for the CTA Head protocol in the adult retrospective study

	Lens dose (mGy)				
	2009	2010	2011	2012	2013
Number of values	34	16	13	18	6
Minimum	12.6	21.4	21.8	17.8	20.7
25th Percentile	25.3	35.7	27.3	22.3	21.7
Median	37.4	36.5	38.0	24.6	25.4
75th Percentile	44.1	38.6	41.9	27.3	27.3
Maximum	54.7	88.5	54.3	54.6	32.8
Mean	35.6	38.5	36.9	26.9	25.3
Standard deviation	12.2	14.7	10.0	8.6	4.2
Lower 95% CI of mean	31.3	30.6	30.8	22.6	20.9
Upper 95% CI of mean	39.8	46.3	42.9	31.2	29.7

6.3.4 Cumulative Lens Dose

A histogram of the reconstructed cumulative lens dose is shown in Figure 6.3. In the adult patients included in this study, the cumulative lens dose ranged from 53.1 to 2891.7 mGy. Again, if this study assumes the threshold dose proposed by the ICRP of 500 mGy (56), there were 53 out of 243 patients (21.8%) that received cumulative doses exceeding the dose threshold. A larger percentage of patients in the adult study were

estimated to have received over 500 mGy compared to that of the pediatric study. This is likely because of the higher dose per examination for adults compared to children.

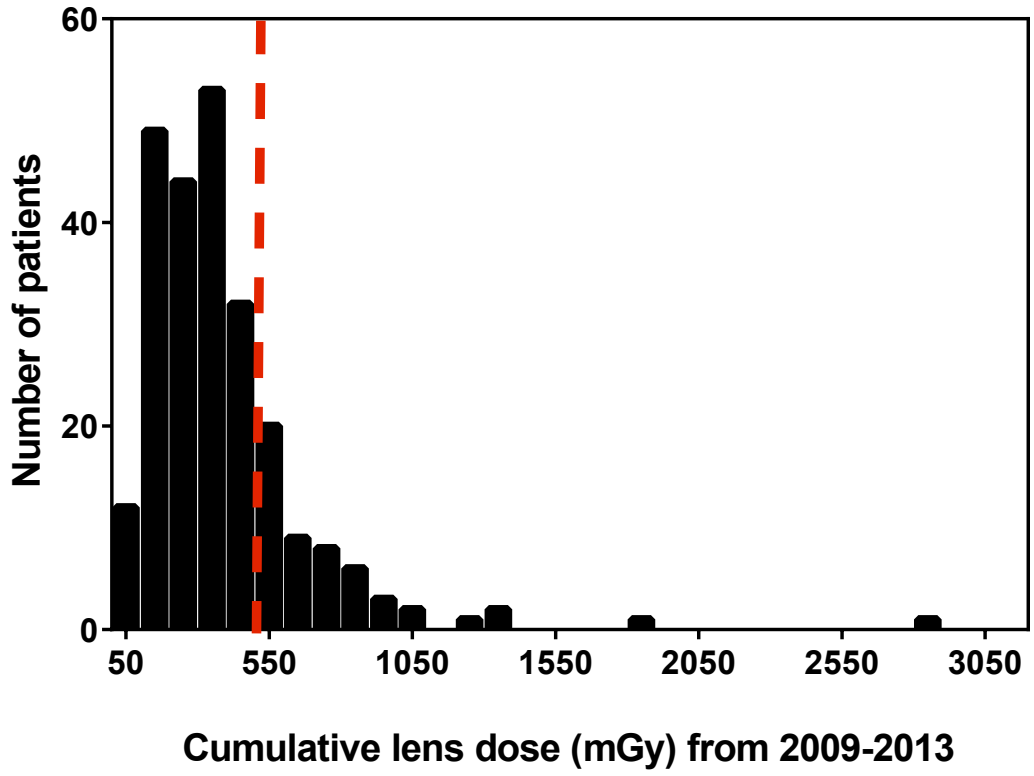

Figure 6.3: Histogram of cumulative lens doses calculated in the adult retrospective study. The red dashed line represents the ICRP threshold dose for radiation-induced cataractogenesis.

The relationship between cumulative lens dose and total number of exams is displayed in Figure 6.4. This figure shows a linear increase in the cumulative lens dose as the total number of exams increases. Unlike the same graph in the pediatric study (Figure 5.9), it has more of a narrow distribution, likely because technical factors used for a given head imaging protocol do not change based upon age for adults, whereas

they do for children. Additionally, there is not nearly as much variability in head size, and therefore not much variability in lens dose, in adults as there is in children.

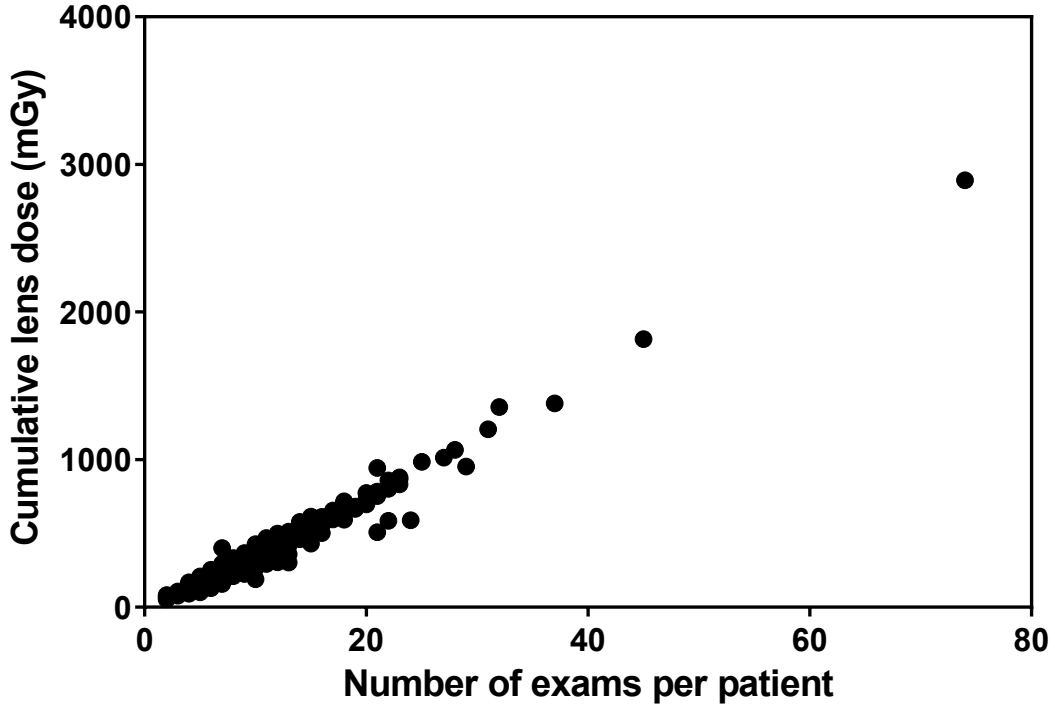

Figure 6.4: Relationship between cumulative lens dose and total number of exams per patient in the adult retrospective study

6.3.5 Lens Dose per Year in Patients Exceeding the ICRP Threshold Dose for Cataract Formation

In the 53 patients who received cumulative lens doses greater than 500 mGy, there were 21 patients out of 243 (8.6%) that exceeded that value in one year. Again, this percentage is much higher than that observed in the pediatric study (8.6% vs. 3.4%), which is likely due to the increased lens dose per exam in adults compared to children. While there have been several studies on cataract incidence in adults who have a history of exposure to radiation from diagnostic CT examinations (74, 75, 77), none of the

studies have provided lens dose estimates. In this study, the use of the exposure history from a patient's medical record allowed for lens dose to be estimated as well as provided information on exposure fractionation.

6.3.6 Age-based Versus Size-based Cumulative Lens Dose Estimates

Cumulative lens doses were also calculated using the age-based method; the phantom age-based $CTDI_{vol}$-to-lens dose CFs are listed in Table 2.5 for the scanner-independent (SI) method, and Table 3.2 for the protocols with OB-TCM. The appropriate $CTDI_{vol}$-to-lens dose CF for the adult male (listed in the above-mentioned tables) was used to convert $CTDI_{vol}$ to lens dose for each exam based upon scanner model, and cumulative lens dose was calculated by summing the doses from all exams for each patient. A plot of the age-based cumulative lens dose versus the size-based cumulative lens dose is shown in Figure 6.5. The age-based method overestimated the lens dose compared to the size-based method, which is indicated by a slope less than 1. However, the overestimation was less than 6%, which suggests that this method can provide a good estimate of lens dose without having to measure head size.

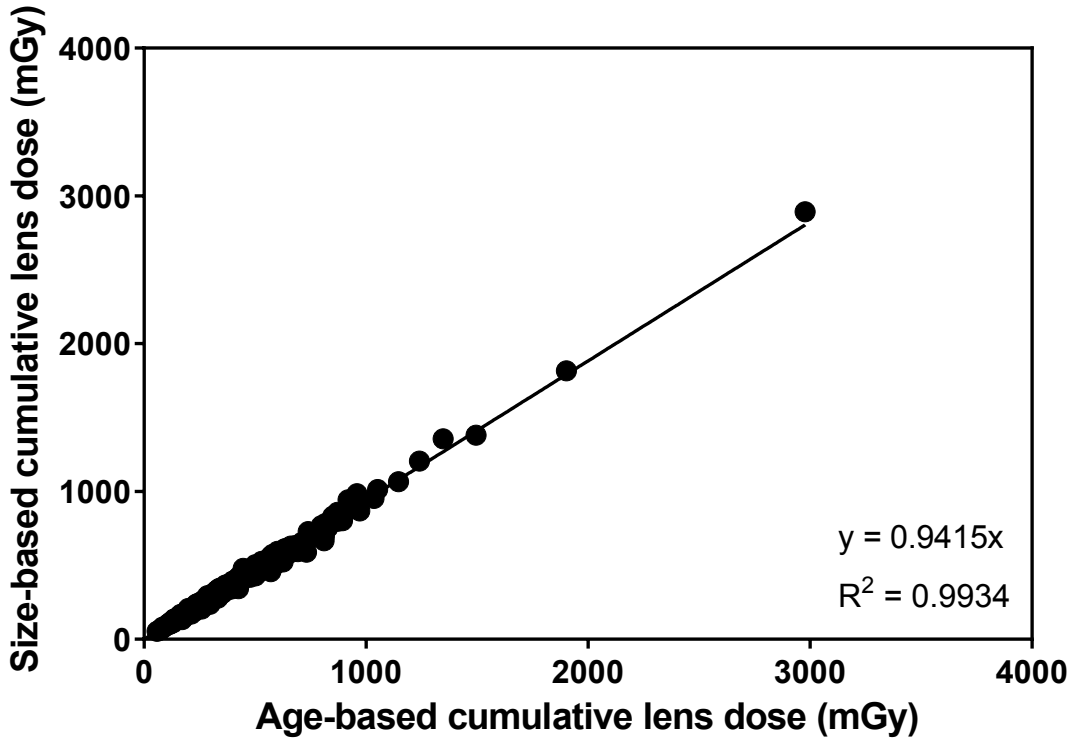

Figure 6.5: Comparison of size-based and age-based methods to calculate cumulative lens dose in adults. The size-based method used the effective head diameter to calculate the $CTDI_{vol}$-to-lens dose CF. The age-based method used the patient age at the exam date to determine the appropriate phantom age-specific $CTDI_{vol}$-to-lens dose CF.

6.4 Conclusions

There have not been many studies to investigate the cumulative radiation dose to the lens from repeated head CT scans in adults. The one relevant study has a shortcoming in their dose estimation methodology and they did not account for differences in head size (135). Thus, the objective of this chapter was to use the size-specific dose estimation methods (described in Chapter 2 and Chapter 3) to reconstruct

lens doses in adult patients who received CT scans of the head at Duke University Medical Center.

The results of this study have shown that lens dose can vary based upon the imaging protocol (i.e. CT Brain, CT Sinus, etc.). This is because technical factors vary between imaging protocols based upon the anatomy of interest. Lens doses were not analyzed by age because head protocols do not vary by age in the adult population like they do in children. However, there was a general decreasing trend in calculated lens doses per protocol from 2009 to 2013, which is likely caused by changes in protocols over time due to the highly dynamic nature of CT imaging.

The cumulative lens doses calculated in the adult retrospective study ranged from 50 to 2900 mGy (Figure 6.3), which is much larger than the range measured in the pediatric retrospective study (Chapter 5). This is likely due to the higher lens doses per protocol for adults compared to children. The cumulative lens dose was observed to increase linearly as the total number of exams increased. There were 53 patients (21.8%) who received cumulative lens doses exceeding 500 mGy (threshold dose assumed by the ICRP in Publication 118 (56)). Out of those 53 patients, there were 21 (8.6%) that exceeded that value in one year.

Like the results from the pediatric study, it is important to note that the adults receiving these exams are often extremely sick, and repeated imaging exams are warranted in order to help them become healthy or ensure that they remain healthy. As

discussed in Chapter 5, Duke University Medical Center is a large academic medical center, so our patient population may not be representative of every hospital in the United States. Further investigation into cumulative lens doses should be performed at different types of medical centers in order to see the complete picture on this topic. Unlike the pediatric population, this cohort of individuals may not be as interesting from an epidemiological standpoint because cataracts are a disease process typically associated with aging. However, a study like this is useful in understanding radiation dose from repeated imaging in the adult population.

7. Conclusions, Applications, and Future Outlook

7.1 Summary and Conclusions

Although CT imaging plays a tremendous role in the diagnosis and management of disease processes in the head, there is a risk of health detriment, including radiation-induced cataracts, due to radiation exposure from repeated imaging exams. Since the question remains of whether or not a dose threshold exists in radiation cataractogenesis, those who are chronically exposed to radiation from head CT could be an interesting population to study in this area. While there have been several studies to investigate the association between repeated CT imaging of the head and the formation of cataracts, they are all lacking a comprehensive dosimetry model for estimation of patient-specific lens doses.

This dissertation filled the above-mentioned void by systematically evaluating each part of the problem. First, the lens dose from the most current head CT protocols at our institution was measured in phantoms ranging in age from newborn to adult. The results of this part were used to develop a scanner-independent, protocol-independent, and size-specific method to estimate lens dose from $CTDI_{vol}$. Second, the effect of OB-TCM was accounted for in the $CTDI_{vol}$-to-lens dose estimation method. Third, the effect of gantry angulation on the lens dosimetry method was investigated, and $CTDI_{vol}$-to-lens dose CFs were derived based upon the distance from the primary beam scan range to the lens. Lastly, a method to retrospectively reconstruct lens doses was developed and

cumulative lens doses were determined for a select group of patients from both the pediatric and adult populations. This research represents a comprehensive approach to lens dosimetry in CT imaging of the head, and serves as a model for future research in the areas of CT dosimetry and radiation health effects.

7.2 Dose Reduction Methods Not Explored in this Research

While this dissertation has provided a means to account for the most relevant lens dose reduction methods in this dosimetry model, there are other ways, including the use of Bismuth shielding and the selection of the starting tube angle, that have not been investigated. The use of bismuth shielding in head CT has been well documented in the literature, with the potential for lens dose reduction ranging from 7.6 to 48.5% (94, 113, 115, 137, 138). However, because bismuth shields have several downsides like negatively affecting image quality, the American Association of Physicists in Medicine (AAPM) recommended in 2012 that, if possible, alternative dose reduction methods should be implemented instead of bismuth shielding (139). Selecting the start angle of the x-ray tube is another dose reduction method not considered in this research project. A recent Monte Carlo study determined that selecting the appropriate start angle of the tube can reduce the lens dose by 3 to 54% depending on the head size, collimation, and pitch of the helical scan (140). However, the ability to select the starting tube angle is not something that can be selected by the technologist when performing a CT exam currently, which is why this method was not further investigated in this dissertation.

7.3 Discussion on Extracting $CTDI_{vol}$ from Structured Dose Reports in Patient Studies

For future dosimetry studies, it should be noted that care should be taken when extracting $CTDI_{vol}$ from the structured dose report and using that value to reconstruct patient doses. For each imaging series listed in a structured dose report, the corresponding $CTDI_{vol}$ and, depending on the manufacturer, the z-axis locations of the scan range are given. However, an investigator cannot tell whether or not the lens is included in a given exam simply based upon the information provided in the structured dose report. Therefore, the axial or helical images for a given exam need to be reviewed in order to ensure that the lens was imaged. One should not blindly record the $CTDI_{vol}$ for each imaging series listed in a structured dose report without reviewing the images, as this would introduce greater uncertainty into the dose estimates.

7.4 Sources of Uncertainty

The lens dosimetry method described in this dissertation has provided a means to estimate lens dose from head CT exams without knowledge of protocol-specific technical factors, such as tube current and pitch. Additionally, it has also described a way to account for variations in head size. Despite this, there is a range of sources of uncertainty, with the most noteworthy ones listed below:

- Uncertainty associated with MOSFET dosimetry
    - Variations in dosimeter response are quantified by taking the average and standard deviation of multiple dose measurements.

The uncertainties associated with MOSFET dosimetry in the CT dose range have been previously estimated to be about 10% (107).

- Uncertainty associated with TLD dosimetry
    - For the experiment in which TLDs were used to measure lens dose, individual calibration factors were not determined for each TLD. Rather, a calibration curve was derived and used to convert the raw TLD readings to dose. The uncertainties associated with this include variations among individual TLD chips, which has shown to be within 5% at 120 kVp (141).
- Uncertainty associated with radiochromic film dosimetry
    - There are a number of sources of uncertainty associated with radiochromic film dosimetry, including experimental and digitization errors. In CT dose ranges, the calculated total error has been estimated to be about 3% (126).
- Calibration of dosimeters against a ADCL-calibrated ionization chamber
    - As reported by the University of Wisconsin-Madison Accredited Dosimetry Calibration Laboratory (ADCL), the uncertainty associated with calibration at diagnostic energies of the ionization chambers used in our experiments is less than 2%.
- $CTDI_{vol}$ accuracy

- This index is computed from look-up tables for each particular scanner model. Quality assurance evaluations are performed regularly in order to ensure the measured $CTDI_{vol}$ falls within 20% of the displayed value on the scanner console (142). Tests at our institution have shown that the displayed and measured $CTDI_{vol}$ values typically differ by less than 5%.

There are some sources of error that are particularly hard to quantify, like phantom positioning in the experiments. With regards to phantom positioning, the positioning lasers within the CT gantry were used make a best effort in the consistency of phantom positioning during the dosimetry experiments. However, there was some miss alignment of the phantoms in the gantry angulation study, but the measurements weren't repeated with different positioning of the phantoms so the error couldn't be quantified.

7.5 Applications and Future Outlook

This dissertation can be particularly useful in the areas of (1) radiation cataractogenesis research, (2) patient dose management, and (3) clinician education and training.

1. Research in radiation-induced cataracts from repeated CT imaging of the head has been investigated previously in adults, but these studies have lacked an effective dosimetry model and they have often relied on self-

reported exposure histories to estimate the total number of exams per person. To the best of our knowledge, there have been no studies on cataracts associated with repeated CT imaging of the head in children. This patient population is particularly interesting because they may be more sensitive to radiation compared to adults, and they are less likely to have age-related cataracts. This dissertation provides an effective dosimetry method for estimating lens dose from head CT and it also provides a framework to follow for reconstructing actual patient doses.

2. Personalized patient dose management is an important tool in CT imaging because it is such a widely used imaging modality. The method described in this dissertation could be applied to estimate and track a patient's lens dose from head CT exams.
3. Lastly, this research could have a positive impact on clinician education and training. By providing a way to estimate lens dose from the volume CT dose index, clinicians can use this technique to understand how changes in technical factors for head imaging protocols can subsequently influence radiation dose to the lens in their patients. With this knowledge, they can work on optimizing the image quality and radiation dose in head CT.

Appendix A: Lens Dose Measurements

Table A.1: Scanner-, phantom-, and protocol-specific lens doses in mGy

Phantom	Protocol	Discovery 750 HD	SOMATOM Definition Flash	OB-TCM
Newborn	Brain	5.0 ± 0.5	12.5 ± 0.8	10.8 ± 0.5
	Sinus	9.8 ± 0.3	8.0 ± 0.1	6.7 ± 0.2
	Facial Bones	16.0 ± 0.6	16.2 ± 0.2	13.4 ± 0.2
	Orbits	12.1 ± 0.3	11.0 ± 0.4	9.8 ± 0.6
	Craniofacial	6.0 ± 0.4	7.1 ± 0.7	6.4 ± 0.6
	Craniofacial HD	23.5 ± 2.0	-	-
1-year-old	Brain	4.7 ± 0.1	11.9 ± 1.2	9.0 ± 0.7
	Sinus	7.2 ± 0.3	6.3 ± 0.6	5.4 ± 0.4
	Facial Bones	13.1 ± 0.8	15.7 ± 1.9	11.1 ± 0.7
	Orbits	12.3 ± 0.7	9.9 ± 0.9	7.9 ± 1.0
	Craniofacial	5.1 ± 0.5	6.1 ± 0.3	5.4 ± 0.4
5-year-old	Brain	14.0 ± 0.8	11.9 ± 1.2	9.2 ± 0.6
	Sinus	10.9 ± 1.0	6.3 ± 0.6	5.8 ± 0.1
	Facial Bones	13.9 ± 0.9	15.7 ± 1.9	10.8 ± 0.5
	Orbits	13.1 ± 1.6	9.9 ± 0.9	7.7 ± 0.3
	Craniofacial	4.2 ± 0.8	6.1 ± 0.3	5.5 ± 0.3
	Craniofacial HD	19.6 ± 1.5	-	-
10-year-old	Brain	16.6 ± 0.5	36.2 ± 2.7	25.3 ± 1.2
	Sinus	16.6 ± 1.2	12.5 ± 1.4	10.8 ± 0.3
	Facial Bones	29.9 ± 1.9	26.2 ± 2.5	20.1 ± 1.1
	Orbits	19.4 ± 1.4	25.1 ± 1.2	16.9 ± 1.2
	Craniofacial	31.6 ± 2.1	27.4 ± 2.0	18.9 ± 1.7
Adult female	Brain	26.9 ± 1.6	27.8 ± 2.0	20.3 ± 1.8
	Sinus	17.9 ± 1.2	11.7 ± 1.0	11.3 ± 0.7
	Facial Bones	21.6 ± 0.9	26.2 ± 2.3	17.5 ± 0.4
	Orbits	16.5 ± 1.3	22.5 ± 1.8	17.2 ± 0.6
	Craniofacial	30.5 ± 1.7	26.6 ± 0.9	17.7 ± 1.4
Adult male	Brain	26.6 ± 2.3	30.6 ± 1.9	22.3 ± 1.3
	Sinus	18.7 ± 0.5	13.8 ± 1.8	10.4 ± 0.6
	Facial Bones	23.0 ± 1.5	22.5 ± 1.4	20.7 ± 1.2
	Orbits	18.2 ± 1.3	24.9 ± 0.7	19.2 ± 1.1
	Craniofacial	31.7 ± 0.9	26.8 ± 3.0	21.0 ± 1.9

Appendix B: Lateral Scout Images from the Gantry Angulation Study

a)

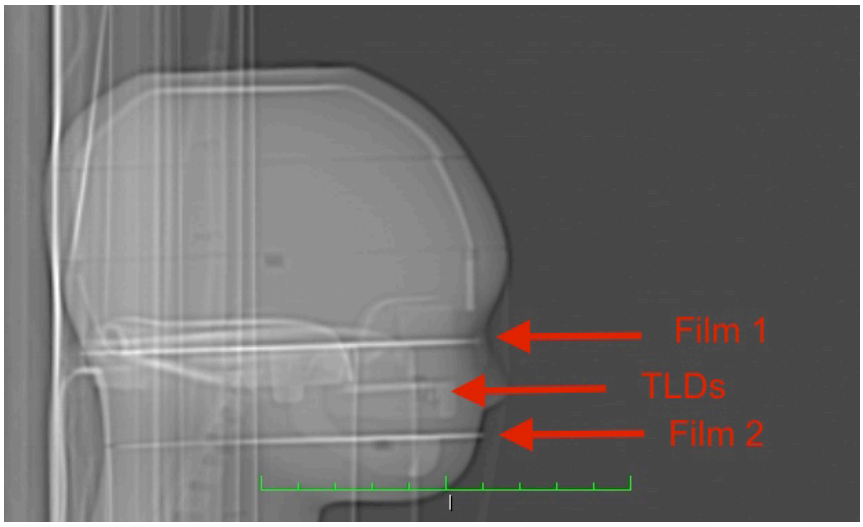

b)

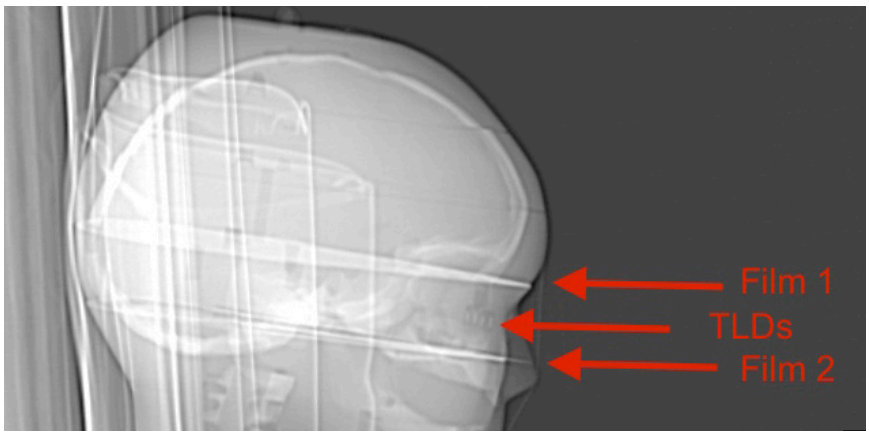

c)

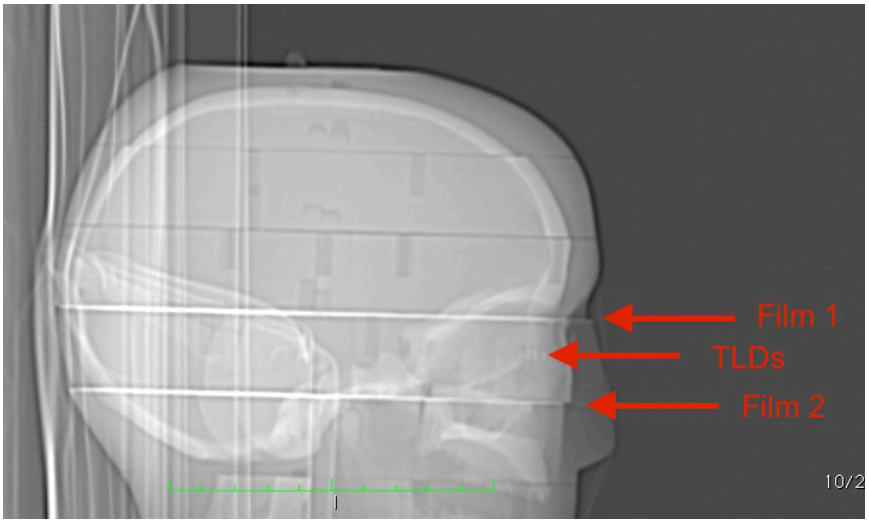

d)

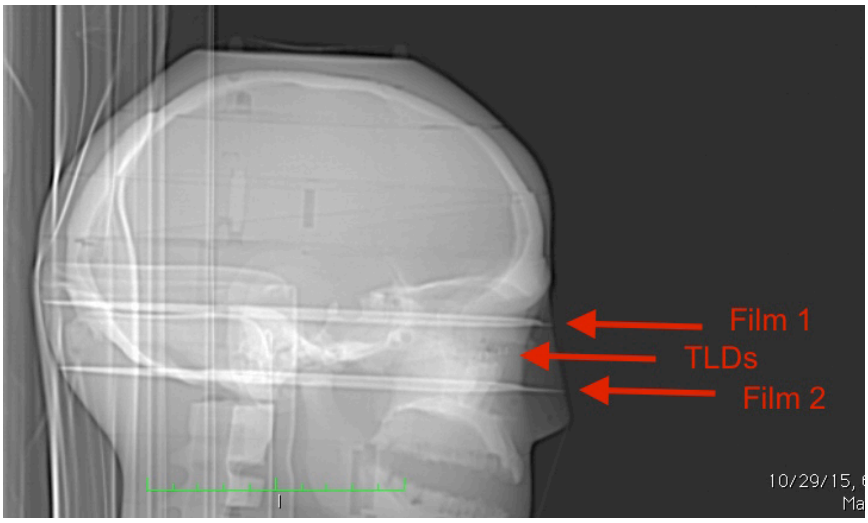

e) 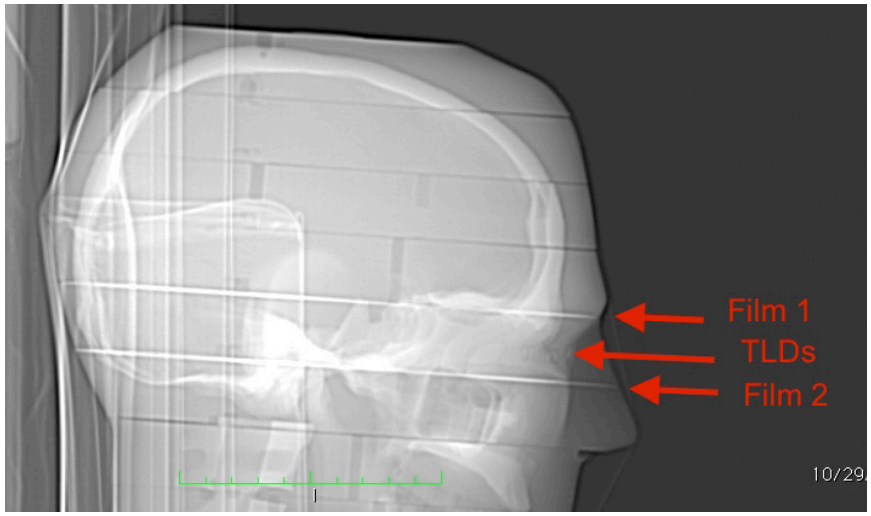

Figure B.1: Lateral scout images of the a) newborn, b) 1-year-old, c) 5-year-old, d) adult female, and e) adult male showing the placement of the two sheets of radiochromic film and the TLDs for the gantry angulation study. The lateral scout image of the 10-year-old phantom showing the dosimeter placement is displayed in Figure 4.2.

Appendix C: IRB Protocol for the Pediatric and Adult Retrospective Study

Radiation Dose to the Lens of the Eye from Head CT Scans and Radiation Induced Cataract

Background and Significance:

Ionizing radiation is generally associated with posterior sub-capsular opacities (PSC). Historically, PSC opacification was thought to be a characteristic of the radiation damage to the lens, although more recent data suggest that radiation induced opacities can be found in the lens cortex as well.

Head CT scans have become the preferred pretreatment evaluation and post-procedural follow-up imaging studies for brain, craniofacial, facial bones, and orbits due to its wide availability and fast scan times. However, head CTs involve ionizing radiation, and the long-term effect of this radiation is not known.

Anthropomorphic phantoms of varying ages (i.e. newborn, 1 year old, 5 year old, 10 year old, adult female, and adult male) scanned using both CT and MOSFET detectors were used to document total radiation dose to the lens of the eye. The purpose of performing the phantom scans was to obtain quantitative values for an average dose. To have a better understanding of the total dose exposure for pediatric and adult patients from various head CT scans, which include the orbits, sinuses, facial bones,

craniofacial, brain, and temporal bones protocols, a retrospective evaluation of the radiologic experience of these patient populations is required.

Purpose:

To document the degree of radiation exposure to the lens of the eye that pediatric and adult patients receive from head CT scans.

Design and Procedure:

This study is *a retrospective review* of the radiology and electronic health records of patients with head CT scans. The study team will review and select appropriate patient data from the Duke pediatric and adult patient population. Records will be reviewed for the period of approximately 5 years (January 2009–December 2013). All subjects that meet the criteria will be included in this retrospective review. Each subject will be assigned a serial code number (1, 2 etc.). The subject's radiology history at Duke will be reviewed and the number and type of head CT as well as the reported dose index ($CTDI_{vol}$) for each respective scan will be recorded. The subject's electronic medical record will be reviewed to verify and document age, gender, and clinical indication for radiology exam.

Risks / Benefits:

There is a small risk of a privacy breach to the subjects. The study team will only review medical information already collected as part of their routine medical care. There

are no benefits to subjects included in this study. Knowledge gained from this study may aid in better understanding cataract risks from pediatric and adult head scans.

Costs / Compensation:

There are no costs or any compensation to subjects reviewed for this retrospective study.

Data Analysis:

We will estimate the annual incidence and trend in incidence of pediatric and adult head CT scans over the study period using a Poisson log linear model, with possibility of over dispersion. We will also estimate the average number of scans per patient and test if there is a significant trend in this figure. Technical dose indices associated with CT scans such as CTDI and tube current time product (mAs) and frequency of CT scans from the pediatric and adult patient populations will be calculated. We will examine trends in the average dose per visit and the average and cumulative dose per patient. A multivariate analysis will be performed for each of the analyses to stratify effects by demographic factors such as age and gender.

Data Storage and Confidentiality:

Every effort will be made to ensure subjects' confidentiality. The data from each subject will be de-identified and assigned a serial code number (i.e. 1, 2, etc.), which will not be derived from any information about the individual and cannot be translated to

identify the individual. The key to the code will be generated in Excel. All study files containing subject information will be kept on secure password protected computers and on the radiology shared network drive with only study staff having access to the files. The key to the code will be destroyed after all data is analyzed. Study data will be kept only for the period of six years, after which all relevant study documents will be destroyed.

References

1. Thibodeau G, Patton K. Anatomy & physiology St. Louis: Mosby Elsevier; 2007.

2. Beyer T, Vogler G, Sharma D, O'Donnell F. Protective barrier effect of the posterior lens capsule in exogenous bacterial endophthalmitis--an experimental primate study. Investigative ophthalmology & visual science. 1984;25(1):108-12.

3. Cotlier E, Fox J, Bohigian G, Beaty C, Du PREE A. Pathogenic effects of rubella virus on embryos and newborn rats. Nature. 1968;217:38-40.

4. Karkinen-Jääskeläinen M, Saxén L, Vaheri A, Leinikki P. Rubella cataract in vitro: Sensitive period of the developing human lens. The Journal of experimental medicine. 1975;141(6):1238-48.

5. Friedenwald JS. Permeability of the lens capsule: with special reference to the etiology of senile cataract. Archives of Ophthalmology. 1930;3(2):182-93.

6. Augusteyn RC. Growth of the lens: in vitro observations. Clinical and experimental optometry. 2008;91(3):226-39.

7. Bassnett S, Mataic D. Chromatin degradation in differentiating fiber cells of the eye lens. The Journal of cell biology. 1997;137(1):37-49.

8. Augusteyn RC. Growth of the human eye lens. Mol Vis. 2007;13:252-7.

9. Roberts JE. Ocular phototoxicity. Journal of Photochemistry and Photobiology B: Biology. 2001;64(2):136-43.

10. Pascolini D, Mariotti SP. Global estimates of visual impairment: 2010. British Journal of Ophthalmology. 2011:bjophthalmol-2011-300539.

11. Michael R, Bron A. The ageing lens and cataract: a model of normal and pathological ageing. Philosophical Transactions of the Royal Society of London B: Biological Sciences. 2011;366(1568):1278-92.

12. Smithen LM, Brown GC, Brown MM. Dollars and sight: the economics of ophthalmology. Current opinion in ophthalmology. 2004;15(3):173-80.

13. Chan E, Mahroo OA, Spalton DJ. Complications of cataract surgery. Clinical and Experimental Optometry. 2010;93(6):379-89.

14. Klein BE, Klein R, Linton KL. Prevalence of age-related lens opacities in a population: the Beaver Dam Eye Study. Ophthalmology. 1992;99(4):546-52.

15. Flaye D, Sullivan K, Cullinan T, Silver J, Whitelocke R. Cataracts and cigarette smoking: the City Eye Study. Eye. 1989;3(4):379-84.

16. Klein BE, Klein R, Lee KE. Diabetes, cardiovascular disease, selected cardiovascular disease risk factors, and the 5-year incidence of age-related cataract and progression of lens opacities: the Beaver Dam Eye Study. American journal of ophthalmology. 1998;126(6):782-90.

17. Taylor HR, West SK, Rosenthal FS, Muñoz B, Newland HS, Abbey H, et al. Effect of ultraviolet radiation on cataract formation. New England Journal of Medicine. 1988;319(22):1429-33.

18. Chylack Jr LT, Peterson LE, Feiveson AH, Wear ML, Manuel FK, Tung WH, et al. NASA study of cataract in astronauts (NASCA). Report 1: Cross-sectional study of the relationship of exposure to space radiation and risk of lens opacity. Radiation research. 2009;172(1):10-20.

19. Black RL, Oglesby RB, von Sallmann L, Bunim JJ. Posterior subcapsular cataracts induced by corticosteroids in patients with rheumatoid arthritis. Jama. 1960;174(2):166-71.

20. Bochow TW, West SK, Azar A, Munoz B, Sommer A, Taylor HR. Ultraviolet light exposure and risk of posterior subcapsular cataracts. Archives of Ophthalmology. 1989;107(3):369-72.

21. Nakashima E, Neriishi K, Minamoto A. A reanalysis of atomic-bomb cataract data, 2000-2002: a threshold analysis. Health physics. 2006;90(2):154-60.

22. Worgul B, Kundiyev Y, Sergiyenko N, Chumak V, Vitte P, Medvedovsky C, et al. Cataracts among Chernobyl clean-up workers: implications regarding permissible eye exposures. Radiation research. 2007;167(2):233-43.

23. Goldstein LE, Muffat JA, Cherny RA, Moir RD, Ericsson MH, Huang X, et al. Cytosolic β-amyloid deposition and supranuclear cataracts in lenses from people with Alzheimer's disease. The Lancet. 2003;361(9365):1258-65.

24. Moncaster JA, Pineda R, Moir RD, Lu S, Burton MA, Ghosh JG, et al. Alzheimer's disease amyloid-β links lens and brain pathology in down syndrome. PloS one. 2010;5(5):e10659.

25. Hockwin O. Cataract classification. Documenta ophthalmologica. 1995;88(3-4):263-75.

26. Chylack LT, Leske MC, Sperduto R, Khu P, McCarthy D. Lens opacities classification system. Archives of Ophthalmology. 1988;106(3):330-4.

27. Chylack LT, Leske MC, McCarthy D, Khu P, Kashiwagi T, Sperduto R. Lens opacities classification system II (LOCS II). Archives of Ophthalmology. 1989;107(7):991-7.

28. Chylack LT, Wolfe JK, Singer DM, Leske MC, Bullimore MA, Bailey IL, et al. The lens opacities classification system III. Archives of ophthalmology. 1993;111(6):831-6.

29. Taylor HR, West SK. The clinical grading of lens opacities. Australian and New Zealand journal of ophthalmology. 1989;17(1):81-6.

30. Klein BEK, Klein R, Linton KLP, Magli YL, Neider MW. Assessment of cataracts from photographs in the Beaver Dam Eye Study. Ophthalmology. 1990;97(11):1428-33.

31. Sparrow J, Bron A, Brown N, Ayliffe W, Hill A. The Oxford clinical cataract classification and grading system. International ophthalmology. 1986;9(4):207-25.

32. Vivino M, Chintalagiri S, Trus B, Datiles M. Development of a Scheimpflug slit lamp camera system for quantitative densitometric analysis. Eye. 1993;7(6):791-8.

33. Group A-REDSR. The Age-Related Eye Disease Study (AREDS) system for classifying cataracts from photographs: AREDS report no. 4. American journal of ophthalmology. 2001;131(2):167-75.

34. Sasaki K, Shibata T, Obazawa H, Fujiwara T, Kogure F, Obara Y, et al. Classification system for cataracts. Ophthalmic research. 1990;22(Suppl. 1):46-50.

35. Thylefors B, Chylack Jr L, Konyama K, Sasaki K, Sperduto R, Taylor H, et al. A simplified cataract grading system The WHO Cataract Grading Group. Ophthalmic epidemiology. 2002;9(2):83-95.

36. Tetz MR, Auffarth GU, Sperker M, Blum M, Völcker HE. Photographic image analysis system of posterior capsule opacification. Journal of Cataract & Refractive Surgery. 1997;23(10):1515-20.

37. Bender L, Spalton DJ, Uyanonvara B, Boyce J, Heatley C, Jose R, et al. POCOman: new system for quantifying posterior capsule opacification. Journal of Cataract & Refractive Surgery. 2004;30(10):2058-63.

38. Wong WL, Li X, Li J, Cheng C-Y, Lamoureux EL, Wang JJ, et al. Cataract Conversion Assessment using Lens Opacity Classification System III and Wisconsin Cataract Grading SystemConversion Algorithm for the LOCS III and Wisconsin System. Investigative ophthalmology & visual science. 2013;54(1):280-7.

39. Durkin SR, Roos D, Higgs B, Casson RJ, Selva D. Ophthalmic and adnexal complications of radiotherapy. Acta ophthalmologica Scandinavica. 2007;85(3):240-50.

40. Jeganathan VSE, Wirth A, MacManus MP. Ocular Risks From Orbital and Periorbital Radiation Therapy: A Critical Review. International Journal of Radiation Oncology*Biology*Physics. 2011;79(3):650-9.

41. Finger PT. Radiation therapy for orbital tumors: concepts, current use, and ophthalmic radiation side effects. Survey of ophthalmology. 2009;54(5):545-68.

42. Jiang G, Tucker S, Guttenberger R, Peters L, Morrison W, Garden A, et al. Radiation-induced injury to the visual pathway. Radiotherapy and Oncology. 1994;30(1):17-25.

43. Barabino S, Raghavan A, Loeffler J, Dana R. Radiotherapy-induced ocular surface disease. Cornea. 2005;24(8):909-14.

44. Dhir S, Joshi A, Banerjee A. Radiation Retinopathy in Diabetes Mellitus Report of a Case. Acta Radiologica: Oncology. 1982;21(2):111-3.

45. Parsons JT, Bova FJ, Fitzgerald CR, Mendenhall WM, Million RR. Radiation retinopathy after external-beam irradiation: analysis of time-dose factors. International Journal of Radiation Oncology* Biology* Physics. 1994;30(4):765-73.

46. Nakissa N, Rubin P, Strohl R, Keys H. Ocular and orbital complications following radiation therapy of paranasal sinus malignancies and review of literature. Cancer. 1983;51(6):980-6.

47. Parsons JT, Bova FJ, Fitzgerald CR, Mendenhall WM, Million RR. Radiation optic neuropathy after megavoltage external-beam irradiation: analysis of time-dose factors. International Journal of Radiation Oncology* Biology* Physics. 1994;30(4):755-63.

48. Hanna C, O'Brien JE. Lens epithelial cell proliferation and migration in radiation cataracts. Radiation research. 1963;19(1):1-11.

49. Worgul B, Merriam Jr G, Medvedovsky C. Cortical cataract development--an expression of primary damage to the lens epithelium. Lens and eye toxicity research. 1989;6(4):559-71.

50. Worgul BV, David J, Odrich S, Merriam GR, Medvedovsky C, Merriam JC, et al. Evidence of genotoxic damage in human cataractous lenses. Mutagenesis. 1991;6(6):495-9.

51. Holsclaw D, Rothstein H, Medvedovsky C, Worgul B. Modulating radiation cataractogenesis by hormonally manipulating lenticular growth kinetics. Experimental eye research. 1994;59(3):291-6.

52. Merriam Jr GR, Worgul BV. Experimental radiation cataract--its clinical relevance. Bulletin of the New York Academy of Medicine. 1983;59(4):372.

53. ICRP. The 2007 Recommendations of the International Commission on Radiological Protection. Annals of the ICRP. 2007;37(2-4).

54. Di Paola M, Bianchi M, Baarli J. Lens opacification in mice exposed to 14-MeV neutrons. Radiation research. 1978;73(2):340-50.

55. Merriam Jr GR, Focht EF. A clinical and experimental study of the effect of single and divided doses of radiation on cataract production. Transactions of the American Ophthalmological Society. 1962;60:35.

56. ICRP. ICRP Statement on Tissue Reactions - Early and Late Effects of Radiation in Normal Tissues and Organs - Threshold Doses for Tissue Reactions in a Radiation Protection Context. Annals of the ICRP. 2012;41(1-2).

57. Abdelkawi S. Lens crystallin response to whole body irradiation with single and fractionated doses of gamma radiation. International journal of radiation biology. 2012;88(8):600-6.

58. Dynlacht JR. The role of age, sex and steroid sex hormones in radiation cataractogenesis. Radiation research. 2013;180(6):559-66.

59. Deeg HJ, Flournoy N, Sullivan KM, Sheehan K, Buckner CD, Sanders JE, et al. Cataracts after total body irradiation and marrow transplantation: a sparing effect of dose fractionation. International Journal of Radiation Oncology* Biology* Physics. 1984;10(7):957-64.

60. Belkacemi Y, Labopin M, Vernant J-P, Prentice HG, Tichelli A, Schattenberg A, et al. Cataracts after total body irradiation and bone marrow transplantation in patients with acute leukemia in complete remission: a study of the European Group for Blood and Marrow Transplantation. International Journal of Radiation Oncology* Biology* Physics. 1998;41(3):659-68.

61. Hall MD, Schultheiss TE, Smith DD, Nguyen KH, Wong JY. Dose Response for Radiation Cataractogenesis: A Meta-Regression of Hematopoietic Stem Cell

Transplantation Regimens. International Journal of Radiation Oncology* Biology* Physics. 2015;91(1):22-9.

62. Choshi K, Takaku I, Mishima H, Takase T, Neriishi S, Finch SC, et al. Ophthalmologic changes related to radiation exposure and age in adult health study sample, Hiroshima and Nagasaki. Radiation research. 1983;96(3):560-79.

63. Wilde G, Sjöstrand J. A clinical study of radiation cataract formation in adult life following γ irradiation of the lens in early childhood. British journal of ophthalmology. 1997;81(4):261-6.

64. Hall P, Granath F, Lundell M, Olsson K, Holm L-E. Lenticular opacities in individuals exposed to ionizing radiation in infancy. Radiation research. 1999;152(2):190-5.

65. Day R, Gorin MB, Eller AW. Prevalence of lens changes in Ukrainian children residing around Chernobyl. Health physics. 1995;68(5):632-42.

66. Merriam Jr G, Szechter A. The relative radiosensitivity of rat lenses as a function of age. Radiation research. 1975;62(3):488-97.

67. Dynlacht JR, Valluri S, Garrett J, Nees J, Caperell-Grant A, DesRosiers C, et al. Age and hormonal status as determinants of cataractogenesis induced by ionizing radiation. II. Sparsely ionizing (low-LET) radiation. Radiation research. 2012;178(4):260-5.

68. Abelson P, Kruger P. Cyclotron-induced radiation cataracts. American Association for the Advancement of Science Science. 1949:655-7.

69. Minamoto A, Taniguchi H, Yoshitani N, Mukai S, Yokoyama T, Kumagami T, et al. Cataract in atomic bomb survivors. International journal of radiation biology. 2004;80(5):339-45.

70. Chodick G, Bekiroglu N, Hauptmann M, Alexander BH, Freedman DM, Doody MM, et al. Risk of cataract after exposure to low doses of ionizing radiation: a 20-year prospective cohort study among US radiologic technologists. American journal of epidemiology. 2008;168(6):620-31.

71. Vano E, Kleiman NJ, Duran A, Rehani MM, Echeverri D, Cabrera M. Radiation cataract risk in interventional cardiology personnel. Radiation research. 2010;174(4):490-5.

72. Jacob S, Boveda S, Bar O, Brézin A, Maccia C, Laurier D, et al. Interventional cardiologists and risk of radiation-induced cataract: results of a French multicenter observational study. International journal of cardiology. 2013;167(5):1843-7.

73. Mrena S, Kivelä T, Kurttio P, Auvinen A. Lens opacities among physicians occupationally exposed to ionizing radiation-a pilot study in Finland. Scandinavian journal of work, environment & health. 2011:237-43.

74. Klein B, Klein R, Linton K, Franke T. Diagnostic x-ray exposure and lens opacities: the Beaver Dam Eye Study. American journal of public health. 1993;83(4):588-90.

75. Klein BE, Klein R, Moss SE. Exposure to diagnostic x-rays and incident age-related eye disease. Neuro-Ophthalmology. 2000;7(1):61-5.

76. Hourihan F, Mitchell P, Cumming RG. Possible associations between computed tomography scan and cataract: the Blue Mountains Eye Study. American journal of public health. 1999;89(12):1864-6.

77. Yuan MK, Tsai DC, Chang SC, Yuan MC, Chang SJ, Chen HW, et al. The risk of cataract associated with repeated head and neck CT studies: a nationwide population-based study. American Journal of Roentgenology. 2013;201(3):626-30.

78. ICRP. Non-stochastic Effects of Irradiation, ICRP Publication 41. Annals of the ICRP. 1984;14(3).

79. ICRP. 1990 Recommendations of the International Commission on Radiological Protection, ICRP Publication 60. Annals of the ICRP. 1991;21(1-3).

80. ICRP. Radiopathology of Skin and Eye and Radiation Risk, ICRP Publication 85. Annals of the ICRP. 2000;30(2).

81. ICRP. Statement on Tissue Reactions2011 10/23/2014:[1-2 pp.].

82. NCRP. Recommendations on Limits for Exposure to Ionizing Radiation, NCRP Report No. 91. Bethesda, Maryland: National Council on Radiation Protection and Measurements, 1987.

83. NCRP. Risk Estimates for Radiation Protection, NCRP Report No. 115. Bethesda, Maryland: National Council on Radiation Protection and Measurements, 1993.

84. NCRP. Limitation of Exposure to Ionizing Radiation, NCRP Report No. 116. Bethesda, Maryland: National Council on Radiation Protection and Measurements, 1993.

85. NCRP. Radiation Protection Guidance for Activities in Low-Earth Orbit, NCRP Report No. 132. Bethesda, Maryland: National Council on Radiation Protection and Measurements, 2000.

86. NCRP. Information Needed to Make Radiation Protection Recommendations for Space Missions Beyond Low-Earth Orbit, NCRP Report No. 153. Bethesda, Maryland: National Council on Radiation Protection and Measurements, 2006.

87. NCRP. Potential Impact of Individual Genetic Susceptibility and Previous Radiation Exposure on Radiation Risk for Astronauts, NCRP Report No. 167. Bethesda, Maryland: National Council on Radiation Protection and Measurements, 2010.

88. NCRP. Radiation Dose Management for Fluoroscopically-guided Interventional Medical Procedures, NCRP Report No. 168. Bethesda, Maryland: National Council on Radiation Protection and Measurements, 2011.

89. EPRI. Epidemiology and Mechanistic Effects of Radiation on the Lens of the Eye: Review and Scientific Appraisal of the Literature. Palo Alto, CA: EPRI, 2014 Contract No.: 3002003162.

90. Frush D, Chatfield M, Wildman-Tobriner B. American College of Radiology (ACR) CT Dose Index Registry: A Resource for Pediatric CT Diagnostic Reference Levels. European Workshop on DRLs in Paediatric Imaging; October 15-17; Lisbon, Portugal 2015.

91. Yamauchi-Kawaura C, Fujii K, Aoyama T, Koyama S, Yamauchi M. Radiation dose evaluation in head and neck MDCT examinations with a 6-year-old child anthropomorphic phantom. Pediatric radiology. 2010;40(7):1206-14.

92. Michel M, Jacob S, Roger G, Pelosse B, Laurier D, Le Pointe HD, et al. Eye lens radiation exposure and repeated head CT scans: A problem to keep in mind. European journal of radiology. 2012;81(8):1896-900.

93. Kanal KM, Vavilala MS, Raelson C, Mohan A, Cohen W, Jarvik J, et al. Variation in pediatric head CT imaging protocols in Washington state. Journal of the American College of Radiology. 2011;8(4):242-50.

94. Mukundan S, Jr., Wang PI, Frush DP, Yoshizumi T, Marcus J, Kloeblen E, et al. MOSFET dosimetry for radiation dose assessment of bismuth shielding of the eye in children. AJR American journal of roentgenology. 2007;188(6):1648-50.

95. Suzuki S, Furui S, Ishitake T, Abe T, Machida H, Takei R, et al. Lens exposure during brain scans using multidetector row CT scanners: methods for estimation of lens dose. American Journal of Neuroradiology. 2010;31(5):822-6.

96. Jaffe TA, Hoang JK, Yoshizumi TT, Toncheva G, Lowry C, Ravin C. Radiation dose for routine clinical adult brain CT: variability on different scanners at one institution. American Journal of Roentgenology. 2010;195(2):433-8.

97. Abdeen N, Chakraborty S, Nguyen T, dos Santos M, Donaldson M, Heddon G, et al. Comparison of image quality and lens dose in helical and sequentially acquired head CT. Clinical radiology. 2010;65(11):868-73.

98. Bassim MK, Ebert CS, Sit RC, Senior BA. Radiation dose to the eyes and parotids during CT of the sinuses. Otolaryngology-Head and Neck Surgery. 2005;133(4):531-3.

99. Shope TB, Gagne RM, Johnson GC. A method for describing the doses delivered by transmission x-ray computed tomography. Medical physics. 1981;8(4):488-95.

100. AAPM. AAPM report No. 96. The measurement, reporting, and management of radiation dose in CT. 2008.

101. McCollough CH, Leng S, Yu L, Cody DD, Boone JM, McNitt-Gray MF. CT dose index and patient dose: they are not the same thing. Radiology. 2011;259(2):311-6.

102. Turner AC, Zankl M, DeMarco JJ, Cagnon CH, Zhang D, Angel E, et al. The feasibility of a scanner-independent technique to estimate organ dose from MDCT scans: using CTDIvol to account for differences between scanners. Medical physics. 2010;37(4):1816-25.

103. Turner AC, Zhang D, Khatonabadi M, Zankl M, DeMarco JJ, Cagnon CH, et al. The feasibility of patient size-corrected, scanner-independent organ dose estimates for abdominal CT exams. Medical physics. 2011;38(2):820-9.

104. AAPM. AAPM report No. 204. Size-Specific Dose Estimates (SSDE) in Pediatric and Adult Body CT Examinations. 2011.

105. McMillan K, Bostani M, Cagnon C, Zankl M, Sepahdari AR, McNitt-Gray M. Size-specific, scanner-independent organ dose estimates in contiguous axial and helical head CT examinations. Medical physics. 2014;41(12):121909.

106. CIRS. ATOM Dosimetry Phantoms. Norfolk, Virginia: Computerized Imaging Reference Systems, Inc.; 2006.

107. Yoshizumi TT, Goodman PC, Frush DP, Nguyen G, Toncheva G, Sarder M, et al. Validation of metal oxide semiconductor field effect transistor technology for organ dose assessment during CT: comparison with thermoluminescent dosimetry. American Journal of Roentgenology. 2007;188(5):1332-6.

108. Poludniowski GG, Evans PM. Calculation of x-ray spectra emerging from an x-ray tube. Part I. Electron penetration characteristics in x-ray targets. Medical physics. 2007;34(6):2164-74.

109. Poludniowski GG. Calculation of x-ray spectra emerging from an x-ray tube. Part II. X-ray production and filtration in x-ray targets. Medical physics. 2007;34(6):2175-86.

110. Poludniowski G, Landry G, DeBlois F, Evans P, Verhaegen F. SpekCalc: a program to calculate photon spectra from tungsten anode x-ray tubes. Physics in medicine and biology. 2009;54(19):N433.

111. Ogden CL, Kuczmarski RJ, Flegal KM, Mei Z, Guo S, Wei R, et al. Centers for Disease Control and Prevention 2000 growth charts for the United States: improvements to the 1977 National Center for Health Statistics version. Pediatrics. 2002;109(1):45-60.

112. Duan X, Wang J, Christner JA, Leng S, Grant KL, McCollough CH. Dose reduction to anterior surfaces with organ-based tube-current modulation: evaluation of performance in a phantom study. American Journal of Roentgenology. 2011;197(3):689-95.

113. Wang J, Duan X, Christner JA, Leng S, Grant KL, McCollough CH. Bismuth shielding, organ-based tube current modulation, and global reduction of tube current for dose reduction to the eye at head CT. Radiology. 2012;262(1):191-8.

114. Marsh R, Silosky M. Characterization and implementation of OSL dosimeters for use in evaluating the efficacy of organ-based tube current modulation for CT scans of the face and orbits. Medical physics. 2015;42(4):1730-8.

115. Nikupaavo U, Kaasalainen T, Reijonen V, Ahonen S-M, Kortesniemi M. Lens Dose in Routine Head CT: Comparison of Different Optimization Methods With Anthropomorphic Phantoms. American Journal of Roentgenology. 2015;204(1):117-23.

116. Lai N, Chen T, Tyan Y, Tsai H. Off-centre effect on dose reduction to anterior surfaces with organ-based tube-current modulation. Radiation Measurements. 2013;59:155-9.

117. Yeoman L, Howarth L, Britten A, Cotterill A, Adam E. Gantry angulation in brain CT: dosage implications, effect on posterior fossa artifacts, and current international practice. Radiology. 1992;184(1):113-6.

118. Tan J, Tan K-L, Lee J, Wan C-M, Leong J-L, Chan L-L. Comparison of eye lens dose on neuroimaging protocols between 16-and 64-section multidetector CT: achieving the lowest possible dose. American Journal of Neuroradiology. 2009;30(2):373-7.

119. Tzedakis A, Perisinakis K, Raissaki M, Damilakis J. The effect of z overscanning on radiation burden of pediatric patients undergoing head CT with multidetector scanners: a Monte Carlo study. Medical physics. 2006;33(7):2472-8.

120. Product Overview: Materials and Assemblies for Thermoluminescence Dosimetry. Franklin, Massachusetts: Thermo Fisher Scientific; 2007.

121. Technical Note 7: MOSFET Dosimeter Specifications. Best Medical Canada.

122. Ashland I. Gafchromic™ XR Film. Covington, KY: Ashland, Inc.; 2013.

123. Rampado O, Garelli E, Deagostini S, Ropolo R. Dose and energy dependence of response of Gafchromic® XR-QA film for kilovoltage x-ray beams. Physics in medicine and biology. 2006;51(11):2871.

124. Brady S, Yoshizumi T, Toncheva G, Frush D. Implementation of radiochromic film dosimetry protocol for volumetric dose assessments to various organs during diagnostic CT procedures. Medical physics. 2010;37(9):4782-92.

125. Lungren MP, Yoshizumi TT, Brady SM, Toncheva G, Anderson-Evans C, Lowry C, et al. Radiation dose estimations to the thorax using organ-based dose modulation. AJR American journal of roentgenology. 2012;199(1):W65-73.

126. Brady SL. Development of Radiochromic Film for Spatially Quantitative Dosimetric Analysis of Indirect Ionizing Radiation Fields: Duke University; 2010.

127. Fontana ST, Brubaker RF. Volume and depth of the anterior chamber in the normal aging human eye. Archives of Ophthalmology. 1980;98(10):1803.

128. U.S. Nuclear Regulatory Commission (NRC). 10 CFR § 20.1003. Standards for Protection Against Radiation - Definitions. Revised as of April 6.

129. Rosen AM, Denham DB, Fernandez V, Borja D, Ho A, Manns F, et al. In vitro dimensions and curvatures of human lenses. Vision Research. 2006;46(6–7):1002-9.

130. Boone JM. Dose spread functions in computed tomography: a Monte Carlo study. Medical physics. 2009;36(10):4547-54.

131. Chen W-L, Hwang J-S, Hu T-H, Chen M-S, Chang WP. Lenticular opacities in populations exposed to chronic low-dose-rate gamma radiation from radiocontaminated buildings in Taiwan. Radiation research. 2001;156(1):71-7.

132. Holmedal LJ, Friberg EG, Børretzen I, Olerud H, Lægreid L, Rosendahl K. Radiation doses to children with shunt-treated hydrocephalus. Pediatric radiology. 2007;37(12):1209-15.

133. Bernier M-O, Rehel J-L, Brisse HJ, Wu-Zhou X, Caer-Lorho S, Jacob S, et al. Radiation exposure from CT in early childhood: a French large-scale multicentre study. The British journal of radiology. 2012;85(1009):53-60.

134. Rollins JD, Collins JS, Holden KR. United States head circumference growth reference charts: birth to 21 years. The Journal of pediatrics. 2010;156(6):907-13. e2.

135. Stein EG, Haramati LB, Bellin E, Ashton L, Mitsopoulos G, Schoenfeld A, et al. Radiation exposure from medical imaging in patients with chronic and recurrent conditions. Journal of the American College of Radiology. 2010;7(5):351-9.

136. Bushby K, Cole T, Matthews J, Goodship J. Centiles for adult head circumference. Archives of disease in childhood. 1992;67(10):1286-7.

137. Hopper KD, Neuman JD, King SH, Kunselman AR. Radioprotection to the eye during CT scanning. American Journal of Neuroradiology. 2001;22(6):1194-8.

138. Geleijns J, Salvado Artells M, Veldkamp WJ, Lopez Tortosa M, Calzado Cantera A. Quantitative assessment of selective in-plane shielding of tissues in computed tomography through evaluation of absorbed dose and image quality. European radiology. 2006;16(10):2334-40.

139. AAPM. AAPM position statement on the use of bismuth shielding for the purpose of dose reduction in CT scanning. American Association of Physicists in Medicine, 2012.

140. Zhang D, Zankl M, DeMarco JJ, Cagnon CH, Angel E, Turner AC, et al. Reducing radiation dose to selected organs by selecting the tube start angle in MDCT helical scans: A Monte Carlo based study. Medical physics. 2009;36(12):5654-64.

141. Cao Y. Physics Characterization of TLD-600 and TLD-700 and Acceptance Testing of New X-RAD 160 Biological X-Ray Irradiator: Duke University; 2013.

142. ACR. Computed Tomography Quality Control Manual: American College of Radiology; 2012.

Biography

Natalie Ann Januzis was born on July 26, 1988 in Secaucus, New Jersey. In 2006, she began her undergraduate education at Quinnipiac University in Hamden, Connecticut. During this time, she became certified in general radiography by the American Registry of Radiologic Technologists. She graduated magna cum laude in May 2010 with a Bachelor of Science degree in Diagnostic Imaging. In August of 2010, she began working towards a Master of Science degree in Medical Physics at Duke University in Durham, North Carolina. She successfully defended her thesis titled "Accuracy of Effective Dose Estimation from Single and Double Badges and an Evaluation of Organ Dose and Image Quality in Thoracic MDCT Scans Through a Comparison of Bismuth Shields and a Global Reduction in Tube Current" and graduated in May 2012.

Since she began working towards her Doctor of Philosophy degree in 2012, she has received the Nuclear Regulatory Commission (NRC) Health Physics Fellowship and a honorable mention from the Health Physics Society Accelerator Section for presenting "A Novel Correction Method for Effective Dose in the Point Dose Method: A Case Study – Parathyroid CT Scans" at the 2014 annual meeting in Baltimore, MD. She has published papers in Physics in Medicine and Biology and the Health Physics Journal, as well as served as co-author on papers published in Radiation Protection Dosimetry, the American Journal of Roentgenology, Urology, and the Journal of Endourology.